GeSi Photodetectors and Electro-absorption Modulators for Si Electronic-photonic Integrated Circuits

By

Jifeng Liu

B.S. Materials Science and Engineering
Tsinghua University, 1999

M.S. Honors Materials Physics and Chemistry
Tsinghua University, 2001

Submitted to the Department of Materials Science and Engineering in Partial Fulfillment of the Requirements for the Degree of

Doctor of Philosophy in Electronic, Photonic and Magnetic Materials
at the
Massachusetts Institute of Technology

February 2007

Signature of Author: _____
Department of Materials Science and Engineering
Nov 9th, 2006

Certified by: _____
Lionel C. Kimerling
Thomas Lord Professor of Materials Science and Engineering
Thesis Supervisor

Accepted by: _____
Samuel M. Allen
POSCO Professor of Physical Metallurgy
Chair, Departmental Committee on Graduate Students

GeSi Photodetectors and Electro-absorption Modulators for Si Electronic-photonic Integrated Circuits

By

Jifeng Liu

Submitted to the Department of Materials Science and Engineering
on November 9th, 2006 in Partial Fulfillment of the Requirements for the
Degree of Doctor of Philosophy in Electronic, Photonic and Magnetic Materials

ABSTRACT

The silicon electronic-photonic integrated circuit (EPIC) has emerged as a promising technology to break through the interconnect bottlenecks in telecommunications and on-chip interconnects. High performance photonic modulators and photodetectors compatible with Si complimentary metal oxide semiconductor (CMOS) devices are indispensable to achieve this goal. A photonic modulator generates optical "1" and "0" signals by switching the light on and off, while a photodetector converts the optical signals to electrical ones so that they can be processed by a CMOS circuit. Due to its compatibility with Si CMOS processing and adequate optoelectric properties, epitaxial GeSi material has been considered as a promising candidate to achieve this goal. This thesis investigates epitaxial GeSi photodetectors and electro-absorption (EA) modulators integrated with high index contrast Si(core)/SiO_2(cladding) waveguides to form an EPIC circuit on a Si platform with CMOS compatibility.

Tensile strain is introduced into the GeSi material to enhance its optoelectronic properties. The effect of tensile strain on the band structure of Ge is systematically studied, and the deformation potential constants of Ge are derived from the experimental results with relatively high accuracy. Methods to engineer the tensile strain in Ge are demonstrated. Tensile strain in small, selectively grown Ge mesas and stripes with at least one dimension $<<10$ μm is also investigated. The results are instructive to design selectively grown GeSi EA modulators and photodetectors integrated with Si/SiO_2 waveguides.

Free-space coupled Ge photodetectors on Si are fabricated with significantly improved performance in the L band (1561-1620nm) of telecommunications as a result of strain engineering. We have demonstrated a selectively grown Ge photodetector on a Si platform with a bandwidth of 8.5 GHz and a high responsivity over a broad wavelength range of 650-1605 nm. Full responsivity was achieved at 0 bias and full bandwidth was obtained at 1 V reverse bias, compatible with the requirement of Si ultra-large scale integrated circuits (ULSI).

The GeSi EA modulator is based on Franz-Keldysh (FK) effect, where the electric field shifts the direct band edge of the GeSi material and significantly enhances its

absorption coefficient in the weakly absorbing regime. Therefore, by modulating the electric field in the GeSi material, we can modulate the intensity of the light of a certain range of wavelength that passes through the GeSi material. A strain-enhanced FK effect in tensile strained epitaxial Ge material is demonstrated. A waveguide-integrated GeSi EA modulator with 4.8 dB insertion loss, 9.8 dB extinction ratio and a bandwidth >50 GHz has been designed with the material composition and device structure optimized for operations around 1550 nm. The same material and device structure can be also used for waveguide-integrated photodetectors with a responsivity of 1.1 A/W at 1550 nm and a bandwidth >35 GHz. A method to monolithically integrate GeSi modulators, photodetectors and Si/SiO_2 waveguides is proposed and the expected performance is evaluated.

Waveguide-integrated GeSi photodetectors and EA modulators are fabricated on a standard 180 nm CMOS production line based on the design. We demonstrate a waveguide-integrated GeSi photodetector with a responsivity of 1.0 A/W at 1518 nm and a bandwidth >4.5 GHz, as well as a GeSi EA modulator with an extinction ratio of ~0.3 dB. While the device performance of the EA modulator is far from ideal due to fabrication issues, the preliminary results demonstrate the feasibility of the electronic-photonic integration on a Si platform with GeSi modulator and detector devices. The problems in this first device processing are identified, and solutions are proposed and partially tested. The device performance could be greatly enhanced with improved processing technique.

Thesis Supervisor: Lionel C. Kimerling
Title: Thomas Lord Professor of Materials Science and Engineering

Acknowledgement

I would like to thank many people for their kind help and support during my Ph.D. program in MIT. First of all, I would like to express my deepest gratitude and respect to my thesis advisor, Prof. Kimerling. One night in the early spring of 2001, I dialed up Kim's cell phone number from Beijing, hoping to talk to him about a research assistant position in this group. I was very nervous when I started talking, but Kim was so nice and kind that I soon relaxed and began to talk about my research interest avidly. People often say that there are actually only a few important steps on the path of life, and this is surely one of them for me. Kim has helped me to realize the dream of studying in MIT. During these five years, Kim's guidance, support and encouragement have been invaluable to my progress in the field of Si photonics. I have learnt a lot from his insight and critical thinking. Thank you, Kim!

I also feel very lucky to work with the three senior members in Emat group: Prof. Kazumi Wada, Dr. Jurgen Michel, and Dr. Xiaoman Duan. A few days after I finished my written exam in June, 2002, Wada sen-see and I had a lunch together. He told me that he suspects that there is tensile strain in the Ge material grown in our UHV-CVD reactor. I said that I would be happy to do an XRD analysis to measure the strain in the Ge material. This is the beginning of our research on tensile strained Ge on Si, which brings about a lot of important results in my thesis. Wada sen-see is always encouraging my new ideas, and giving good advices in my research. After Wada sen-see left MIT to be a full professor in the University of Tokyo, I work closely with Dr. Michel and he has given me a lot of support in the research. We had many enlightening discussions together, and I also learnt from his superb experimental skills. His sharp mind is always very helpful for me to polish my new ideas and make them more practical. I always regard Prof. Wada and Dr. Michel as my co-advisors, and I am looking forward to learning more from them. Dr. Duan has given me motherly care over the years. She often invites me to all kinds of parties and traditional Chinese art show, which makes me feel more at home. After Xiaoxin and I got married, she invited us to dinner and gave us one of the most important lectures I had in MIT: how to keep a happy family life. I guess this is something I can never learn at school so it is invaluable. ☺

I sincerely thank the support of my thesis committee members, Prof. Fitzgerald and Prof. Marzari. Prof. Fitzgerald is a world leader in the research on epitaxial growth. His knowledge and expertise has been invaluable to me and all my predecessors working on SiGe materials and devices. I benefit a lot from the help of his group, too, especially Dr. Min-joo Lee, Dr. Nate Quitoriano, Mr. Michael Mori, Mr. Kenneth Lee, Mr. Carl Dohrman and Mr. Yu Bai. I have taken Prof. Marzari's course on first principle calculations, which greatly broadened my horizon in materials science. I am also looking forward to more collaboration with him and his group on studying the optoelectronic properties of new materials.

I also want to thank a lot of former and current staff members and students in Emat for their support. My predecessor, Dr. Douglas Cannon, has taught me a lot of tricks in Ge material growth and device fabrication in MTL. It is very helpful in making my high speed, tensile strained Ge photodetectors. Dr. Anat Eshed became our great saver twice when our UHV-CVD system broke due to unexpected power shutdowns in 2003 and 2004. Her expertise in vacuum systems is of great help to our research. Mr. Mark Beals

has made tons of efforts to establish our new lab for 6-inch UHV-CVD system. He is also our great project manager in EPIC program. I do not know how we can survive if it were not him who dealt so well with our collaborators in BAE systems and Lucent Technologies. Dr. Yasha Yi often discusses with me some new trends and new papers in microphotonics, and we used to go for a walk after lunch everyday to talk about some new ideas. Dr. Shoji Akiyama was the supreme master of device fabrications when he was in Emat, and we had a nice collaboration on the project of Ge saturable absorber for femtosecond laser. Dr. Dong Pan and I had many good discussions in designing the GeSi electro-absorption modulators, and the current design is a brain child of our thinking and rethinking. Dr. Victor Nyugen is my old office buddy, and he was the first one to show me around the Emat labs. Mr. David Danielson and Ms. Samerkhae (Nok) Jongthammanurak are my old buddies in UHV-CVD growth, and they helped me a lot in maintaining the UHV-CVD system. Nok also helped me with some AFM analysis. Dr. Wojtek Giziewicz offered lots of support in the bandwidth measurement of my photodetectors. His expertise in electrical engineering makes my life much easier dealing with RF signals. Dr. Ching-yin Hong is an expert in device processing and mask design, and she has given me much help in these aspects. I learnt waveguide measurements for the first time from Dr. Donghwan Ahn, and he is now my buddy in the research on waveguide-integrated Ge photodetectors. I am very happy to have written a few papers with him. Dr. Ningning Feng is an expert in electromagnetic theory, and I am looking forward to learning more from him on EM simulations. Ms. Lirong Zeng has been my old friend since I came to MIT, and I am very glad to collaborate with her on Si solar cell research. Mr. Jae Hyung Yi is my officemate and has helped me a lot with PL measurements. Mr. Rong Sun has helped me with some initial measurements on waveguide-integrated devices. Mr. Kevin Mccomber is a new student in our group has been learning quickly from me about the UHV-CVD system, and I would expect him to be my good successor. Mr. Xiaochen Sun is doing DLTS studies on the defects in Ge, and I hope he can achieve more insights into this aspect. Mr. Juejun Hu is my Tsinghua alumnus, and I always enjoy discussing with him about all sorts of weird ideas. I would also like to thank our secretaries, Ms. Mindy Baughman and Ms. Ellen Weene. They are of great help in our everyday work, and I think ematters cannot survive without their efforts.

I would also like to thank my good friend and TA, Prof. Stefano Curtarolo, for his outstanding teaching work in 3.23. He is the best TA I have ever met, and his interesting problem sets enhanced my interest in electronic and photonic materials and devices. His knowledge and humor always bring a lot of fun.

Many research specialists in the Microsystems Technology Laboratory (MTL) have helped me a lot with device processing. Dr. Li-wen Wang gave me the first introduction to the fabrication process in MTL. Mr. Robert J. Bicchieri has been supporting the maintenance of our UHV-CVD system in TRL. Mr. David Terry, Mr. Brian Mckenna, Mr. Eric Lim and Mr. Kurt Broderick have been always very helpful when I encounter problems in the fabrication process.

Last but not least, I would like to thank my family, i.e., my parents and my wife, Dr. Xiaoxin Wang (note that Chinese women no longer change their family names after getting married☺). My path on scientific research clearly starts from the guidance of my parents, who always encouraged me to take things apart and learn how they work when I

was a child, even if I broke things sometimes. My dad is a professor in mathematics, and his bookshelf became my field of exploration when I grew up. I would say he has the most influence on my career. I learnt most of my cooking skills from my mom, which helped me to thrive in US with authentic Chinese food. I am also very grateful to the endless love of my dear wife, Xiaoxin. For the past five years we have been living on two opposite sides of the earth, but our hearts have always been together. Her email every morning works better than 10 cups of coffee to cheer me up. Thanks to the modern optical communication technology, we never felt we were far apart. After all these years we are finally together again and will never separate. I want to say to her: "执子之手，与子携老。", meaning "holding your hand, I will grow old with you."

Table of Contents

List of Figures and Tables

Chapter 1 Introduction

1.1 Overview and Motivation

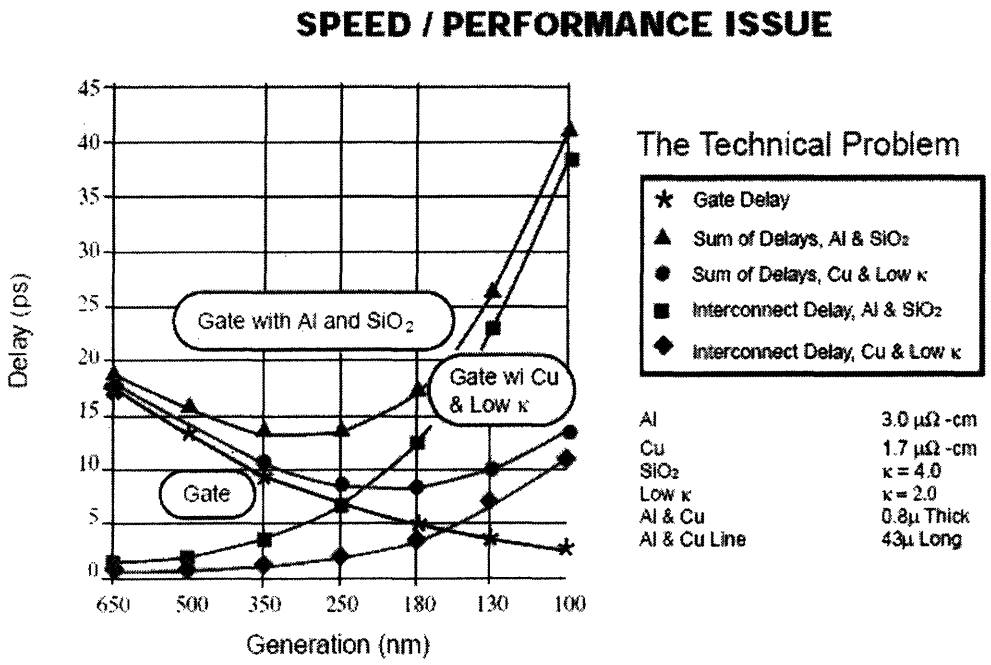

Fig. 1.1 The gate delay and interconnect delay as a function of feature size for Al/SiO_2 and Cu/low k dielectric CMOS technology

Silicon based microelectronics has achieved great success over the past 50 years and drastically changed the life of the human being. With the development of photolithography and etching technique, currently tens of millions of complementary metal oxide semiconductor (CMOS) transistors are integrated on a Si chip for information processing [1]. The driving force for improved performance in Si microelectronics is the ever shrinkage of device feature size which enables higher and higher level of integration. However, as the feature size decreases below 100 nm, the gain in the performance from shrinking the size of the devices is becoming less and less. This is due to two reasons. (1) RC delay. With the shrinkage of the feature size and the increase in the density of devices per unit area, the cross-section of the metal

interconnects decreases while the total length increases, so the resistance becomes higher and higher. Therefore, the RC delay becomes more and more severe. Fig. 1.1 shows the gate and interconnect delay vs. feature size for Al/SiO_2 and Cu/low dielectric material interconnect technology [2]. While the gate delay decreases with the feature size since the gate width becomes shorter and shorter, the RC delay due to metal interconnects increases with the shrinkage of feature size. Overall, the Al/SiO_2 technology already starts to show a significant increase in the total delay for feature size <150 nm, and Cu/low dielectric metal contacts starts to show notable increase in the total delay for sub-100 nm technology. RC delay not only slows down the overall speed of the chip, but also induces desynchronized signals in the clock distribution and increases the bit error rate of the chip. (2) The heat dissipation. The total length of metal interconnects has reached the order of 20 kilometers on the state-of-the-art Si microprocessors [3]. Winding up such a long wire on a ~1 inch square chip would generate lots of heat when the current flows through these metal interconnects. In fact, it is an important reason for Intel to abort their 4 GHz single chip central processing unit (CPU) in 2004 [4]. Clearly, metal interconnect is not ideal for ultra high speed data transmission on chip and has become a bottleneck that limits the performance of the microprocessor. New technologies are needed to speed up the data transmission on chip.

Another dilemma in modern information technology is that although the optical fiber has a capacity of 40 Gb/sec in data transmission, the speed decreases considerably when it reaches our computers and we can only obtain a bandwidth of ~100 Mb/sec by now. This is because the optical signals have to be transformed back to electrical signals and transmit through metal cables to be accepted by our computers. The RC delay in the

metal cables greatly limits the bit rate we receive from the network. We could enjoy nearly 1000 times higher bandwidth if the optical signals can be directly processed on our computers. This technology is envisioned as "Fiber to the X", where "X" stand for any terminal that receives the optical signal from an optical fiber. If we use light of slightly different wavelengths to carry different channels of information in the same optical fiber [5], then bandwidth can be even further expanded. For example, in the C band (1520-1560 nm) and L (1561-1620nm) of telecommunications, wavelengths can be divided at an interval of 0.5 nm, giving 200 channels in the C and L bands. Each channel can reach 40 Gb/sec bit rate, so the total capacity with wavelength multiplexing can reach 8 Tb/sec! The beauty of this technique is that the light of different wavelengths can be transmitted through the same optical fiber simultaneously since they do not interfere with each other. Such ability can never be achieved in metal interconnects. This technology is called dense wavelength division multiplexing (DWDM). If we can integrate photonic devices on a Si chip to filter the wavelengths and transform the optical signals from the fiber back to electronic signals for the transistors to process, then we can achieve tens of thousands of times enhancement in the bandwidth of the network.

Silicon photonics has emerged as a promising solution to the interconnect bottle neck both on chip and in the network [6]. By substituting the metallic wires with optical waveguides, not only the bandwidth of data transmission can be increased, but the heat dissipation can be greatly reduced as well since photons do not generate any heat when they propagate in a waveguide. Fig. 1.2 shows a schematic diagram of using optical clock instead of electrical clock on chip to speed up the interconnect and avoid desynchronized signals due to RC delay. In this application light source is either directly modulated or

indirectly modulate by an external photonic modulator to generate optical clocking signals.

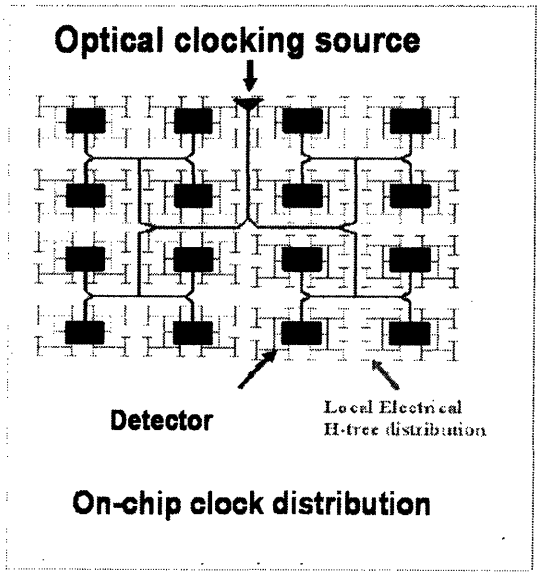

Fig. 1.2 Schematic diagram showing the concept of on-chip optical clock distribution.

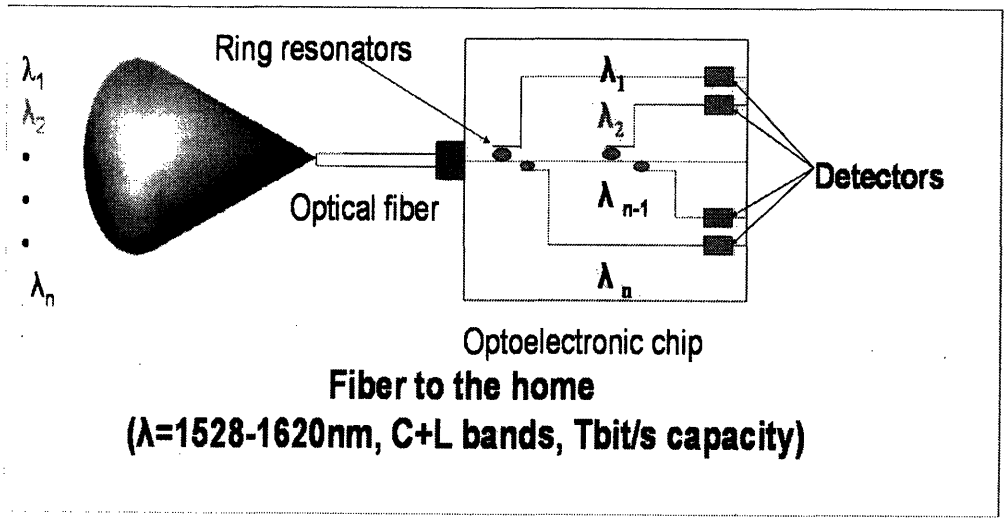

Fig. 1.3 Schematic figure showing an electronic-photonic integrated circuit (EPIC) for dense wavelength division multiplexing and fiber to the home applications.

The signals are sent through waveguides (red lines in Fig. 1.2) to different regions on chip. The waveguides keep splitting until the end node region is small enough so that the RC delay becomes negligible for the performance of the chip. At this step the optical clock signal is transformed back to electrical ones by high bandwidth photodetectors (blue squares in Fig. 1.2) and the further split electrically via H-trees (thin green lines in Fig. 1.2). By introducing optical functions onto a Si chip, the computer can also talk to the outside world optically and make full use of the high bandwidth offered by optical communications. Fig. 1.3 shows a schematic drawing to achieve DWDM on a Si chip. The optical signals carried by different wavelengths are coupled from a fiber to the waveguide, filtered by ring resonators that pick up a specific wavelength, and then transformed back to electrical signals by a photodetector. In this way, our computers can directly receive optical signals from optical fibers and fully exploit the high bandwidth provided by optical communications. Clearly, to achieve electronic-photonic integrated circuit (EPIC) on chip, four components are essential: the light source (laser or LED), the modulator, the photodetector, and the waveguides that connects all these components. The laser is the "power source" for the photonic part of the chip. The modulator is used to switch the light on and off to generate optical 0 and 1 signals, while the photodetector is used to transform the optical signals back into electrical ones so that the transistors on the Si chip can process the information. Waveguides in photonics are just like the metal wires in electronics, and they conduct the optical signals to different optoelectronic components. In the case of DWDM, filters based on resonant effects (such as ring resonators) are also needed to demultiplex the different wavelengths. To exploit the advantages of photonic interconnect the modulator and the photodetector have to work at

a bandwidth greater than 10 GHz. Although such devices are readily available based on III-V semiconductors, they are not compatible with Si microelectronic technology and are hard to integrate on a Si microelectronic chip. Therefore, high performance light sources, photonic modulators and photodetectors that can be processed together with the Si electronic circuits are higher desirable for EPIC on Si. In this thesis, we focus on the research on CMOS compatible photodetector and photonic modulators devices on Si.

Germanium has been shown to be a promising material for photodetection on Si. The direct band gap of Ge is 0.8 eV, corresponding to 1550 nm. Therefore, it has a good quantum efficiency in photon absorption for wavelengths <1550 nm (C band). The electron mobility of Ge is 3900 $cm^2 sec^{-1} V^{-1}$ and hole mobility is 1900 $cm^2 sec^{-1} V^{-1}$, both are about 4 times higher than those of Si. Due to the high carrier mobility, a fast device can be achieved at a relatively low bias. Further more, SiGe technology has already been applied to strained Si transistors [7], and even Ge MOS devices is under hot investigation recently due to the high mobility and low threshold voltage offered by Ge devices [7, 8]. Therefore, the material is fully compatible with Si electronic technology and has a tendency to expand its applications in ultra-large scale integrated circuits (ULSI). Due to the 4% lattice mismatch between Ge and Si, epitaxial growth of Ge on Si has been a big challenge. However, with the development of SiGe buffer layer growth [9] and pure Ge low temperature buffer growth [10], the problem has been overcome. In terms of device fabrication, Ge photodetectors on Si with GHz bandwidth have also been demonstrated [11,12,13]. Two of the major remaining challenges for Ge photodetectors are: (1) How to enhance the quantum efficiency of Ge photodetectors in the L band of

telecommunications, and (2) how to integrate the Ge photodetectors with waveguides on a Si chip. These two issues will be addressed in this thesis.

Si based photonic modulators has also been an active field of study for nearly 20 years [14]. Most of them employ the change in the refractive index of Si by free carrier injection. The free carriers can be injected optically with a pump laser [15], or electrically with a forward biased *p-i-n* diode [16] or a CMOS device working at carrier inversion mode [17]. With the refractive index change in a Mach-Zender structure [17] or ring resonator [16], modulator devices based on phase shift have been fabricated and Si modulators working at a bandwidth of a few GHz have been demonstrated. There are several disadvantages of these devices, though. First, the injected carriers recombine in a relatively long time (greater than ns) and limit the speed of the modulator. Although the free carriers can be swept out of the Si region by reverse biasing the diode structure, the speed is still limited by the transit time of the carriers. Second, electrical injection into a p-i-n diode inevitably involves a relatively high current, which increases the power consumption of the device. Third, in the case of phase modulation by ring resonators the quality factor (Q) of the ring has to be traded off for higher speed. This is because the higher the Q, the long the light stays in the ring, and the longer the delay of the light in the modulator. However, lower Q would also decrease the modulation depth of the devices since the intensity contrast for resonant and none resonant wavelengths is no longer so large. Therefore, there is plenty of room to improve the currently available Si modulators.

In III-V semiconductors high speed optical modulators are usually achieved by electro-absorption (EA) effect like Franz-Keldysh (FK) effect in the bulk material [18] or

Quantum Confined Stark effect (QCSE) in quantum well devices [19,20]. The electric field can shift the direct band gap and change the photon absorption of III-V materials, thereby making a transparent material opaque at a certain wavelength range when an electric field is applied. With this method we can make an EA modulator. Such devices are usually achieved with reverse biased *p-i-n* diode structures, where a strong electric field is built into the intrinsic layer when a reverse bias is applied on the devices. Since the field effect takes place in sub ps time frame [21], the speed of the device can reach the order of tens of GHz [22]. Also, because the current at reverse bias is much smaller than that at forward bias, the power consumption of the device is much lower than the phase modulators by carrier injection. However, the field effect on the absorption around the band edge of Si is very weak because the oscillation strength of the indirect gap transition is more than two orders of magnitude lower than that of the direct gap [14]. Although Si also has several direct gaps, they are all in the range of 3-4 eV and are irrelevant to the wavelengths used in optical communications. Germanium, on the other hand, has a direct gap of 0.8 eV that corresponds to 1550 nm, as mentioned previously. Therefore, it is interesting to investigate the possibility of using the electric-absorption effect in Ge or GeSi alloy to modulate the light around 1550 nm. We will discuss in detail the FK effect and the design of a waveguide integrated GeSi EA modulator in this thesis.

1.2 Outline of the Thesis

Chapter 2 discusses enhancing the absorption of Ge in the wavelength range of 1550-1620 nm (part of C band and the whole L band) by tensile strain. The effect of tensile strain on the band gap of Ge is studied in detail for the first time, and the

deformation potential constants of Ge are derived from the results with relatively high accuracy. Methods to engineer the tensile strain in Ge are discussed. The strain in selectively grown Ge mesas is also studied, providing one of the most fundamental information to design waveguide-integrated GeSi photodetectors and EA modulators based on the selective growth of Ge and GeSi.

Chapter 3 presents the fabrication and characterization of tensile strained, free space coupled Ge photodetectors on Si. We demonstrate that the band gap engineering by tensile strain transfers to a significantly enhanced responsivity in the L band. The devices show a broad detection spectrum of 650-1620 nm and the bandwidth is 8.5 GHz at 1V reverse bias. The broad detection spectrum, high bandwidth and low driving voltage make it suitable for both telecommunications and optical interconnect on chip. A signal-to-noise ratio analysis shows that the detector can achieve a bit error rate of $<10^{-12}$ with a relatively low input optical power of 60 μW when working at 10 GHz clocking frequency.

Chapter 4 discusses the design of waveguide-integrated, high performance GeSi EA modulators and photodetectors. We first report the enhanced Franz-Keldysh effect observed in tensile strained Ge and compared it to the results from the theoretical calculations. Then we focus on designing the composition of a GeSi material that has optimized electro-absorption modulation performance at 1550 nm. The band gap shift due to Si doping and strain in the selectively grown GeSi structure are both taken into account. One step forward, we present two coupling schemes from the waveguide to the GeSi EA modulator and calculated the optimized dimensions of the GeSi modulator to achieve the best overall performance. We also show that the same kind of GeSi EA modulator devices can be used as photodetectors, so the modulator-waveguide-

photodetector integration can be achieved relatively easily on a single Si chip. The expected bandwidth of the modulator/photodetector devices is also estimated. Our result shows that a waveguide integrated EA modulator with >50 GHz bandwidth and ~10 dB extinction ratio can be achieved with ~5 dB insertion loss. The waveguide integrated photodetector can achieve a responsivity >1.0 A/W and a bandwidth >35 GHz. The expected performance of these devices is fully suitable for application in Si EPIC chips.

Chapter 5 presents some preliminary results on our first attempt in fabricating waveguide-integrated photodetectors and modulators. First we present the design of the fabrication process which enables the butt-coupling between waveguides and photodetectors/modulators. An important technique in the device fabrication, trench filling selective growth of GeSi, is discussed in detail. We then present the electrode design to achieve good electric performance without perturbing the optical mode in the active region of the devices. The waveguide integrated photodetector/modulator devices are characterized by optoelectronic measurements. The detectors show a responsivity of 1.0 A/W at 1518 nm, and a bandwidth >4.5 GHz. The electro-absorption modulator, however, only achieved a modulation depth of about 7% due to the relatively low electric field applied on the GeSi layer limited by the generation/recombination current in the depletion region. Also, the dark current is high in both photodetectors and EA modulators. We will discuss the source of these problems and possible ways to avoid these issues in the future fabrication process.

Chapter 6 summarizes major results and achievements of this thesis, and presents the directions of future work.

Chapter 2: Tensile Strained Epitaxial Ge on Si

In recent years, there has been an extensive study concerning the effect of strain on the band structure of semiconductors due to the applications in electronic and optoelectronic devices. Strained III-V semiconductor quantum well structures have been applied to low threshold laser diodes [23]. Strained Si on the SiGe alloy layer has been developed for high frequency complimentary metal-oxide-semiconductor (CMOS) devices [24,25,26]. Strain distorts the lattice of the semiconductor materials, thereby changing their band structures. The most interesting energy band parameters of semiconductors that can be engineered by strain are the band gap and the carrier mobility. Band gap engineering modifies the absorption/emission properties so that photon detection/emission of the material can be adjusted to our advantage. Carrier mobility can usually be enhanced by strain, so that an electronic device with high speed and lower driving voltage can be achieved.

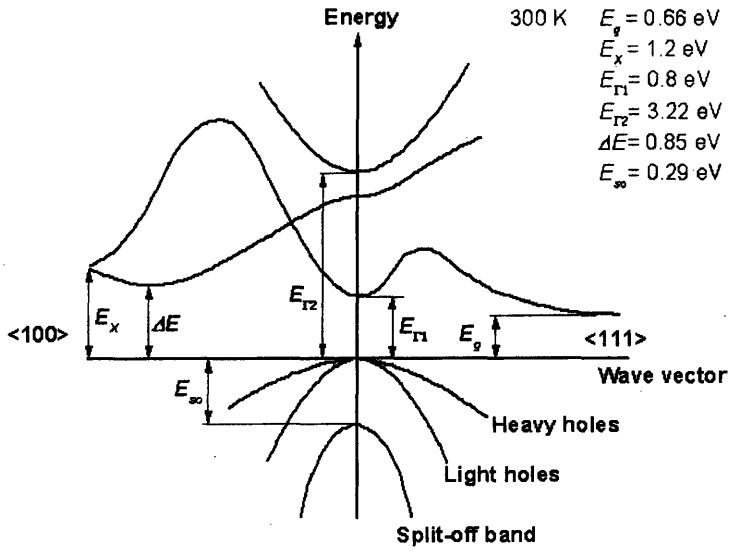

Fig. 2. 1 Energy band structure of bulk Ge

Fig. 2.1 shows the energy band structure of bulk Ge material [27]. The lowest band gap is an indirect gap of $E_g = E_g^L$ =0.664 eV at L valley (corresponding to 1867nm), and the second lowest band gap is a direct gap of $E_g^{\Gamma 1}$ =0.800 eV at Γ valley (corresponding to 1550nm). Since we are not interested in the second direct gap $E_g^{\Gamma 2}$ =3.22 eV in this thesis, in the later text the terms "direct band gap" and "E_g^{Γ}" will refer to $E_g^{\Gamma 1}$ only. The indirect band gap absorption is inefficient due to the fact that an adequate phonon is required together with a photon to complete the excitation of an electron from the valence band to the L valley. For wavelengths greater than 1550nm the absorption of Ge is due to this indirect transition only, so the absorption coefficient is low. To increase the efficiency of Ge photodetectors in the L-band (1561-1620nm) of telecommunication, it would be desirable to decrease the direct band gap of Ge by some means so that the absorption in this wavelength range would be much more efficient. In this chapter, we will discuss the effect of tensile strain on the band structure of Ge, methods of engineering tensile strain in Ge epitaxial layers, and the strain in selectively grown Ge mesas.

2.1. Effect of Strain on the Band Structure of Blanket Ge film

Blanket epitaxial thin films grown on a substrate are usually under biaxial stress state, since there is no constraint in the vertical direction (perpendicular to the film surface) so that the stress in the vertical direction should be zero. Perturbation approach based on quantum mechanics (i.e. k•p theory with strain energy Hamiltonian as a perturbation term) has been employed to derive the effect of strain on the band structure

of semiconductor materials in literature [28]. This theory is often referred to as "deformation potential theory". For diamond structure epitaxial films grown on (100) substrates, the two main axes of stress are along (010) and (001) directions. In this case, deformation potential theory shows that the effect of the strain on the fundamental band gap (at k=0) of a semiconductor material is given by [29]:

$$E_g^{\Gamma}(lh,\varepsilon_{\parallel}) = E_g{}^{\Gamma}(0) + a(\varepsilon_{\perp} + 2\varepsilon_{\parallel}) + \Delta_0/2 - 1/4\delta E_{100} - 1/2\sqrt{\Delta_0{}^2 + \Delta_0\delta E_{100} + 9/4\,(\delta E_{100})^2}$$
$$E_g^{\Gamma}(hh,\varepsilon_{\parallel}) = E_g{}^{\Gamma}(0) + a(\varepsilon_{\perp} + 2\varepsilon_{\parallel}) + 1/2\delta E_{100}\,, \tag{2.1}$$

where $\varepsilon_{\parallel}$ is the in-plane strain, $\varepsilon_{\perp}$ is the strain in the direction perpendicular to the surface of the epitaxial film; $E_g^{\Gamma}(lh,\varepsilon_{\parallel})$ and $E_g^{\Gamma}(hh,\varepsilon_{\parallel})$ are the bandgaps from the maxima of the light and heavy hole valence bands to the bottom of Γ valley (at k=0) under an in-plane strain $\varepsilon_{\parallel}$, respectively. $E_g{}^{\Gamma}(0)$ is the direct bandgap of unstrained material; a is the dilational deformation potential of the material, and b is the devitorial deformation potential constants of biaxial stress along <100> direction; $\delta E_{100} = 2b(\varepsilon_{\perp} - \varepsilon_{\parallel})$; and Δ_0 is the split-off energy. For Ge Δ_0=0.29 eV, as shown in Fig. 2.1. Under biaxial stress state, it is easy to derive from the Hooke's law in terms of tensor that $\varepsilon_{\perp}$=-$(2C_{12}/C_{11})\varepsilon_{\parallel}$ due to the fact that the stress in the vertical direction is zero. In Ge, the elastic constants are C_{11}=128.53 GPa and C_{12}=48.26 GPa [27], so $\varepsilon_{\perp}$=-0.751 $\varepsilon_{\parallel}$. As we can see from Eq. 2.1, the dilational part of the strain tensor only shift the band edges of light and heavy hole bands, while it is the devitorial part of the strain tensor that makes the light and heavy hole bands non-degenerate. This is because the dilational part of the strain tensile only changes the volume of the lattice and does not change its cubic

shape. As the cubic symmetry is maintained, the light and heavy hole bands remain degenerate. The devitorial part of the strain tensor, on the other hand, changes the lattice from cubic to tetragonal. As the cubic symmetry is broken, the light hole and heavy holes become non-degenerate at k=0. The deformation potentials a and b of Ge have been measured experimentally over the years, as summarized in Table 2.1.

Table 2.1. Deformation potential values of Ge reported in literature

	literature	Reference
a(eV)	-8.0	30
	-9.0±0.4	31
	-9.08±0.15	32
	-10.3±0.4	33
	-10.4±0.8	34
	-11.5±0.4	35
b(eV)	-1.8±0.3	36
	-1.9±0.2 (Al doped Ge)	37
	-2.2±0.2 (In doped Ge)	38
	-2.21±0.13	38
	-2.4±0.2	31
	-2.6±0.2	32
	-2.7±0.3	39
	-2.86±0.15	35

Plugging any of these reported values into Eq. 2.1, one always finds biaxial tensile strain should decrease the direct bandgap of Ge, as schematically shown in Fig. 2.2. Therefore, tensile strain could improve the absorption of Ge in the L-band (wavelength >1550 nm) and increase the quantum efficiency of Ge photodetectors. Also, the top of the valence

band is determined by the light hole band under tensile strain (Fig. 2.2). Since the light hole effective mass (0.043 m_0) is much smaller than the heavy hole (0.33 m_0) [27], the hole mobility can also be significantly increased. It has been calculated that hole mobility of Ge increases from 1900 to 10000 cm^2/V sec with 1% in-plane strain [40]. Therefore, tensile strain can improve the responsivity and the speed of Ge photodetectors at the same time.

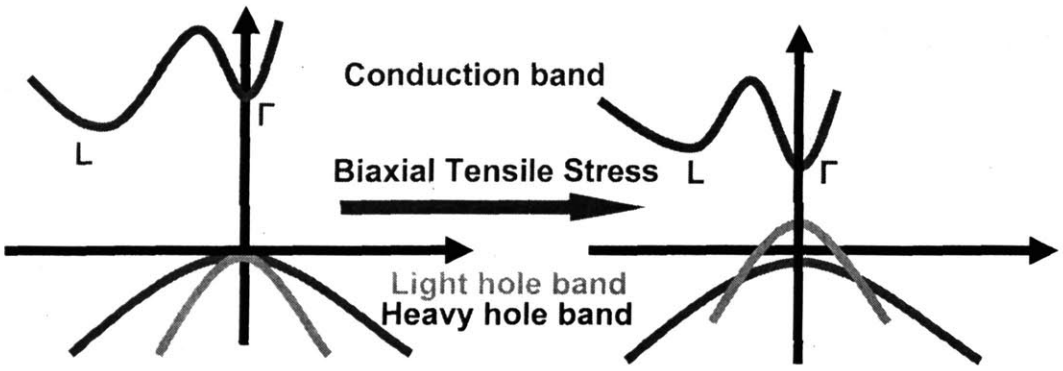

Fig. 2. 2 Schematic diagram showing the effect of tensile strain on the band structure of Ge

However, due to the brittleness of Ge bulk material all the previous experimental studies on the effect of stress/strain on the band structure of Ge have been based on uniaxial or hydrostatic compression tests [30-39], and there have been no experimental reports on the effect of biaxial tensile stress on the band structure of Ge films, i.e., the effect of tensile strain on the direct band gap of Ge has not been experimentally verified. Also, deformation potential values obtained in previous studies vary as much as 50% from different literature, as shown in Table 2.1. This large dispersion may result from the non-uniformity of the stress in the samples, especially in the uniaxial compression tests

where the samples tend to bend and deviate from the ideal uniaxial compression. To verify that tensile strain decreases the direct band gap of Ge and makes the light and heavy hole bands degenerate, and obtain accurate deformation potential constants of Ge, we study the effect of biaxial tensile stress on the direct bandgap of epitaxial Ge film on Si and derive the dilational and shear deformation potential constants, a and b, for the direct bandgap of Ge at room temperature [41,42]. These parameters are important for predicting the effect of strain on the optoelectronic properties of Ge, especially the biaxially stressed electronic and optoelectronic devices based on epitaxial Ge.

2.1.1 Mechanism of Tensile Strain Accumulation in Ge-on-Si

The lattice mismatch between Ge and Si is $f = \frac{a_{Si} - a_{Ge}}{a_{Ge}}$ =-4.0%. The misfit has to be accommodated by elastic strain ε and plastic strain δ in the Ge film, i.e.

$$f = \varepsilon + \delta \tag{2.2}$$

Very thin Ge film can grow pseudomorphically on Si with coherent interface. In that case, the misfit is completely accommodated by elastic strain ε in the Ge film. When the film grows above a certain thickness, pseudomorphic growth is no longer energetically favored since the elastic energy is too large. The film would start to relax by generating a misfit dislocation network at the interface. This way, the elastic energy decreases at the cost of increase in plastic energy of dislocations. For a given thickness, an equilibrium elastic strain ε^* is reached to minimize the total energy of the system. Fitzgerald has reviewed the study on strain relaxation in epitaxial films [43] and we will follow his review in the later text. The elastic energy per unit area of an epitaxial Ge film with a thickness of h grown on Si (100) substrate is given by:

$$E_\varepsilon = \varepsilon^2 Y_{100} h . \tag{2.3}$$

Y_{100} is the Young's modulus of Ge under biaxial stress along [010] and [001] directions, given by

$$Y_{100} = C_{11} + C_{12} - \frac{2C_{12}^2}{C_{11}}, \tag{2.4}$$

where elastic constants $C_{11} = 128.53GPa$ and $C_{12} = 48.26GPa$ so that Y_{100}=140.55 GPa for Ge [27]. The dislocation energy is given by:

$$E_d = D(f-\varepsilon)(1-\nu_{Ge}\cos^2\alpha)(b/b_{eff})\left[\ln\frac{R}{b}+1\right] \tag{2.5}$$

In the above equation, ν_{Ge} =0.27 is the Poisson ratio of Ge [27], $b = \frac{1}{2}<110>$ is the Burger's vector, b_{eff} is the effective Burger's vector (i.e., the component of b on the interface plane and perpendicular to the dislocation line), and α is the angle between the Burger's vector and the dislocation line. In diamond cubic semiconductors there are two kinds of misfit dislocations: $\alpha = 90°$ and $\alpha = 60°$. When $\alpha = 90°$, i.e., Burger's vector is perpendicular to the dislocations line on the interface plane, we have (b/b_{eff})=1. When $\alpha = 60°$, we have (b/b_{eff})=2. D is the average shear modulus of the Ge/Si interface given by

$$D = \frac{G_{Si}G_{Ge}b}{\pi(G_{Si}+G_{Ge})(1-\nu)}, \tag{2.6}$$

where G_{Si}=51 GPa and G_{Ge}=40 GPa are the shear modulus of Si and Ge on (100) interface, respectively. R is the radius of the dislocation core. When the film thickness $h > S/2$ where $S = b_{eff}/(f-\varepsilon)$ is the average spacing of two misfit dislocations, we

have $R = S/2 = b_{eff}/2(f-\varepsilon)$. When the film thickness $h < S/2$ we have $R = h$. The total energy is a sum of elastic and plastic energy. We find that the total energy is minimized at $\varepsilon = -0.0035\%$ for $\alpha = 90^\circ$ and $\varepsilon = -0.0065\%$ for $\alpha = 60^\circ$, respectively, with 1 μm Ge on Si(100). Therefore, nearly fully relaxed Ge is energetically favored for film thickness>1 μm.

The Ge epitaxial films grown by ultra-high vacuum chemical vapor deposition (UHVCVD) in this study are grown at ≥600°C. At such high temperature and with film thickness >1 μm, the Ge film is nearly completely relaxed at the growth temperature. Upon cooling to room temperature, tensile strain can be accumulated in the Ge films due to the larger thermal expansion coefficient of the Ge film compared with the Si substrate. In UHV-CVD deposition Ge films are naturally deposited on both sides of the double side polished Si (100) wafers so no curvature is introduced to the Si wafer despite of the stress in Ge films. Therefore, the thermal strain is simply given by:

$$\varepsilon_{\parallel} = \int_{T_0}^{T_1} (\alpha_{Ge}(T) - \alpha_{Si}(T))dT \,, \tag{2.7}$$

where T_0 and T_1 are room temperature and growth temperature, $\alpha_{Ge}(T)$ and $\alpha_{Si}(T)$ are the thermal expansion coefficients of Ge and Si at temperature T (°C), respectively, and are given by [44,45]:

$$\alpha_{Ge}(T) = 6.050\times10^{-6} + 3.60\times10^{-9}T - 0.35\times10^{-12}T^2 \quad (^\circ C^{-1}) \tag{2.8}$$

$$\alpha_{Si}(T) = \{3.725\times[1 - \exp(-5.88\times10^{-3}(T+149.15))] + 5.548\times10^{-4}T\}\times10^{-6} \quad (^\circ C^{-1}) \tag{2.9}$$

The theoretical strain calculated by Eq. 2.7 is plotted as a function of growth temperature in Fig. 2.3. It shows that tensile strain between 0.20-0.32% can be obtained in the growth temperature range of 600-900 °C assuming the film is fully relaxed at the growth

temperature and there is no strain relaxation during the cooling process. In reality, strain relaxation would happen at high temperature. There could also be a small amount of residual compressive strain at the growth temperature due to kinetic reasons. Therefore, the real tensile strain accumulated in the Ge film is expected to be smaller than the theoretical value.

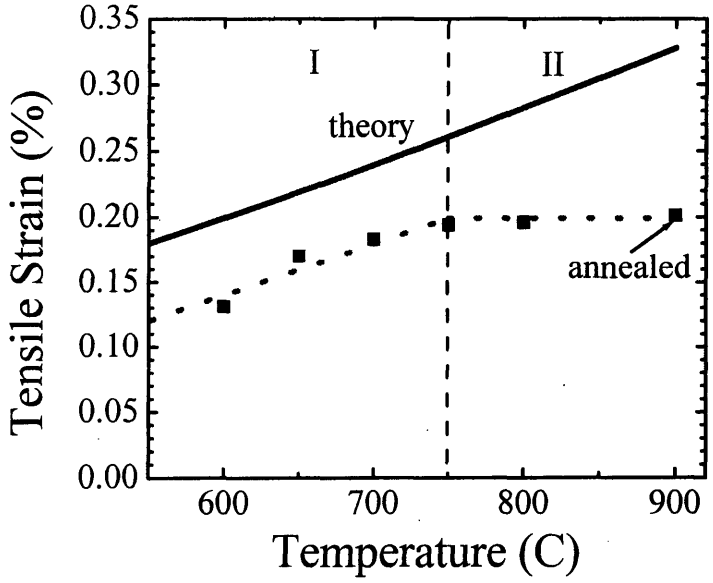

Fig. 2. 3 Comparison of theoretical and experimental thermal strain in Ge films grown or annealed at different temperatures

2.1.2 Measurement of Tensile Strain in Ge Epitaxial films on Si [40, 41, 46]

Epitaxial Ge films were deposited by a two-step UHVCVD on double side polished, 4-inch B doped p^+ Si(100) substrates with a resistivity of 0.001~0.002 Ω cm . Low temperature buffer layers of ~50 nm were deposited at 335°C to achieve planar growth, followed by high temperature depositions at 600, 650, 700 and 800°C, respectively, to obtain different tensile strain in the Ge epitaxial films. Details of this growth method were reported by Luan et al [10]. The film thickness ranges from 1.3 μm

to 1.7 μm, as determined by Rutherford backscattering (RBS). The surfaces of the Ge epitaxial films are smooth, with ~1nm root mean square roughness as revealed by atomic force microscopy (AFM). The threading dislocation density of the as-grown films is ~$8\times10^8/cm^2$, as determined by transmission electron microscopy (TEM). The Ge films are nominally undoped, and the secondary-ion mass spectrometry (SIMS) shows a residual B concentration of ~$10^{14}/cm^3$, most likely due to the B diffusion from the p^+ Si substrate during the growth. To further increase the strain in the front side Ge film, the backside Ge was etched off by H_2O_2 followed by the deposition of Ti films of 1.2-1.5μm on the backside of the wafer and rapid thermal annealing (RTA) to form 3.0-3.8μm of C54-$TiSi_2$. The large tensile stress (~2GPa) in the C54-$TiSi_2$ film induces a slight bending of the wafer toward the backside and further enhances the strain in the front-side Ge film by ~0.05%. Details of this backside silicidation process will be discussed in Section 2.1.4.

X-ray diffraction (XRD) was employed to measure the strain in the Ge epitaxial films experimentally. Samples ~$1\times1cm^2$ in sizes were cut from the wafer for XRD analysis. The XRD was carried out on a Rigaku 250mm high resolution Bragg Brettano diffractometer with Cu K_α irradiation. The strain in the epitaxial Ge films was measured by comparing the Ge(400) and (422) peak positions in $\theta-2\theta$ XRD step scans of the Ge thin films with a lightly doped n-type 2-inch Ge(100) single crystal wafer. The XRD step scan was carried out at 0.002° per step with a data collection time of 2 sec/step. Before each scan of Ge/Si(100) samples, the diffractometer was calibrated in such a way that the $K_{\alpha1}$ diffraction peak of Si(400) from the substrate was maximized and at its theoretical position (θ=34.566°).

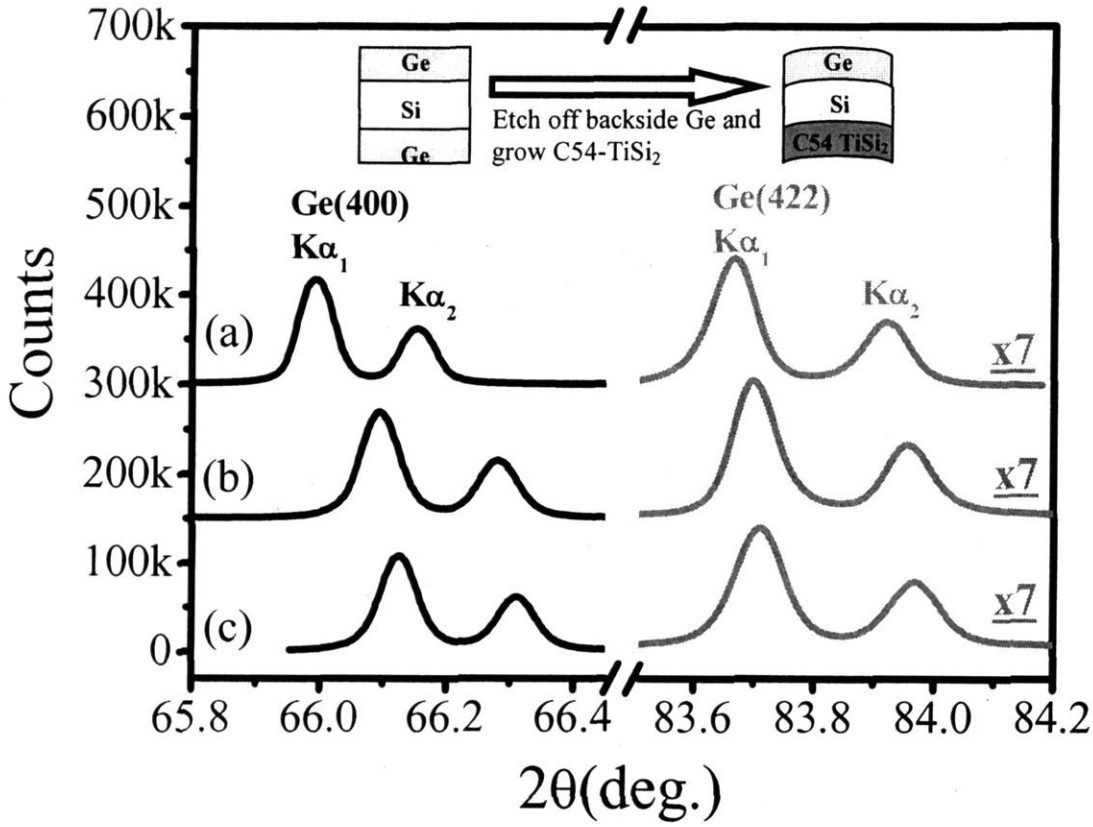

Fig. 2. 4 Ge (400) (black lines) and (422) (gray lines) X-ray diffraction peaks of : (a) bulk Ge(100) wafer, (b) Ge on Si grown at 700°C, and (c) Ge/Si/3.0 μm C54-$TiSi_2$. The intensity of the Ge(422) peaks is magnified by a factor of 7. The shift of the peaks to higher 2θ angles in (b) and (c) compared with (a) indicates the existence of tensile stress in the Ge epitaxial films on Si. The inset of the figure schematically shows the backside silicidation process.

The strain in the Ge epitaxial films on Si was calculated from the XRD data. As representative examples, Fig. 2.4 shows the Ge(400) and (422) diffraction peaks of the bulk Ge(100) sample, the Ge/Si sample grown at 700°C and the Ge/Si/3.0μm C54-$TiSi_2$ sample. The (400) peaks of Ge epitaxial films shift significantly to higher 2θ angles with respect to the bulk Ge sample, indicating the existence of tensile stress in the Ge films. The $K_{\alpha 1}$ peak positions were determined by the parabolic top method and used to

Table 2.2. Summary of strain and direct band gap data obtained in XRD and PR studies.

Ge growth temperature (°C)	Backside C54-$TiSi_2$ thickness (μm)	ε_{400} (%)	ε_{422} (%)	$\varepsilon_{\parallel}$ (%)	$\varepsilon_{\perp}$ (%)	$\frac{\varepsilon_{\parallel}}{\varepsilon_{\perp}}$	$E_g^{\Gamma}(lh)$ (eV)	$E_g^{\Gamma}(hh)$ (eV)
600	N/A	-0.0977 ±0.0013	-0.0213 ±0.0010	0.131 ±0.004	-0.0977 ±0.0013	-1.34 ±0.06	0.7815 ±0.0005	0.7903 ±0.0006
650	N/A	-0.1298 ±0.0015	-0.0298 ±0.0010	0.170 ±0.004	-0.1298 ±0.0015	-1.31 ±0.05	0.7758 ±0.0006	0.7873 ±0.0006
700	N/A	-0.1390 ±0.0015	-0.0318 ±0.0011	0.183 ±0.004	-0.139 ±0.0015	-1.32 ±0.04	0.7743 ±0.0005	0.7863 ±0.0005
800	N/A	-0.1452 ±0.0014	-0.0314 ±0.0012	0.196 ±0.005	-0.1452 ±0.0014	-1.35 ±0.05	0.7727 ±0.0004	0.7852 ±0.0005
800	3.0	-0.1805 ±0.0015	-0.0403 ±0.0010	0.240 ±0.004	-0.1805 ±0.0015	-1.33 ±0.03	0.7656 ±0.0007	0.7815 ±0.0005
800	3.8	-0.1846 ±0.0015	-0.0394 ±0.0012	0.251 ±0.005	-0.1846 ±0.0015	-1.36 ±0.03	0.7640 ±0.0007	0.7805 ±0.0005

calculate the lattice spacing of Ge (400) and (422) planes. The lattice parameter determined for bulk Ge is 0.56580nm, highly consistent with the value reported in literature [47] and indicating the accuracy of our XRD measurements. For the Ge epitaxial films on Si(100), the in-plane strain $\varepsilon_{\parallel}$ and the strain perpendicular to the film $\varepsilon_{\perp}$ can be determined from the XRD data by:

$$\begin{aligned} \varepsilon_{\perp} &= \varepsilon_{400}, \\ \varepsilon_{\parallel} &= 3\varepsilon_{422} - 2\varepsilon_{400} \quad . \end{aligned} \tag{2.10}$$

Here ε_{400} and ε_{422} are the strain in the [400] and [422] directions of the Ge film, respectively. We also carried out (422) scans of the Ge epitaxial film in two orthogonal directions, i.e. [011] and $[01\bar{1}]$, to check any strain relaxation anisotropy. Within the range of experimental error, no anisotropy in the strain relaxation was observed. Therefore, $\varepsilon_{\parallel}$ is isotropic in the plane of the Ge film. Table 2.2 summarizes $\varepsilon_{\parallel}$ and $\varepsilon_{\perp}$ of

each sample. In theory, we have $\varepsilon_{\parallel}/\varepsilon_{\perp}$ = $-C_{11}/(2C_{12})$=-1.33 under biaxial stress, using C_{11}=128.5GPa and C_{12}=48.3GPa for bulk Ge [27]. In our measurements we found $\varepsilon_{\parallel}/\varepsilon_{\perp}$ =-1.33±0.05% for our Ge epitaxial films grown on Si, which is identical to the bulk Ge value within the experimental error. This result again reflects the accuracy of the strain measurements.

The experimentally measured strain in the Ge films is compared to theoretical values in Fig. 2.3. The tensile strain in the Ge layer increases with the growth temperature in the range below ~750°C, similar to the theoretical prediction due to the thermal expansion mismatch. However, the observed strain saturated at ~0.2% above ~750°C. Furthermore, all the observed strains are smaller than the theoretical values. There are two possible mechanisms to cause the smaller tensile strain compared with the theory; (1) the presence of residual compressive strain before the cooling due to the lattice mismatch, even though the film thickness was much more than the critical thickness and (2) the relaxation of tensile strain during the cooling process.

In region I of Fig. 2.3, the observed tensile strain seems to be simply shifted by -0.04 — -0.06% from the theoretical one, as shown by the dashed line. This suggests that the smaller tensile strain in region I is primarily explained by the former mechanism, i.e., a small compressive strain remains at the growth temperature due to the lattice mismatch before the cooling. The residual compressive strain level is about an order of magnitude higher than that predicted from thermodynamic considerations discussed at the beginning of this section (-0.0035 — -0.0065%), indicating there must be some kinetic reasons leading to this residual compressive strain. Although the reason why ~0.04-0.06% compressive strain remains is not completely clear, initial stage of the Ge growth may

play an important role for such a residual compressive strain, since formation of the misfit dislocations at the Ge/Si interface is responsible for the relaxation of lattice mismatch. In the present study, a low temperature buffer layer was used to prevent three-dimensional nucleation of Ge due to the Stranski-Krastanov mode growth [10]. It is possible that this buffer layer could not relax the lattice mismatch entirely due to kinetic barriers, leading to the small compressive strain in the overlying Ge layer. Change in growth condition of the buffer layer (*e.g.*, growth temperature) might change the strain in the Ge layer. However, higher growth temperature for the buffer layer is not preferred since it may induce islanding of the Ge film.

On the other hand, the residual compressive strain cannot explain the saturation of strain in region II (> ~750°C) of Fig. 2.3. This saturation behavior is probably ascribed to the latter mechanism, i.e., relaxation of the tensile strain due to the thermal expansion mismatch during the cooling process. If this relaxation always occurs above ~750°C, accumulation of the tensile strain due to the thermal expansion mismatch is limited below ~750°C. This leads to a constant strain in region II, which is equal to the strain for T = ~750°C, i.e., 0.20% tensile strain in the Ge film. This relaxation model implies that rearrangement of the dislocations in the Ge layer (plastic deformation) occurs mostly above ~750°C. In fact, there is a one-to-one correspondence with the motion of threading dislocations. It has been shown in Ref. [10] that the density of threading dislocations is reduced from 10^9 cm^{-2} to 10^7 cm^{-2} by the cyclic post-growth annealing between a high temperature of 900°C and a low temperature of either 780°C or 100°C due to the coalescence of threading dislocations. In this annealing, the difference of the low temperature (780°C or 100°C) did not show significant difference of the threading

dislocation density. This indicates that the motion of threading dislocations mostly occurs above ~780°C, which is almost equal to the temperature of ~750°C for the onset of strain saturation. Therefore, such a temperature-dependent rearrangement of dislocations should be responsible for the strain saturation above ~750°C.

2.1.3 Measurement of the Direct Band gap of Ge by Photoreflectance [40,41,48]

Photoreflectance (PR) measurement was employed to determine the direct band gap of the Ge films. The same samples used in XRD were subjected to PR measurement to establish a one to one correspondence between the direct band gap of Ge and the in-plane strain $\varepsilon_{\parallel}$. Fig. 2.5 shows the set up for PR measurement. A 488nm Ar laser with a power of 10 mW was used as the pump source and was modulated at a frequency of 201Hz by a chopper to achieve electric field modulation on the sample surface by injecting carriers into the Ge film. A halogen lamp with scanning monochrometer was used as the light source for reflectance measurements. The monochrometer scanned at 0.5 nm/step and the data collection time was 60 sec/step. Due to the modulation of pump laser, the reflectance of the Ge film at wavelengths near its direct band edge can be modulated. A photodetector collected the reflectance signal and fed an electrical signal into a multimeter and an lock-in amplifier. The multimeter measured the DC part of the reflectance $\overline{R} = \frac{1}{2}(R_{on} + R_{off})$, i.e., the average reflectance between pump on and pump off, while the lock-in amplifier was synchronized with the chopper and measured the absolute change in reflectance (AC part) $\Delta R = R_{on} - R_{off}$. Since usually $\Delta R << R_{off}$, we have $\overline{R} \approx R_{off} \approx R_{on}$. By plotting the relative change in reflectance $\Delta R / \overline{R}$ vs.

wavelength near the direct band edge of Ge, we can obtain the information on the direct band gap of Ge.

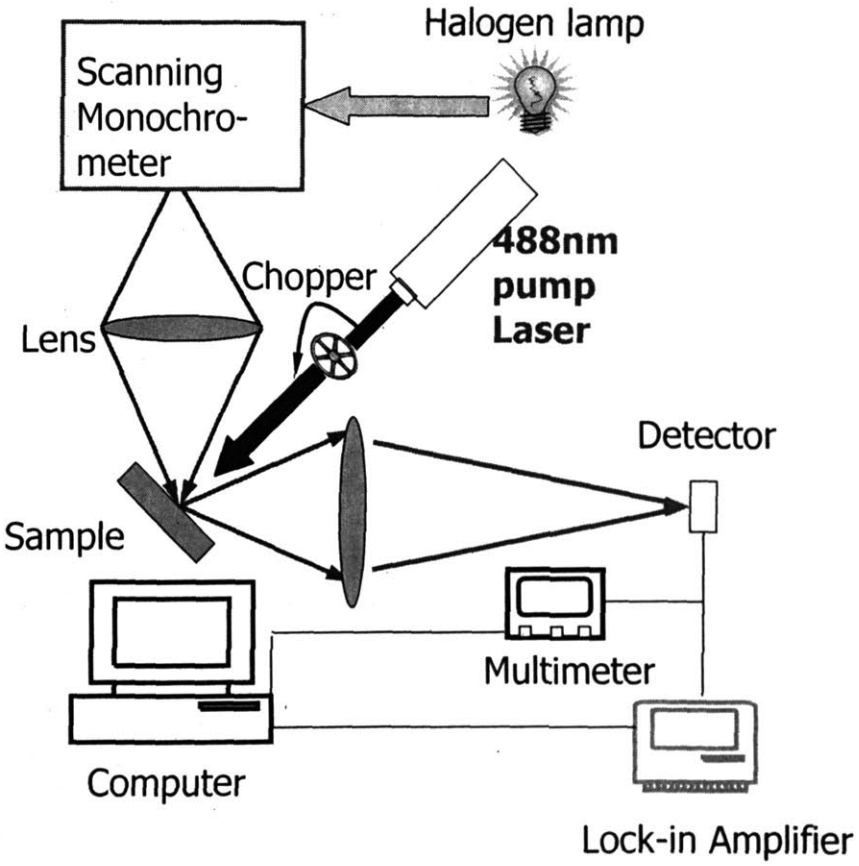

Fig. 2. 5 Schematic diagram of the experimental set-up for photoreflectance measurement.

Fig. 2.6 explains the basic physics of photoreflectance measurement. When intrinsic Ge film is grown on p^+ Si substrate, a built-in electric field is induced in the Ge layer due to the requirement of equalizing Fermi levels in Ge and Si. For simplicity without losing the basic physical principles, we just consider a uniform electric field in Ge layer. The absorption of Ge can be modified by the electric field. For example, without electric field a photon with an energy ($\hbar\omega$) smaller than the direct band gap

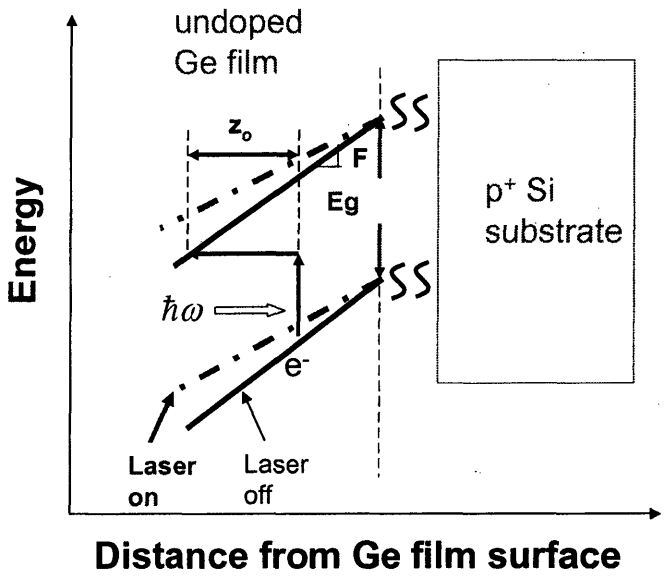

Fig. 2. 6 Physical principle of photoreflectance measurement

(E_g^Γ) cannot excite an electron from the valence band to the conduction band. However, with an electric field this transition could happen at certain probability since an electron can absorb this photon energy and then tunnel through a triangular potential barrier to reach the bottom of the conduction band (Fig. 2.6). Therefore, the absorption is enhanced for photon energies smaller than the direct band gap. When $\hbar\omega << E_g^\Gamma$, however, even with the electric field the potential barrier is still too high to overcome so that the absorption enhancement is negligible. When $\hbar\omega >> E_g^\Gamma$, the photon can always achieve the transition whether there is an electric field or not. Therefore, the effect of electric field is especially pronounced for photon energy around the direct band gap ($\hbar\omega \sim E_g^\Gamma$). For photon energy slightly smaller than the direct band gap we can observe a pronounced enhancement in absorption. By considering the classical quantum mechanical problem of an electron passing through a potential barrier, we can also qualitatively understand that

for photon energy slightly larger than the bandgap the transition probability oscillates with photon energy due to its interference with the potential barrier. This oscillation is called Franz-Keldysh oscillation. Due to Kramer-Kronig relation, any change in absorption also induces a change in the real part of refractive index, so does the reflectance of the material. Therefore, a modification of the built-in electric field in the Ge layer also changes its reflectance. When a 488 nm pump laser is shone on the surface of the sample, electrons and holes are generated by photons, and they drift under the built-in electric field in such a way as to weaken the build-in field. Therefore, the absorption coefficient, refractive index and reflectance can be modulated by the 488 nm pump laser. The incident light intensity from the monochrometer for reflectance measurement, on the other hand, is about three orders of magnitude weaker than the 488 nm laser. Therefore, it plays a negligible role in modifying the electric field. This is why the lock-in amplifier is only synchronized to the pump laser to monitor the change in reflectance. By monitoring the relative change in reflectance ($\Delta R / \overline{R}$) vs. wavelength and analyzing the data with adequate physical models, we can obtain the direct band gap of Ge.

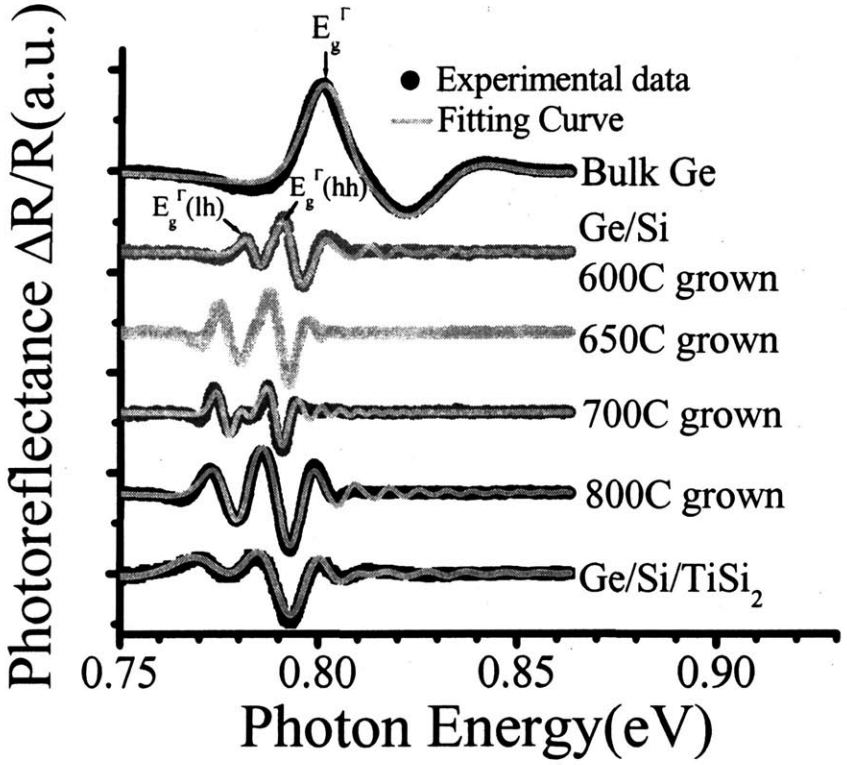

Fig. 2. 7 Photoreflectance spectra of Ge/Si samples grown at different temperatures and fitting with generalized Franz-Keldysh theory.

The PR data of bulk Ge and epitaxial Ge films are shown in Fig. 2.7. The PR data of the bulk Ge shows a peak at 0.8 eV, corresponding to the direct gap of Ge. Some Franz-Keldysh oscillations following the peak can also be observed. The spectrum is fit with the conventional third derivative spectroscopy model since the surface electric field in bulk Ge is usually low [49]. The fitting gives E_g^{Γ}=0.8005±0.0007 eV for the unstressed bulk Ge, in good agreement with the literature and attesting to the accuracy of our PR measurement system [27]. On the other hand, the PR spectra of tensile strained epitaxial Ge on Si show two peaks since the light and heavy hole bands become non-degenerate under tensile strain. The relatively small peak at lower energy corresponds to $E_g^{\Gamma}(lh)$,

while the one adjacent to it at higher energy and higher intensity corresponds to $E_g^{\Gamma}(hh)$. The difference in peak intensity is due to the less joint density of states of light hole transition compared to that of heavy hole. One can see some Franz-Keldysh oscillations after the heavy hole transition peak, while those of the light hole transition are overlapped with the spectra of the heavy hole and cannot be easily seen directly. We can still catch a glimpse of the Franz-Keldysh oscillations after the light hole transition peak in the sample grown at 700°C, though. For the Ge epitaxial films on p^+ Si, there is a significant built-in electric field and the third derivative model (low field approximation) cannot fit the data so well anymore. Therefore, the PR data from Ge epitaxial films on Si were analyzed by the generalized Franz-Keldysh theory developed by Shen et al [50,51]. For the fundamental band gap transitions (wave vector k=0),

$$\Delta R / R \propto \mathrm{Re}(\delta\varepsilon), \tag{2.11}$$

where $\delta\varepsilon$ is the change in the dielectric constant given by

$$\delta\varepsilon(\hbar\omega, F_{dc}, F_{ac}) = \varepsilon(\hbar\omega, F_{dc}) - \varepsilon(\hbar\omega, F_{dc} - F_{ac}) = \Delta\varepsilon(\hbar\omega, F_{dc}) - \Delta\varepsilon(\hbar\omega, F_{dc} - F_{ac}). \tag{2.12}$$

In Eq. 2.12, $\hbar\omega$ is the incident photon energy, F_{dc} is the built-in electric field in the intrinsic Ge epitaxial film grown on p^+ Si(100) without illumination, and F_{ac} is the electric field induced by the ac modulation of the chopped pump laser. Here $\varepsilon(\hbar\omega, F_{dc})$ denotes the dielectric constant of the Ge material when the pump laser is off. As mentioned earlier, the electric field in the Ge layer is decreased when the pump laser is shone on the surface of the material due to the screening of photon-generated carriers. Therefore, the electric field is decreased to $F_{dc} - F_{ac}$ when the pump laser is shone on the Ge surface and $\varepsilon(\hbar\omega, F_{dc} - F_{ac})$ denotes the dielectric function of the material when the pump laser is on. In Eq. 2.12,

$$\Delta\varepsilon(\hbar\omega,F)=\varepsilon(\hbar\omega,F)-\varepsilon(\hbar\omega,0)\,. \tag{2.13}$$

In our case, as the light and heavy hole valence bands of Ge become non-degenerate under biaxial stress, the spectrum is the sum of contributions from light and heavy hole band transitions, characterized by band gaps $E_g^{\Gamma}(lh)$ and $E_g^{\Gamma}(hh)$, respectively. Therefore, we have

$$\Delta\varepsilon(\hbar\omega,F)=(1/(\hbar\omega)^2)\{B_{lh}(\hbar\theta_{lh})^{1/2}[G(\eta_{lh})+iF(\eta_{lh})]+B_{hh}(\hbar\theta_{hh})^{1/2}[G(\eta_{hh})+iF(\eta_{hh})]\}\,, \tag{2.14}$$

where B_{lh} and B_{hh} are constants for light and heavy hole transitions, respectively. These parameters are related to the transition matrix element of the direct gap of Ge; $G(\eta)$ and $F(\eta)$ are electro-optic functions given by

$$G(\eta)=\pi[Ai'(\eta)Bi'(\eta)-\eta Ai(\eta)Bi(\eta)]+\eta^{1/2}H(\eta)\,,$$

$$F(\eta)=\pi[Ai'^2(\eta)-\eta Ai^2(\eta)]-(-\eta)^{1/2}H(-\eta) \tag{2.15a}$$

where

$$\eta_{lh}=[E_g^{\Gamma}(lh)-\hbar\omega-i\gamma_{lh}]/\hbar\theta_{lh}\,,$$

$$\eta_{hh}=[E_g^{\Gamma}(hh)-\hbar\omega-i\gamma_{hh}]/\hbar\theta_{hh}\,, \tag{2.15b}$$

$H(\eta)$ is the unit step function (i. e. $H(\eta)=1$ if $\eta\geq 0$ and $H(\eta)=0$ if $\eta<0$), and $Ai(\eta), Bi(\eta), Ai'(\eta), Bi'(\eta)$ are the Airy functions and their derivatives. In Eq. 2.15b, γ_{lh} and γ_{hh} are the temperature broadening factors of light and heavy hole band transitions, respectively; $\hbar\theta_{lh}$ and $\hbar\theta_{hh}$ are the electro-optical energies of light and heavy hole band transitions, respectively, given by

$$\hbar\theta_{lh}=(e^2\hbar^2F^2/2m_{r,lh})^{1/3}\,,$$

$$\hbar\theta_{hh} = (e^2\hbar^2F^2 / 2m_{r,hh})^{1/3}, \tag{2.16}$$

where e is the electron charge, and $m_{r,lh}$ and $m_{r,hh}$ are the reduced effective mass of electron-hole pairs of light and heavy holes, respectively. Note that $m_{r,lh} = \frac{m_e^{\Gamma} m_{lh}}{m_e + m_{lh}}$, $m_{r,hh} = \frac{m_e^{\Gamma} m_{hh}}{m_e + m_{hh}}$, where m_e^{Γ}=0.038 m_0 is the electron effective mass in the Γ *valley* instead of L valley [27]. The effective masses of holes are $m_{hh} = 0.33m_0$, and $m_{lh} = 0.043m_0$ [27]. Roughly speaking, $\hbar\theta_{lh}$ and $\hbar\theta_{hh}$ are related to the energy bequeathed to the electron-hole pairs by the electric field. The higher the electric field, the higher the electro-optical energy and the easier the tunneling process happens. As we can see from Eqs. 2.15 and 2.16, the numerators in η_{lh} and η_{hh} are related to the height of the triangular potential barrier, while the denominators are related to the width of the potential barrier. The smaller the numerators, the lower the potential barrier; the larger the denominator, the narrower the potential barrier. Therefore, the parameters η_{lh} and η_{hh} completely describes the characteristics of the potential barrier in the band to band transition in the presence of an electric field. This is why they are the major variables in determining the change in dielectric function under an electric field. The electro-optical functions $G(\eta)$ and $F(\eta)$ are related to Airy functions and their derivatives. Airy functions appear in the solution of a tunneling problem, and $G(\eta)$ and $F(\eta)$ are just mathematical formula that describe this tunneling process given the information of the potential barrier described by η. With Eqs. 2.11—2.16, we are able to fit the PR spectra of epitaxial Ge films on Si (see Fig. 2.7). This model fits the experimental data quite well, with correlation coefficients greater than 0.98. It should be noted that the electric field

and broadening factors obtained from the fitting may not be unique, since these two parameters can compensate the effect of each other to some extent. However, since the PR spectra have sharp peaks and valley that are characteristic of the positions of band edges, the band gaps obtained from the fitting are unique and the error is in the order of ~0.0005 eV. The derived bandgaps $E_g^{\Gamma}(lh)$ and $E_g^{\Gamma}(hh)$ are presented in Table 2.2.

2.1.4 Deformation Potential Constants of Tensile Strained Ge on Si

With tensile strain data from XRD and direct band gap data from PR, it seems we can plot the direct band gap of Ge vs. tensile strain, and derive the deformation potential constants from this relation. However, one has to be careful when relating the direct bandgap values at the Γ point measured by PR to the strain measured by XRD. X-ray is able to penetrate the whole Ge film and the strain measured by XRD is an average over the depth of the film. In PR measurements, however, the probed depth is determined by the carrier diffusion length [52], which can be smaller than the depth of the films. From the p-i-n diode performance of our epitaxial Ge/Si photodetectors, we derived that the carrier mobility and life time were 3500cm^2/V sec and 0.8ns, respectively, for cyclic annealed Ge films with a threading dislocation density of ~2×10^7/cm^2 [53]. Since the minority carrier lifetime is known to be inversely proportional to the dislocation density in Ge [54], we estimate the minority carrier life time of the Ge epitaxial films used in this study (with a threading dislocation density of ~8×10^8/cm^2) is ~0.02ns. It is also known that the carrier mobility and diffusivity in Ge at room temperature are relatively insensitive to the dislocation scattering up to a dislocation density in the order of 10^8/cm^2 [55]. Actually, the carrier diffusivity parallel to the dislocations, $D_{\|}$=400±100cm^2/sec, is

greater than that in dislocation-free Ge (100cm^2/sec), while the diffusivity perpendicular to the dislocations, $D_\perp$=80±30cm^2/sec, is slightly smaller than that in dislocation-free Ge. Even with the lower limit of $D_\perp$ (50 cm^2/sec), we still get a carrier diffusion length of $L = \sqrt{D\tau}$ ~300nm. Note that in our samples the carrier diffusion length should be greater than this value, because in PR measurements the carriers diffuse in the direction perpendicular to the film, which is mostly parallel to the threading dislocations. This means the real diffusivity should be closer to $D_\parallel$ and greater than $D_\perp$. Therefore, we can conclude that the probing depth of PR, determined by the carrier diffusion length, is at least 300nm. If there were significant surface stress relaxation in the Ge films typically characterized by the formation of a wavy surface or islanding, then the strain in the top 300nm Ge surface layer would be smaller than that measured by XRD and we would not be able to relate the bandgaps measured by PR to the strain measured by XRD. In our case, AFM has confirmed that the surfaces of the Ge epitaxial films used in this study are very smooth, with a root mean square roughness of ~1nm, i.e. there is no sign of surface stress relaxation or islanding in the epitaxial Ge films and the roughness is much smaller than the detection depth (>300nm) of PR. Therefore, it is safe to state that the strain in the top 300nm of the Ge film should not be affected by the trivial surface roughness, and that it is valid to establish a one to one correspondence between the direct bandgap of Ge and the in-plane strain $\varepsilon_\parallel$ from our experimental results.

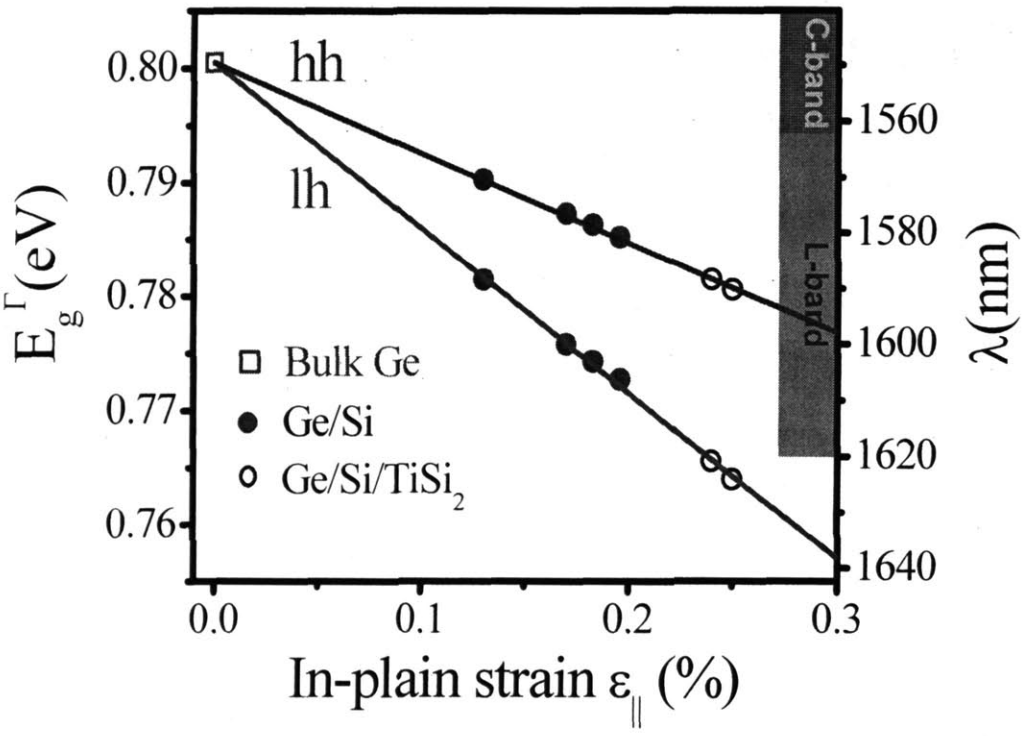

Fig. 2. 8 Direct band gap vs. tensile strain obtained by XRD and PR measurements

The relationship between the direct bandgaps, $E_g^{\Gamma}(lh)$ and $E_g^{\Gamma}(hh)$, and the in-plane strain $\varepsilon_{\parallel}$ is plotted in Fig. 2.8. With 0.25% tensile strain the direct band gap is decreased to 0.764 eV, corresponding to 1625 nm. Therefore, the absorption of Ge in the L band is greatly enhanced. By fitting the experimental data in Fig. 2.8 with Eq. 2.1 (note in Eq. 2.1, $\varepsilon_{\perp}$ can be substituted by $\varepsilon_{\perp} = -\varepsilon_{\parallel}/1.33$ as shown in Table 2.2), we obtain a=-8.97±0.16eV and b =-1.88±0.12eV. The error bars of a and b are determined in the following way: to reflect the effect of the error bars of each data point in Fig. 2.8 on the uncertainties of a and b, we have written a computer code to generate randomly 10000 sets of E_g^{Γ}(lh) and E_g^{Γ}(hh) vs. $\varepsilon_{\parallel}$ data within their error bars listed in Table 2.2, do a

curve fit for each set of data to get a and b, and finally do a statistics on the distribution of a and b due to the variation of the experimental data points within their error bars. The average values of a and b are -8.97 and -1.88eV, respectively. Ninety per cent of the data fall into the range of a=-8.97±0.16eV and b=-1.88±0.12eV. Therefore, the deformation potential constant data obtained above guarantee 90% confidence. These values are compared with earlier experimental data from literature in Table 2.1. All the literature values were measured from either hydrostatic or uniaxial compression tests of single crystal Ge samples. Looking through Table 2.1, the a value obtained in this work is more consistent with Ref. [31] (uniaxial compression test, room temperature) and Ref [32] (hydrostatic compression test, room temperature). The value of $|b|$ obtained in this work is consistent with the lower values reported in literature, i.e. Refs [36] and [37]. As can be seen from Table 2.1, the deformation potential constants reported in literature varied significantly, with the highest reported values greater than the lowest ones by as much as ~50%. This large dispersion may result from the non-uniformity of the stress in the samples, especially in the uniaxial compression tests where the samples tend to bend and deviate from the ideal uniaxial compression. In our samples, the biaxial tensile stress in the Ge epitaxial films was induced by the thermal mismatch between Ge and Si, which gives more uniform stress in the Ge material. While previous measurements sampled a large range of strain up to several percent, the current work has more data points in the small strain regime (<0.25%), which is more consistent with the basic assumptions of deformation potential theory, i.e., the strain Hamiltonian is much less than the spin-orbit Hamiltonian. The XRD method used in the present study also gives a rather accurate measurement of small strains. Thus, the error bars of the deformation potential constants

in this work are smaller than most previous experimental reports. To the best of our knowledge, the deformation potential values a and b are obtained for the biaxially tensile stressed Ge for the first time. The deformation potential constants obtained in this study are especially suitable for the design of electronic and optoelectronic devices based on epitaxial Ge and SiGe, for these planar devices are exactly in the biaxial stress state.

2.1.5 Engineering Tensile Strain in Ge films [56]

As mentioned above, due to strain relaxation the tensile strain in as-grown Ge films is limited to 0.20% for growth temperatures >750°C. It would be desirable to increase the tensile strain in the Ge films by some means. In this section we describe two different methods of increasing the tensile strain in Ge films: (1) backside silicidation, and (2) post growth annealing.

Silicidation has been widely used in CMOS technology to decrease the contact resistance of source, drain, and gate regions [57]. Metal silicides are typically formed by depositing metal (Ti, Co, Ni, etc) on Si followed by silicidation annealing ranging from 600 to 900°C. C54-$TiSi_2$ has been the most commonly used silicide in ultra-large scale integrated circuits (ULSI) due to its low resistivity (14μΩ•cm). It has also been found that the C54-$TiSi_2$ grown on Si shows a large tensile stress, typically ~2GPa [58,59], mainly due to the thermal mismatch between silicide film and Si substrate. Substrate being the same, the curvature induced by the stress of the film is proportional to the magnitude of the stress σ_{film} and the thickness t_{film} of the film [60]. The process of backside silicidation is schematically shown in the inset of Fig. 2.9. Ge films with a thickness of

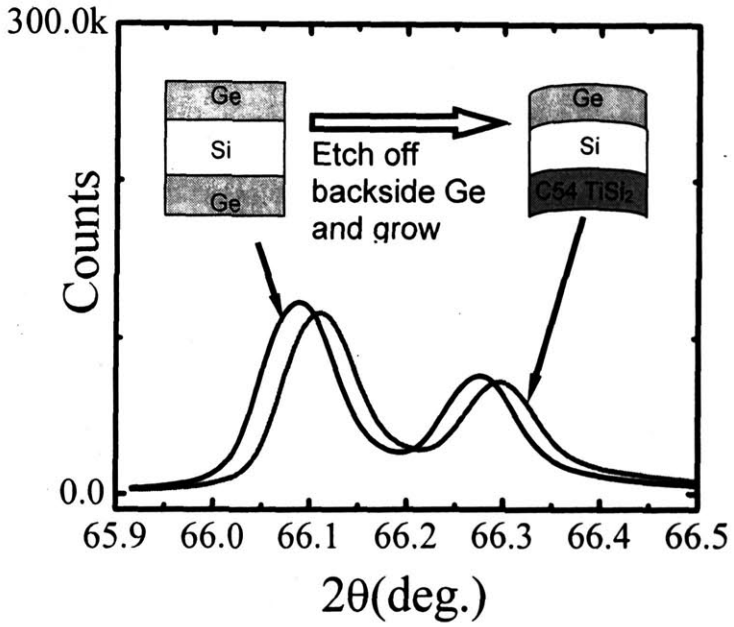

Fig. 2. 9 X-ray diffraction patterns of Ge(400) peaks of Ge/Si(100)/Ge sample and Ge/Si(100)/C54-$TiSi_2$ sample, showing 0.036%±0.006% increase in strain after backside silicidation. The inset shows the process of backside silicidation schematically.

1.3 μm were epitaxially grown on p^+ Si(100) wafers by UHVCVD via a two step growth, as mentioned earlier. In UHVCVD process, Ge films are equally deposited on both sides of the Si wafer so that the wafer is nominally flat. We refer to these samples as Ge/Si/Ge. The Ge film on the backside was then removed by H_2O_2. During this etching process, the front side Ge film was protected by photoresist. After etching, the sample was heated on a hot plate to melt the wax, followed by ultrasonic cleaning in acetone to remove the photoresist. XRD confirms that the backside Ge was completely removed while the front side Ge was intact after the etching. A 1.2 μm Ti layer was then deposited on the backside of the wafer by evaporation and the sample was annealed by rapid thermal annealing (RTA) at 800°C for 5min in N_2 for silicidation. XRD shows that the resulting C54-$TiSi_2$ was polycrystalline without obvious texture. We refer to these samples as

Ge/Si/C54-$TiSi_2$ in the later text. The thickness of the resulting C54-$TiSi_2$ was ~3 μm, which was greater than that of the front side Ge film. Since the stress in the silicide layer (~2 GPa) was also much larger than that in front side Ge (~0.28GPa corresponding to 0.2% in-plane strain), we have $\sigma_{TiSi_2} t_{TiSi_2} >> \sigma_{Ge} t_{Ge}$. Therefore the wafer bends toward the backside and changes into a convex shape. Compared with the case of Ge/Si/Ge sample, the tensile strain in the front side Ge layer would be increased. Since the stress in Ge and C54-$TiSi_2$ films [61] are both thermal stress in nature, assuming both the Ge and the C54-$TiSi_2$ are relaxed during the silicidation process at 850°C and using t_{TiSi_2} , $t_{Ge} << t_{sub}$ (thickness of Si substrate, ~500 μm), the in-plane strain increase in the Ge layer at room temperature induced by the backside silicidation can be derived as:

$$\Delta\varepsilon_{\parallel}(Ge) = \frac{3\Delta T}{t_{sub} M_{Si}} (\Delta\alpha_1 t_{TiSi_2} M_{TiSi_2} - \Delta\alpha_2 t_{Ge} M_{Ge}), \qquad (2.17)$$

where ΔT is the difference between the silicidation temperature and room temperature, M_{Si}=180GPa, M_{Ge}=140GPa [62], and M_{TiSi_2}=342GPa [63] are the biaxial modulus of Si(100), Ge(100) and polycrystalline $TiSi_2$, respectively; α is the thermal expansion coefficient and $\Delta\alpha_1 = \alpha_{Si} - \alpha_{TiSi_2}$ =-10^{-5}/K, [64] $\Delta\alpha_2 = \alpha_{Si} - \alpha_{Ge}$ =-2.5×10^{-6}/K [65]. The calculation with Eq. 2.17 shows that such a backside silicidation would increase the strain in the front side Ge film by ~0.03%.

Fig. 2.9 shows the XRD spectra of front side Ge (400) peaks of Ge/Si/Ge and Ge/Si/C54-$TiSi_2$ samples. For the as grown sample, the strain was 0.204±0.004%. After the formation of backside C54-$TiSi_2$ layer, the strain in the front side Ge layer increases by 0.036±0.006% to 0.240±0.004% compared with the as-grown sample. This experimental result agrees with our calculations based on Eq. 2.17, and demonstrates the

strain increase in the front side Ge film induced by backside silicidation. With a thicker C54-$TiSi_2$ film on the backside, the tensile strain in the Ge film can be increased from 0.20 to 0.25% and the direct band gap can be further decreased to 0.764 eV (corresponding to 1625nm), as shown in Fig. 2.8. Therefore, with enhanced tensile strain by backside silicidation, the epitaxial Ge material is applicable to cover the whole L-band in telecommunications. Another advantage is that C54-$TiSi_2$ itself can be used as a back electrode, so it can be integrated into the diode device for lower contact resistance.

An effective way to further enhance the tensile strain in Ge is to locally reduce the thickness of the Si wafer where Ge devices are formed. This way the active material of Ge in the devices can be further tensile-strained while the mechanical support of the Si wafer is not affected since it is only thinned down in local areas of 10-1000 μm^2. If we reduce the thickness of the Si wafer locally from 500 μm to 20 μm, Eq. 2.17 gives a strain enhancement of about 0.75% and the total tensile strain in the Ge layer is increased to ~1.0 %. This can be achieved by etching the Si wafer from the backside with mask alignment to the front side Ge devices. However, this is an upper limit to this method since the strain would eventually lead to the fracture of the Si material. The fracture strain of Si is ~1.5 % in [100] direction [66]. Therefore, the upper limit of strain enhancement by backside silicidation is also ~1.5 % and the upper limit of tensile strain in the Ge layer is ~1.7 %. Correspondingly, the direct gap of Ge can be decreased to 0.66 eV, and the efficient detection range of epitaxial Ge photodetectors on Si can be further expanded up to 1880 nm. It is interesting to note that the calculation from deformation potential theory shows that the indirect gap of Ge at L valley is 0.64 eV at 1.7% tensile strain, only 20 meV smaller than the direct gap. Considering the thermal energy at room temperature is

26 meV, there is practically no difference between the direct and indirect gaps. In this case, the light emitting properties of the Ge material may also be greatly improved. The stressor layer is not limited to C54-$TiSi_2$ in principle. Any material that has a large thermal expansion mismatch to Ge can be used to stress the Ge films.

The tensile strain can also be engineered by post-growth annealing. Fig. 2.10 shows the tensile strain of a sample grown at 600 °C after annealing at 900 °C for different amount of time. The strain initially increases with annealing time, and then saturates at 0.205% for annealing time longer than 40 min. This is because the film gradually relaxes at 900 °C during the annealing. After about 40 min annealing, the film fully relaxes at 900 °C. Upon cooling, it starts to accumulate thermal strain when the temperature decreases below ~750 °C, as mentioned in section 2.1.2. Therefore, about 0.20% tensile strain is accumulated after annealing at 900 °C for >40min. Etching pit density (EPD) shows that the threading dislocation density decreases accordingly, just as the case of cyclic annealing. Therefore, post-growth annealing can increase the tensile strain and decrease the defect density in the Ge film at the same time. If the Ge film is relaxed at >750°C on a substrate with lower thermal expansion coefficient than Si, the strain in the Ge film can be further increased. For example, the thermal expansion coefficient of SiO_2 is only 5×10^{-7} /K. Therefore, for Ge on insulator (SiO_2) or Ge on quartz the thermally induced tensile strain in the Ge layer can be increased to 0.4%, assuming Ge also starts to accumulate strain when the temperature decreases below 750°C. Correspondingly, the effective detection wavelength can be increased to 1675 nm.

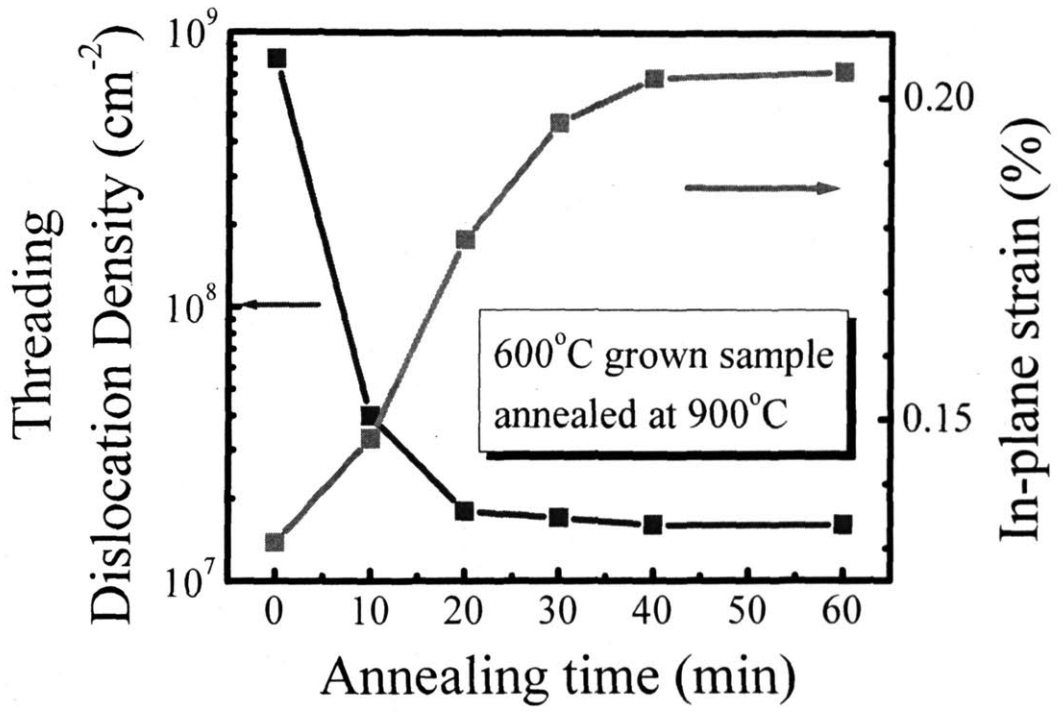

Fig. 2. 10 Tensile strain and threading dislocation density of a Ge/Si sample grown at 600°C as a function of annealing time at 900 °C. The dislocation density was determined by etching pit method.

2.2. Strain in Selectively Grown Ge Structures

Selective growth of Ge on Si is an important technique to offer flexibility and compatibility to integrate Ge optoelectronic devices with Si CMOS devices. It is interesting to understand how the shapes and sizes of the selectively grown Ge mesas affect the level of strain. In this section, an initial study on the strain in selectively grown Ge mesa structures is presented and its effect on the band structure of Ge is discussed.

2.2.1 Selective growth of Ge on Si

An oxide mask is usually employed for selective growth of Ge on Si. An oxide layer is deposited on top of Si wafer, and windows are opened through the SiO_2 by lithography and etching. When Ge is deposited at a slow enough growth rate, Ge mesas

only grow within the windows where the Si substrate is exposed. It has been proposed that this is due to the reaction between GeH_4 and SiO_2 that forms volatile GeO and retards the nucleation of poly Ge on SiO_2. Indeed, it has been observed in literature that GeH_4 etches SiO_2 [67]. In our study, we have also observed that if a native oxide is left on the surface of the Si wafer during the Ge low temperature buffer layer growth, Ge will not grow on the wafer until the native oxide is etched away by GeH_4. However, this model does not explain why Si_3N_4 can also be used as a mask for Ge selective growth. Therefore, there might be other mechanisms for the selective grow of Ge in the presence of a dielectric mask.

SiO_2 mask is hydrophilic and it catches water drops after dilute HF dip before the growth. The residual water drops on the wafer can cause serious problems and greatly reduce the yield of selective growth. Any tiny water drop would induce a blurry, rough region around it after the growth, since a non-uniform native oxide is often present under the droplet and the Ge growth on it becomes non-uniform. To overcome this problem, a different procedure of pre-growth cleaning is adopted. After HF dip, the wafers are rinsed in DI water and then spun dry without additional rinsing. Then the wafers are introduced into the UHVCVD furnace and baked in H_2 at 850 °C for 10min to remove any residual native oxide on Si. The H_2 pressure during the baking is ~1.0 mTorr. The chamber was then cooled down to 335°C for the low temperature buffer layer growth. The same H_2 flow was maintained during the whole cooling process. After these steps, the rest of the growth parameters and procedures are the same as the regular growth of blanket Ge wafers.

XRD study on the strain of an individual Ge mesa would be very difficult since the size is in the order of 10 μm and the diffraction intensity is too low to surpass the noise level unless a synchrotron X-ray source is focused on the mesa. To make the strain

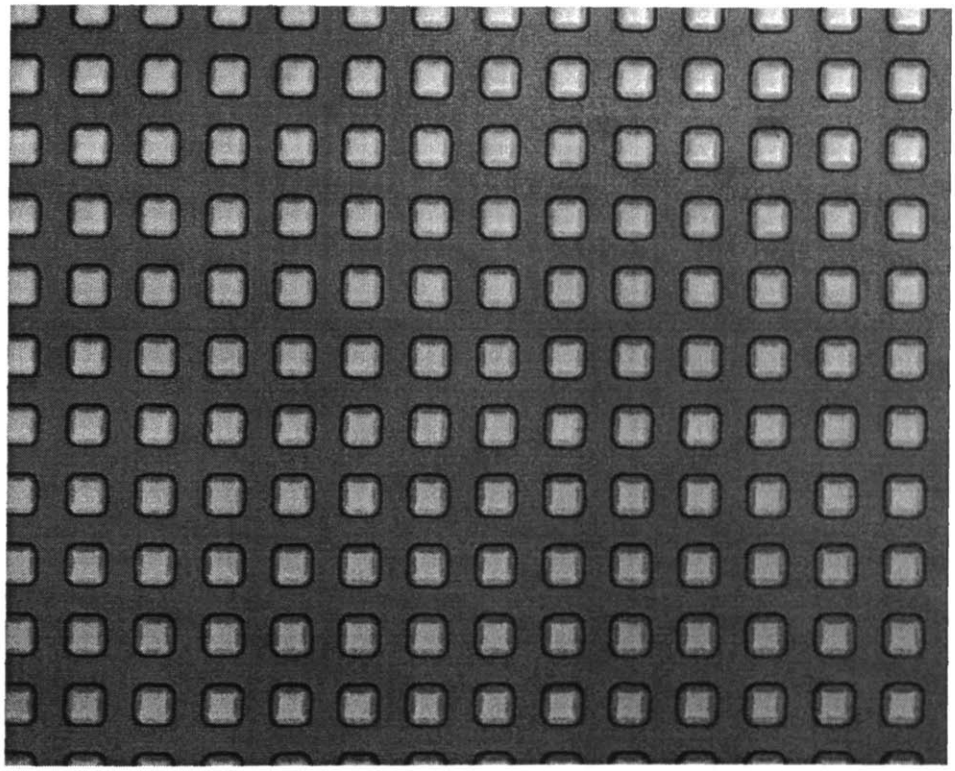

Fig. 2. 11 Optical micrograph of 5×5μm Ge mesas

study on these small Ge mesas easier, we chose to define an array of mesas in a 2.05×2.05 cm^2 region and performed regular XRD on this whole piece of sample. Although the size of each mesa is small, their integral diffraction intensity could be strong enough to produce high quality XRD data. The strain derived from the XRD data is an average of all the mesas. Due to the relatively high accuracy of lithography, we can regard all mesas as exactly the same and this average value should also be very close to the strain in an individual mesa. As an example, Fig. 2.11 shows a micrograph of an array of 5×5μm Ge mesas used in this study. These mesas are separated by a spacing of 5μm

in both x and y directions. Therefore, a large array of 2048×2048 mesas is defined in the 2.05×2.05 cm^2 region. The net area covered by Ge is ¼ of the total area, which is about 1 cm^2. Such a large area is already good enough to produce strong XRD signals. Since the flat of Si wafers are along <110> directions, the edges of the mesas are also along <110> directions due to the alignment of the flat during photolithography. Faceting at the edges of the mesas can be clearly seen, which will be discussed later. With spin drying and H_2 baking before the growth, no water drops were caught on the wafer and the native oxide was completely removed. Therefore, we obtain nearly 100% yield in the selective growth. Fig. 2.12 shows the cross-sectional TEM image at the edge of a 10×10 μm^2 Ge mesa. Three kinds of facets can be clearly identified: (311), (111) and (113). These facets play important roles in the strain relaxation of the selectively grown Ge mesas, as will be discussed in detail later. Fig. 2.13 shows the AFM images of a 5×5 μm^2 and a 10×10 μm^2 Ge mesa. Through the three-dimensional scan of the AFM analysis, we can also identify (311) and (111) facets at the edges of the mesas. Note that the facets take up a much larger proportion of the surface area in the 5×5 μm^2 mesa than in the 10×10 μm^2 one. Therefore, the smaller the mesas, the more the strain relaxation induced faceting. A detailed quantitative analysis will be given in the following section.

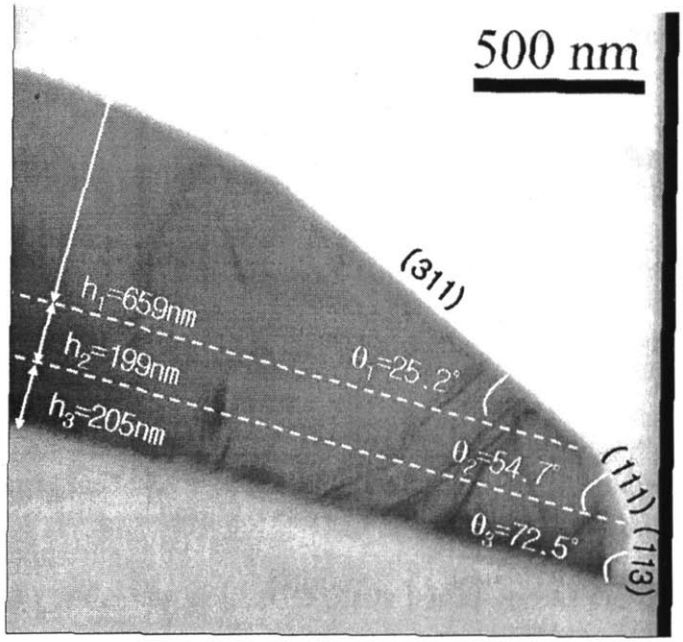

Fig. 2. 12 Cross-sectional TEM at the edge of a 10×10μm Ge mesa. (TEM courtesy of Dr. Jinggang Lu, *North Carolina State University*)

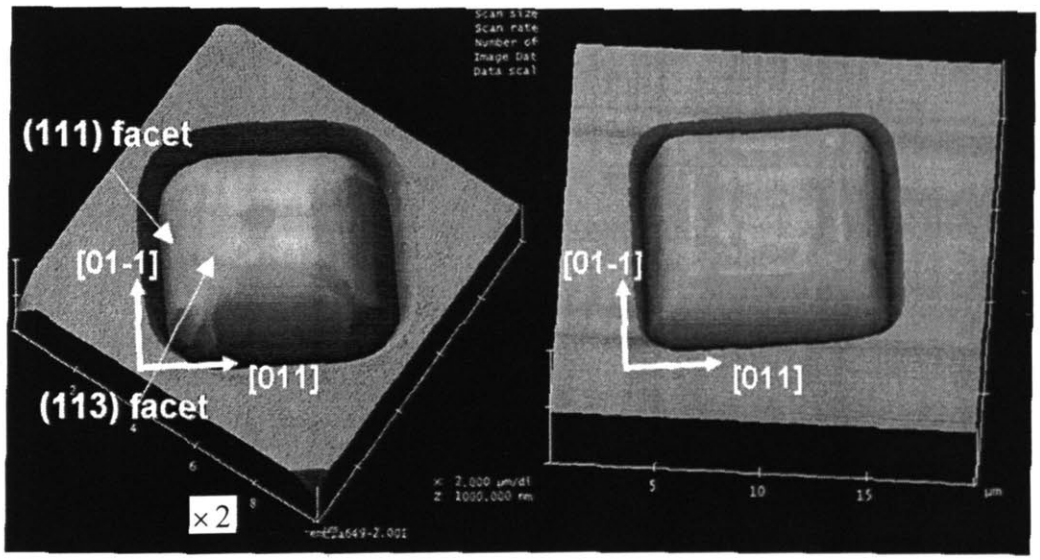

Fig. 2. 13 AFM images of a 5×5 μm² (left) and a 10×10 μm² Ge mesa (right). The 5×5μm² mesa is *magnified by twice in the figure for better comparison* of its shape to that of the 10×10 μm² mesa. The edges of the mesas are along <110> directions. AFM analysis courtesy of Ms. Samerkhae Jongthammanurak

2.2.2 Strain in Selectively Grown Ge Mesas

Fig. 2.14 shows the XRD data of the 5×5μm Ge mesa sample compared to a blanket Ge film sample grown in the same run at 700°C. From the XRD data, we derive a tensile strain of $\varepsilon_{\parallel}$=0.081% for the 5×5μm Ge mesa sample, which is much smaller than the tensile strain in the blanket film grown at the same temperature (0.176%). We also carried out (422) scans of the sample in two orthogonal directions, i.e. [011] and [01$\bar{1}$], to check any strain relaxation anisotropy in the 5×5μm square mesa. Within the range of experimental error, no anisotropy in the strain relaxation was observed. Therefore, this square mesa is also subjected to a uniform in-plane tensile strain, but the level of tensile strain is significantly lower than the blanket film case.

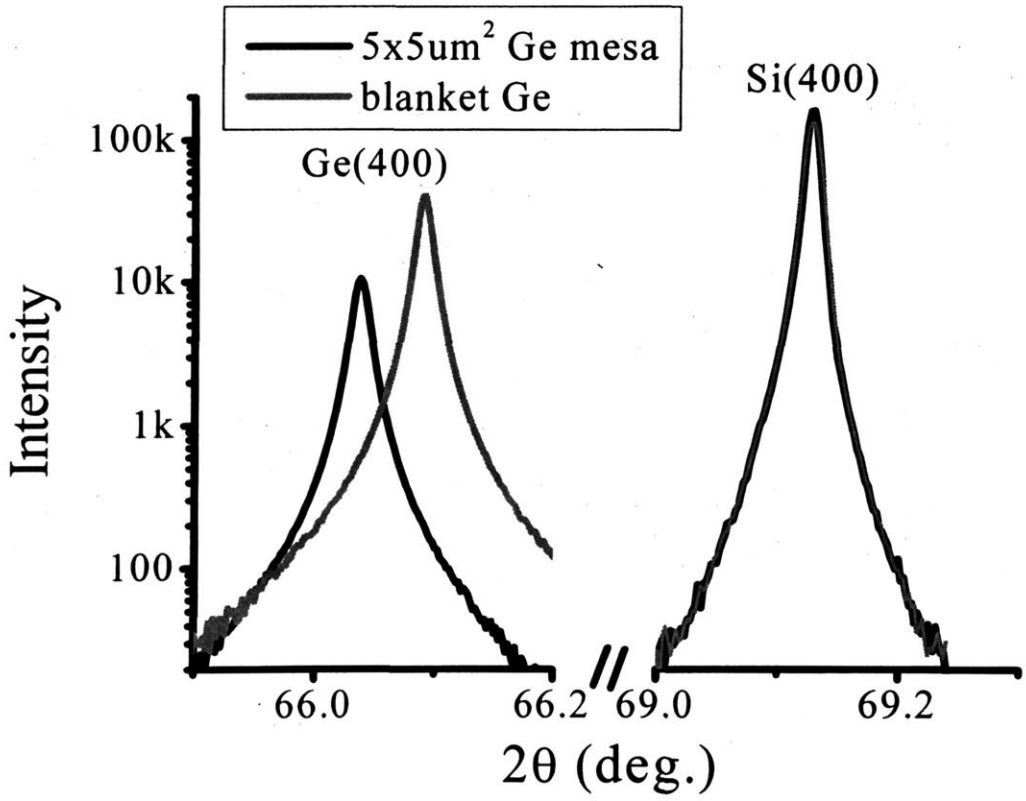

Fig. 2. 14 XRD data of the 5×5μm Ge mesa sample compared to a blanket Ge sample grown in the same run at 700°C.

Fig. 2.15 shows the in-plane tensile strain $\varepsilon_{\parallel}$ as a function of square mesa size for as-grown samples and samples annealed at 900°C for an hour. Interestingly, the strain in the mesas decreases dramatically when the mesa size shrinks below 20μm. There are two possible reasons for strain relaxation: (1) plastic relaxation by generation/extension of misfit dislocations at the Ge/Si interface, and (2) elastic relaxation induced by faceting at the edges of the mesas or undulation of the surface. In the first case, usually the misfit dislocation forms a half loop with two segments of threading dislocations, as schematically shown in Fig. 2.16.

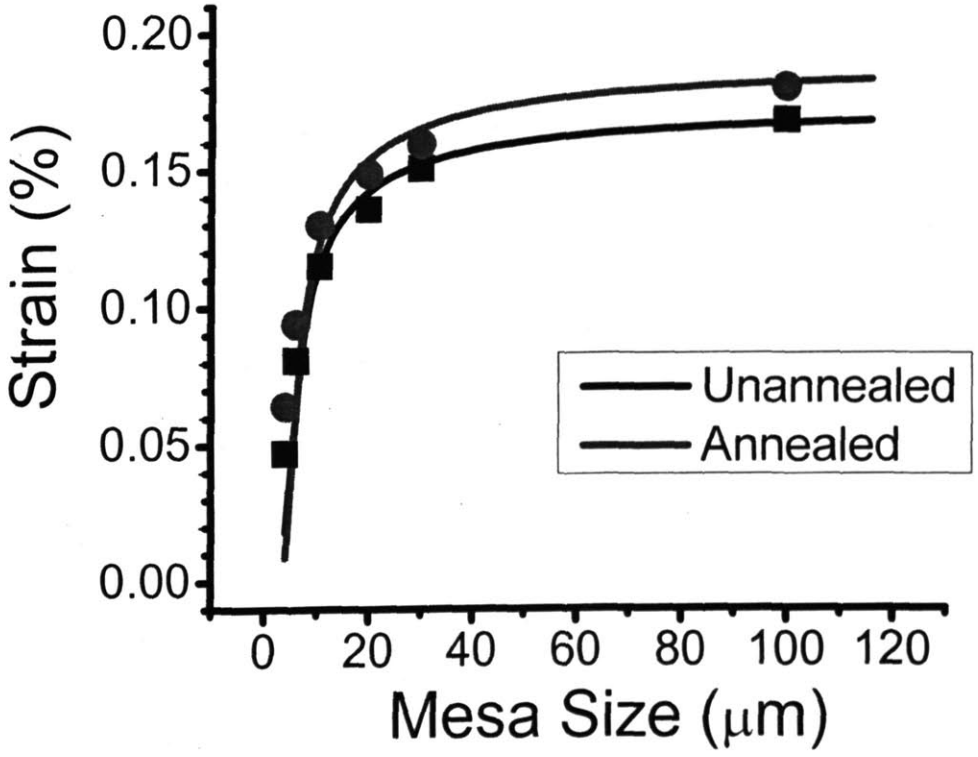

Fig. 2. 15 In-plane tensile strain $\varepsilon_{\parallel}$ as a function of square mesa size for as-grown and post-annealed samples. The samples were grown at 700 °C and post-annealed at 900 °C for 1h. The points in the figure are experimental data, while the lines are fitting curves to the theoretical model by Tersoff et al [70,71].

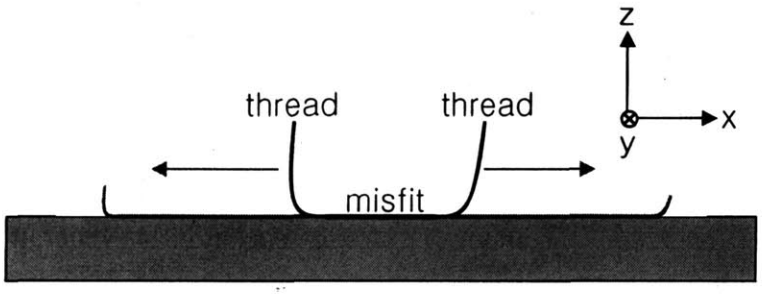

Fig. 2.16 Schematic drawing showing the generation/extension of a misfit dislocation that accompanies the gliding of two segments of threading dislocations.

The generation/extension of misfit dislocations accompanies the gliding of the two segments of threading dislocations toward the edges of the mesa. So some threading dislocations would glide to the edge and disappear, resulting in less threading dislocation density. However, etching pit study shows that the average threading dislocation density of the Ge mesa remains almost unchanged when the mesa size decreases from 100 μm to 10 μm, while significant strain relaxation already occurs. Furthermore, we saw a similar relaxation behavior as the mesa size shrinks in the as-grown samples at 600° C, while the threading dislocation motion is almost frozen at this temperature for Ge [68]. An even more tell-tale evidence was found when we study the in-plane strain anisotropy in an elongated rectangular Ge stripes. We know that the misfit dislocations along the x direction actually relax the strain in the y direction, and vise versa (see Fig. 2.16). Therefore, in an elongated rectangular Ge stripe the strain in the longitudinal direction should be easier to relax than the transverse direction, since the misfit dislocations can extend throughout the transverse direction much more easily than longitudinal direction. Yet the reality is the opposite from our experimental results. From a 2.5×100 μm Ge stripe we measured a tensile strain of 0.175% in the longitudinal direction while in the transverse direction it is only 0.024%. The result is exactly contrary to what we expect if

misfit dislocation generation/extension is the main reason for strain relaxation. Therefore, the strain relaxation in our case is unlikely to be related to misfit dislocation generation/extension at the Ge/Si interface.

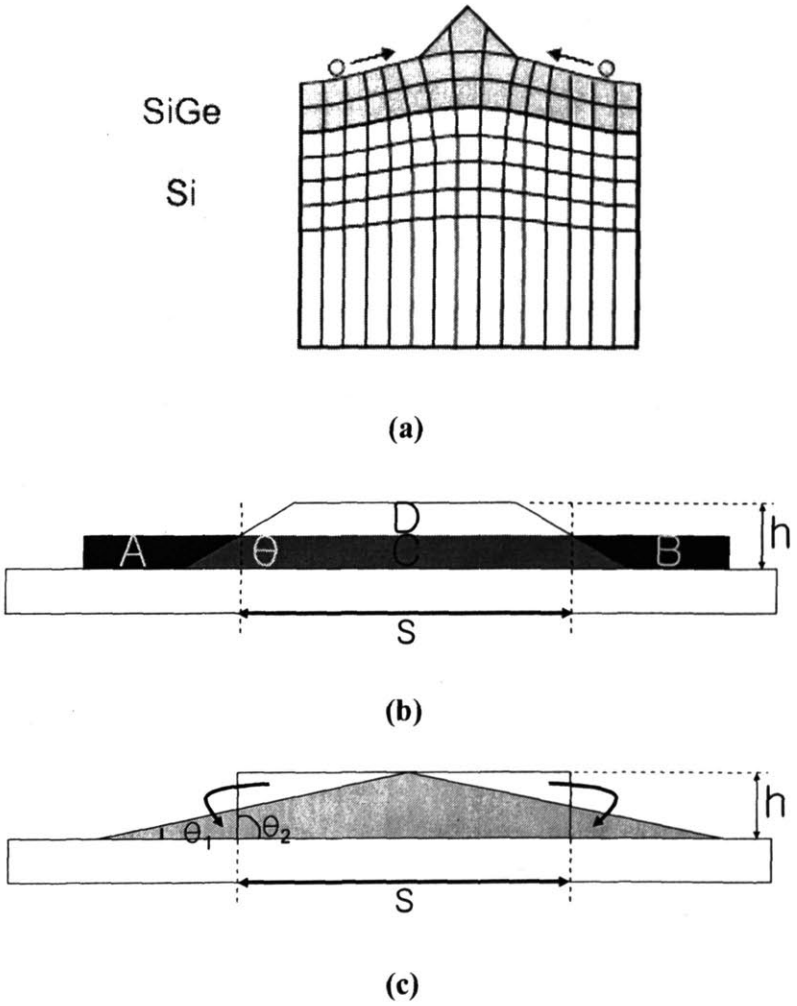

Fig. 2.17 Schematic drawing showing the elastic relaxation of SiGe induced by faceting or undulated surfaces. (a) forming undulation on the surface is equivalent to moving atoms away from the interface. (b) forming a facet is also equivalent to moving atoms away from the interface. (c) at the same width and height, reducing the facet angle is equivalent to moving atoms to the interface (from the white to the green triangle)

Faceting at the edges of the mesas or surface undulation can also induce elastic relaxation of the strain, as shown schematically in Fig. 2.17 [69]. The stress in a thin film is due to the lattice or thermal mismatch between the film and the substrate, so the stress

is maximized at the interface. Forming undulated surfaces is equivalent to moving atoms away from the interface (Fig. 2.17 (a)), thereby partially releasing the constraint of the interface and relaxing the strain. Fig. 2.17 (b) compares the case of a piece of blanket film with a faceted island of the same volume. It is equivalent to moving the atoms from regions A and B to region D. Since region D is further from the interface than regions A and B, the total strain energy is decreased due to faceting. The strain energy decrease due to elastic relaxation by faceting has been studied theoretically in literature to understand the formation of Ge islands on Si [70,71]. For a piece of mesa with a length of t, an average width of s (average over the top and bottom width), a thickness of h, and a facet that makes an angle of θ with the surface of the substrate (Fig. 2. 17(b)) , the amount of decrease in strain energy per unit volume in the case of $h, h/\tan\theta << s$, t is approximated by

$$E_r = 2c\left[\left(\frac{h}{s}\right)\ln\left(\frac{s}{h}e^{3/2}\tan\theta\right)+\left(\frac{h}{t}\right)\ln\left(\frac{t}{h}e^{3/2}\tan\theta\right)\right]. \qquad (2.18)$$

Here $c = \sigma_b^2(1-\nu_{Si})/2\pi G_{Si}$, where σ_b is the biaxial stress of the uniform blanket Ge film (i.e., without any faceting), while ν_{Si} =0.278 and G_{Si}=51GPa are the passion ratio and shear modulus of Si (100) substrate [27]. The term c is proportional to the strain energy without faceting. Eq. 2.18 shows that the larger the strain energy without faceting, the more the energy decrease after the strain is relaxed via faceting, which is reasonable intuitively. The in-plain tensile strain ε_0 in the blanket film deposited on the backside of the same wafers was determined to be 0.176±0.005% for unannealed samples and 0.192±0.004%. Therefore, $\sigma_b = Y_{100}\varepsilon_0$=0.247 GPa for unannealed samples and 0.270 GPa for annealed samples. The terms in the square brackets of Eq. 2.18 gives the geometrical

factor of strain energy reduction when a faceted structure is formed. The first term gives the strain relaxation in the transverse (width) direction, while the second one gives the strain relaxation in the longitudinal (length) direction. When s=t (square mesas), the strain relaxation in the longitudinal and transverse directions are the same. When s<<t (elongated rectangular mesa) the relaxation mainly happen in the transverse direction instead of the longitudinal direction.

One can imagine intuitively that the best way to relax the strain for a given volume of atoms is to put the atoms right on top of each other and form an "atomic wire" perpendicular to the substrate, since the contact area to the substrate is minimized in this case. This corresponds to $h/s \to \infty$, $h/t \to \infty$ and a facet angle of $\theta = 90^\circ$. As *h/s* or *h/t* decreases, the amount of strain relaxation decreases because a less proportion of the atoms are positioned away from the interface. This fact is mathematically embodied in Eq. 2.18 under the assumption of $h, h/\tan\theta << s$, t. The equation also indicates when *h, s,* and t are fixed, decreasing θ would result in less strain relaxation. This is because more atoms are positioned near the interface as θ decreases, as shown in Fig. 2.17 (c). In this figure, decreasing the facet angle from θ_2 to θ_1 is equivalent to moving the atoms in the white triangles to the green triangles. Since these atoms are closer to the interface, the strain relaxation is decreased. Therefore, it seems that a facet with larger θ would relax more strain energy and is more preferred. However, usually a large angle facet also increases the surface energy of the structure. Therefore, due to the balance of surface energy and strain energy we almost never see a facet with $\theta = 90^\circ$.

If the elastic energy of the system without faceting is E_s, then the total strain energy decreases to $E_s - E_r$ with the aid of faceting, as we defined earlier. It should also

be noted that when $E_s - E_r < 0$ Eq. 2.18 loses its physical meaning because strain energy can never be less than 0. In that case, we can just say the system should be fully relaxed due to faceting and the total strain energy is 0, instead of saying that the strain energy becomes negative. This is a limitation of Eq. 2.18 due to its approximation in the derivation of strain energy decrease related to faceting. It could become pronounced when the assumption $h, h/\tan\theta << s$, t is not satisfied.

In our case, the cross-sectional TEM picture in Fig. 2.12 shows that the edge of the mesa is consisted of (311), (111) and (113) facets. As a first order approximation, we can divide the mesa into three parts: one with (311) facet, one with (111) facet, and one with (113) facet, as shown in Fig. 2.12. The total strain energy reduction of the mesa structure due to faceting can be regarded as the sum of strain energy reduction of these three parts. Therefore, in this case

$$E_r = 2c\sum_{i=1}^{3} h_i \left[s^{-1} \ln\left(\frac{se^{3/2}}{h_i \cot\theta_i} \right) + t^{-1} \left(\frac{te^{3/2}}{h_i \cot\theta_i} \right) \right]. \qquad (2.19)$$

From Fig. 2.12, we get $h_1 = 659$ nm, $h_2 = 199$ nm, $h_3 = 205$ nm, $\theta_1 = 25.2^\circ$, $\theta_2 = 54.7^\circ$ and $\theta_3 = 72.5^\circ$. The maximum step height is 659nm for the (311) facet in Fig. 2.12, which is still much smaller than the lateral dimensions ($s = t > 2.5$ μm in our samples). Therefore, the approximation in Eq. 2.18 is applicable. The round corners at the joints of facets are neglected in this model.

Let ε_0 and ε_f be the in-plane strain in the blanket Ge film and faceted Ge mesa, respectively. Then the amount of decrease in elastic energy per unit volume induced by faceting should be:

$$E_r = Y_{100}(\varepsilon_0^2 - \varepsilon_f^2). \tag{2.20}$$

Comparing Eq. 2.19 with Eq. 2.20, we obtain

$$\varepsilon_f = \sqrt{\varepsilon_0^2 - \frac{2c}{Y_{100}} \sum_{i=1}^{3} h_i \left[s^{-1} \ln\left(\frac{se^{3/2}}{h_i \cot\theta_i} \right) + t^{-1} \left(\frac{te^{3/2}}{h_i \cot\theta_i} \right) \right]} \tag{2.21}$$

For square mesas s=t, and the calculated strain vs. mesa size is shown by the lines in Fig. 2.15. The result agrees reasonable well with the experimental results both for unannealed and annealed samples. Therefore, it is concluded that the strain relaxation of the selectively grown Ge mesas is mainly due to the faceting instead of misfit dislocation generation at the interface.

An interesting case is that when the mesa is an elongated rectangle stripe, i.e., t>>s, the model predicts that the strain relaxation in the longitudinal direction would be much less than that in the transverse direction. We have verified this prediction experimentally by measuring the strain in 100×2.5 μm Ge mesas. The longitudinal direction of the trench is along [011] direction, while the transverse direction is $[01\bar{1}]$. Therefore, by analyzing the (422) scans of the sample in two orthogonal directions, i.e. [011] and $[01\bar{1}]$, we are able to determine the strain relaxation anisotropy in the elongated rectangular mesa. The results show that the strain in the longitudinal direction (100 μm long) is 0.175%, similar to the strain in 100×100 μm mesas; while the strain in the transverse direction is only 0.024% (almost relaxed). These results not only verify the validity of the theoretical model of the facet-induced strain relaxation, but are also instructive for the design of waveguide-coupled GeSi modulator or detector devices. These devices usually have a small cross-section ($<1 \times 1$ μm^2) to keep single optical mode,

while the length is much larger than the cross-sectional dimensions (~ tens of μm) to achieve high enough absorption or modulation depth. The strain in these structures is mainly along the longitudinal direction if facets are formed during the Ge growth. One has to take this factor into account when engineering the band gap of GeSi material, since its effect on the band gap is different from biaxial stress case in blanket films. We will come back to this issue in Chapter 4 when we discuss the GeSi electro-absorption modulator design.

Chapter 3. Tensile Strained Ge Photodetectors on Si

In this chapter, we present the fabrication and performance of tensile strained Ge photodetectors on Si. We first demonstrate the enhancement of the responsivity of Ge photodetectors in the C (1528-1560 nm) and L (1561-1620 nm) bands with 0.25% tensile strain introduced by backside silicidation. We then present a selectively grown Ge photodetector on Si with a bandwidth of 8.5 GHz and a broad detection spectrum from 650 to 1605nm. These high performance devices are fabricated with technologies that can be integrated into a standard Si CMOS process, and are applicable to Si-based electronic-photonic integrated circuits.

3.1 Strain-engineered Ge/Si Photodetectors with Enhanced Responsivity [72]

As we mentioned in Chapter 1, the wavelength range used in the dense wavelength division multiplexing (DWDM) technology is expanding from C band (1528-1560 nm) to also include L-band (1561-1620 nm), requiring photodetectors that can cover both C and L bands. Tensile strained Ge epitaxial films on Si presented in Chapter 2 are promising candidates for achieving this goal with Si-compatible technology. By introducing 0.25 % tensile strain in epitaxial Ge films on Si with a backside silicidation process, the direct band gap of Ge can be decreased from 0.801 eV (corresponding to 1550 nm) to 0.764 eV (corresponding to 1623 nm), which is promising for applications in C+L band telecommunications. Therefore, tensile strained Ge/Si p-i-n photodetectors are fabricated to verify the enhancement of responsivity in L-band due to the direct band gap shrinkage.

3.1.1 Device Fabrication Process

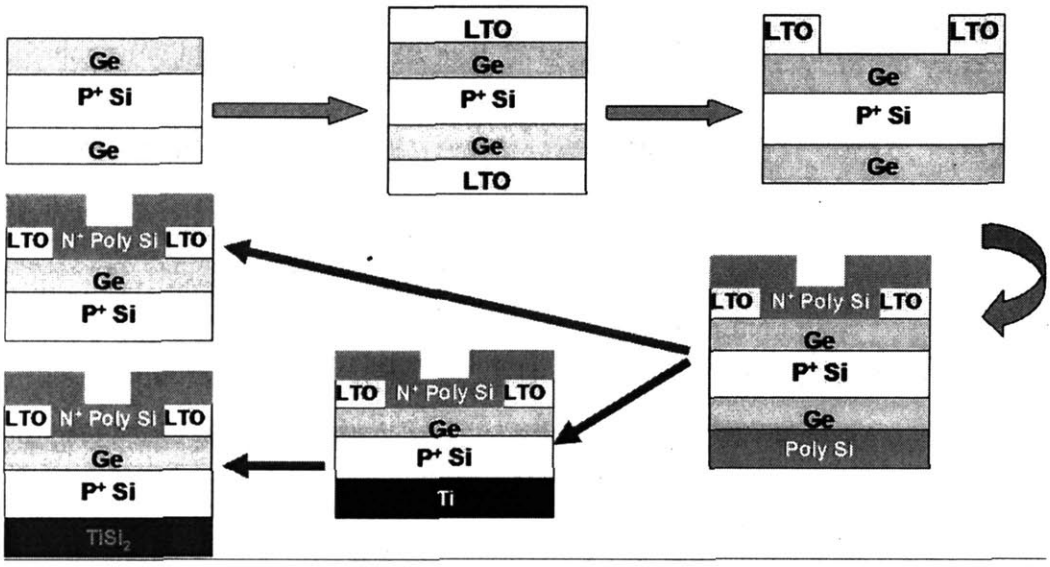

Fig. 3. 1 Process flow of fabricating tensile strained Ge p-i-n diodes on Si with blanket Ge films. The thickness of the films and substrates are not drawn to scale for clarity of labeling.

Fig. 3.1 shows the process flow of the device. Ge epitaxial films were deposited on 4-inch p^+ Si(100) substrates with a resistivity of <0.002 Ω·cm (boron doping ~10^{19}/cm^3) by UHVCVD. The thickness of the film was determined to be 2.35 μm by Ge element depth profile analysis of secondary ion mass spectrometry (SIMS). The root mean square roughness of the film was determined to be ~0.7 nm by atomic force microscopy (AFM). A one-hour annealing at 900 °C was performed to reduce the threading dislocation density from 8×10^8 /cm^2 to 1.7×10^7 /cm^2. Then a low temperature oxide (LTO) layer of 300 nm was deposited on top of the Ge film, and diode areas were defined by etching windows ranging from 10μm to 1cm in diameter through the LTO layer. A 200 nm poly Si layer was then deposited and implanted with phosphorous, followed by an activation annealing at 650 °C for 30 min. The peak concentration of phosphorous in the poly Si layer was in the order of 10^{20} /cm^3. The poly-Si layer was

then patterned to define the *n* side of the *p-i-n* diode, and the p^+ Si substrate was used as the *p* side. The poly Si and Ge layers on the backside were removed by reactive ion etching (RIE). Finally, a 1.5 μm Ti layer was deposited on the backside of the wafer, followed by a rapid thermal annealing (RTA) at 800 °C for 5 min to form C54-$TiSi_2$. This C54-$TiSi_2$ layer on the backside enhances the tensile strain in the front side Ge film, and also serves as a backside electrical contact. All the materials and processing techniques used in this device are CMOS-compatible. The tensile strain in the front side Ge layer was determined to be 0.25 % by XRD. In the later text, these devices will also be referred to as 0.25 % tensile strained samples. A set of samples without backside silicidation were also fabricated as a reference, in which the tensile strain in the Ge films was 0.20 %. They will also be referred to as the 0.20 % tensile strained samples in the later text.

3.1.2. *I-V* Characteristics

The *I–V* characteristics of the device were measured with a HP4145A semiconductor parameter analyzer. The current was divided by the device area to obtain *J-V* curves, where *J* stands for the current density. Fig. 3.2 shows the J-V characteristics of Ge p-i-n photodiodes on Si with and without backside silicidation. The J-V characteristic of a diode is given by

$$J = J_0(\exp(qV/\eta kT) - 1), \qquad (3.1)$$

where J_0 is the dark current density while η is the non-ideality factor. η=1 indicates ideal diode behavior. Generation/recombination in the depletion region leads to η=2. In

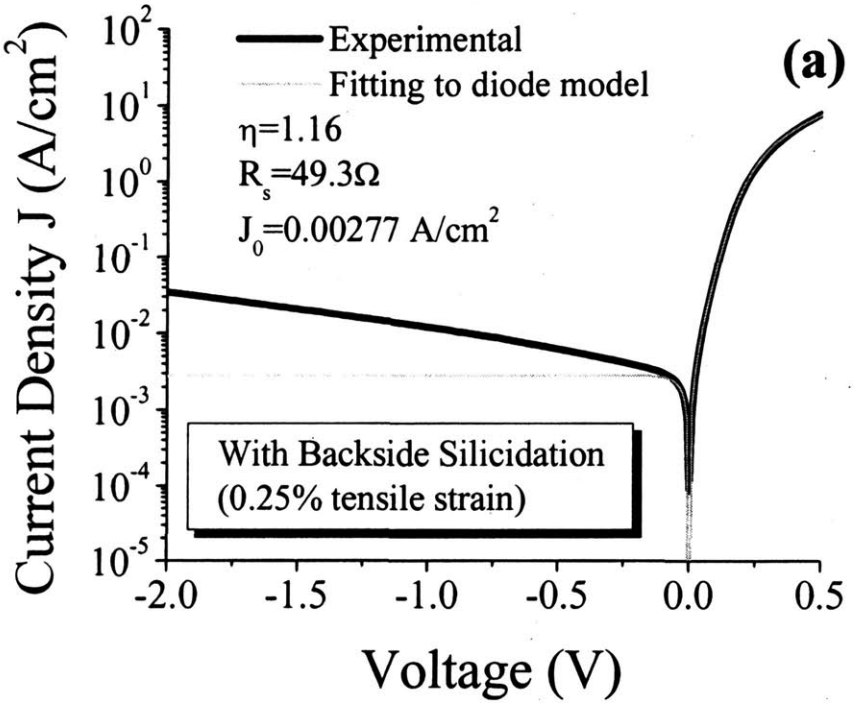

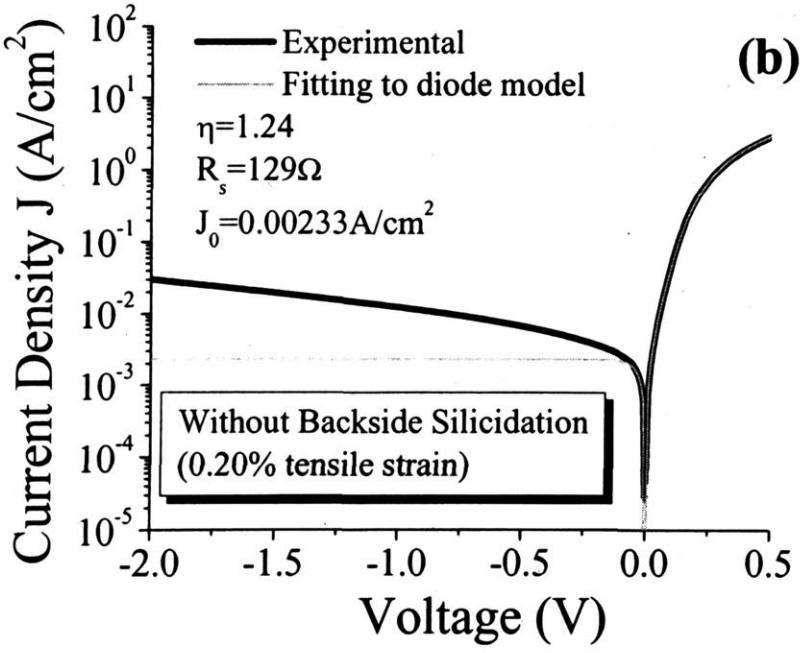

Fig. 3. 2 J-V characteristics of Ge p-i-n diodes with and without backside silicidation

reality, the non-ideality factor of a diode is usually between 1 and 2 at low forward bias. At high forward bias, the series resistance effect has to be taken into account, so the *J-V* curve starts to deviate from the ideal exponential growth. Taking into account the series resistance, the *J-V* relation should be given by

$$J = J_0\left[\exp\left(\frac{q(V - JAR_s)}{\eta kT}\right) - 1\right], \tag{3. 2}$$

where A is the junction area and R_s is the series resistance. Eq. (3. 2) is an implicit equation of J. By fitting the experimental *J-V* curves with Eq. (3. 2), we can derive the saturation dark current J_0, the non-ideality factor η and the series resistance R_s. The derived values are shown in the inset of Fig. 3.2. The backside silicidation has little effect on J_0, η and the dark current at reverse bias, but decreases the series resistance significantly from $129\,\Omega$ to $49\,\Omega$. Therefore, the backside silicidation increases the tensile strain and improves the contact resistance without deteriorating the device performance in terms of dark current and ideality factor.

An interesting phenomenon in Fig. 3.2 is that although we can fit the forward bias part of the experimental *J-V* curves very well with equation (3.2), (correlation factor>0.999), the dark current at reverse bias measured experimentally is much larger than J_0. The saturation dark current density derived from the fitting is $\sim 2\times 10^{-3}\,A/cm^2$, yet the experimentally measured values at 2 V reverse bias is an order of magnitude higher. Also, the dark current increases with the reverse bias in the experimental data, in contrast to the saturation behavior of dark current given in Eq. (3.2). The non-ideality factor of the diodes is around 1.2, indicating that although there is some generation/recombination in the depletion region, yet it is not dominant. Moreover, even

the generation/recombination current should saturate as the carriers reach saturation velocity at reverse bias. Yet we did not observe any saturation in dark current up to 5 V reverse bias, corresponding to >30 kV/cm electric field and well enough to accelerate the carriers to saturation velocity. Therefore, such a high, voltage-dependent dark current cannot be explained by generation-recombination current in the depletion region alone.

It has been known that threading dislocations act as conducting paths in addition to lifetime killers in semiconductor materials [73,74,75,76]. The dangling bonds along the dislocations overlap with each other, thus forming a conduction path for the carriers trapped by the dislocations. DC I-V measurements along the dislocations in Ge thin plates and electron beam induced current (EBIC) measurements have been used to study the conductivity of dislocations in Ge, and a one-dimensional, quasi-metallic conduction along 60° dislocations in Ge was well established [73,77]. Therefore, the dislocation conductivity could contribute significantly to the dark current. To explain the discrepancy in the *J-V* data fitting between the forward and reverse bias, here an equivalent circuit model is presented in Fig. 3.3 based on the assumption that the conductivity of the dislocations also plays a key role in the *J-V* curves. The threading dislocations can be modeled as a resistor in parallel to the diode. At forward bias the resistance of the dislocations R_{dis} is much higher than the diode itself, so the current mainly flows through the diode, as indicated by the red arrows on the left half of Fig. 3.3. As a result, we can hardly see any effect related to the conductivity of dislocations at forward bias. At reverse bias, however, the dislocation resistance R_{dis} is much smaller than the junction resistance of the diode, so the reverse current mainly flows through the threading dislocations, as indicated by the red arrows on the right half of Fig. 3.3. Therefore, we

observe a normal diode behavior at forward bias as if almost no dislocations exist, while at reverse bias we observe much higher dark current than expected due to the conduction path through the threading dislocations.

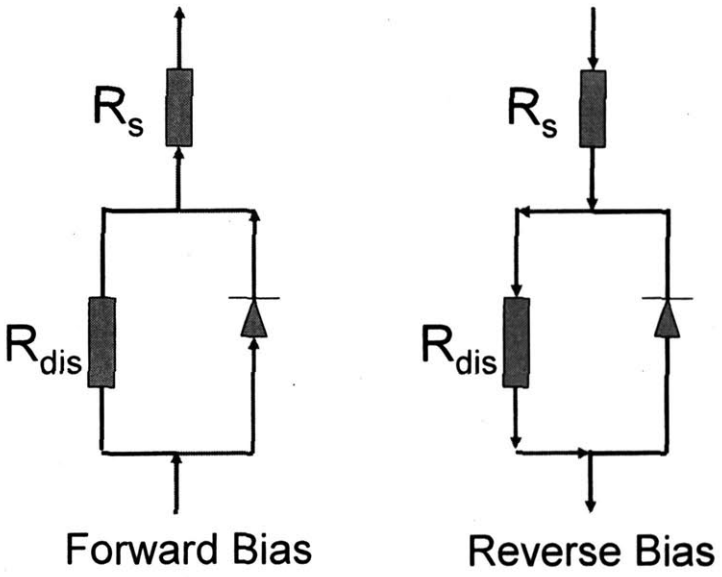

Fig. 3. 3. Equivalent circuits of Ge p-i-n diodes on Si with threading dislocations in the Ge material.

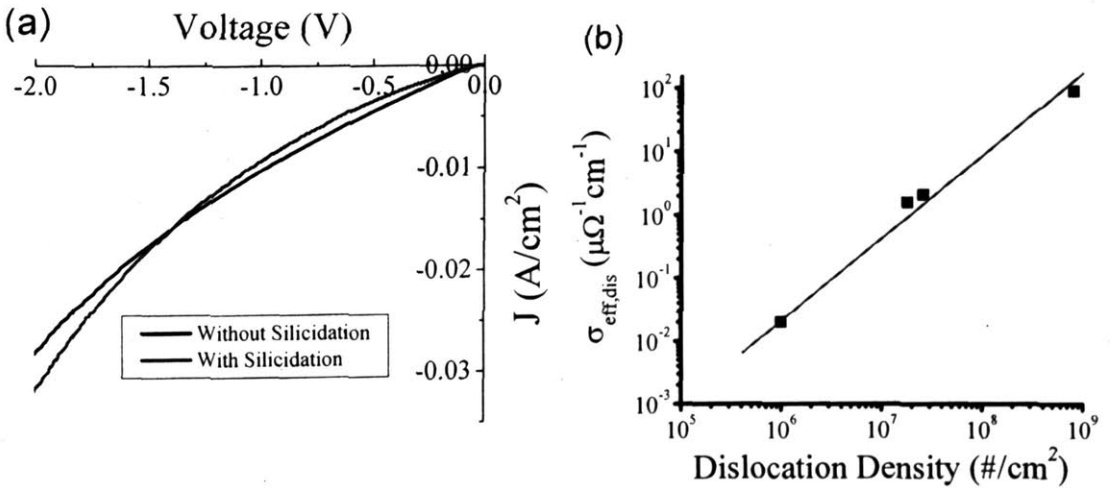

Fig. 3. 4 (a) J-V characteristics of the threading dislocations derived from the J-V data of Ge/Si p-i-n diodes, and (b) effective conductivity of reverse biased Ge diode as a function of dislocation density.

Subtracting the fitted I-V data from the experimental data at reverse bias, one obtains the I-V curve of the dislocations, as shown in Fig. 3.4 (a). Indeed, the resistance

of the dislocation is much larger than that of the diode at forward bias. For example, at 0.2V bias the current density flowing through the dislocations is only ~10^{-3}A/cm^2, while through the forward biased junction the current density reaches ~1A/cm^2. This is consistent with our model that the dislocation resistance is much higher than the forward biased junction. However, at reverse bias R_{dis} is much lower than the junction resistance, so the dark current we see is mainly due to the conductive paths along these threading dislocations. The effective conductivity of the reverse biased Ge diode is plotted as a function of threading dislocation density in Fig. 3.4 (b), combining the data of this work with references [9] and [68]. The effective conductivity increases linearly with the threading dislocation density, providing a strong evidence that the conductivity is related to dislocations.

To sum up, our model on the *J-V* characteristics of epitaxial Ge/Si diodes not only considers the generation/recombination of threading dislocations, but also the intrinsic conductivity of threading dislocation. The model can effectively explain the experimental result. However, more elaborate study is needed to understand the mechanism of the conductivity of threading dislocations in epitaxial Ge films on Si.

3.1.3. Responsivity Measurement

The responsivity was measured with a monochromatic light source in the wavelength range of 1300-1650 nm on Ge photodiodes of 300 μm in diameter. The light was directed at a normal incidence from the top of the device. No antireflection coating was deposited on the top surfaces of the devices. The incident light intensity was calibrated with a commercial Ge photodetector and an InGaAs photodetector. In this

wavelength range the difference between the two calibration detectors is within 7%. An average intensity of the two detectors was used as the incident intensity.

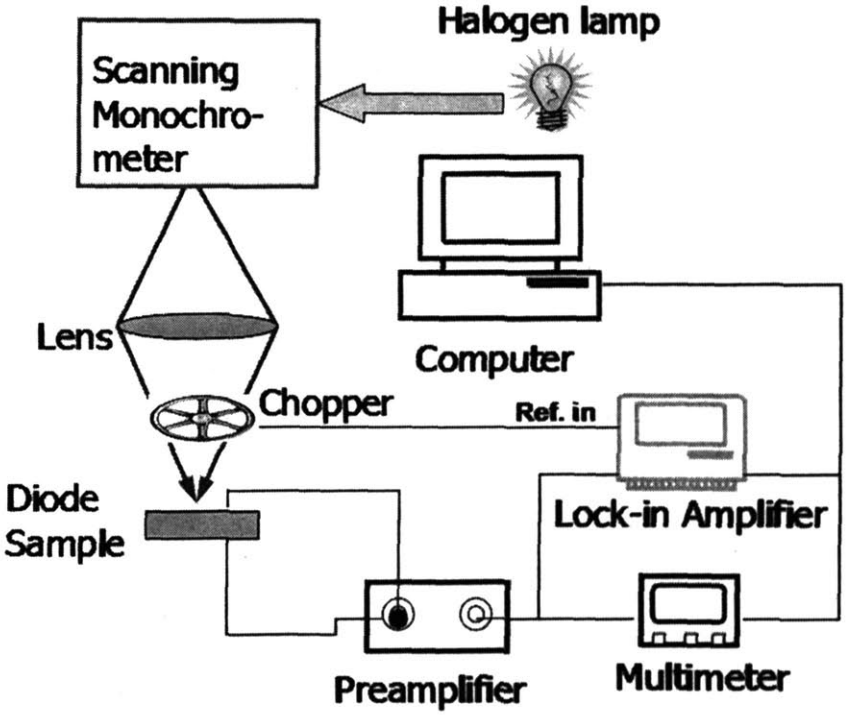

Fig. 3. 5 Schematic diagram of responsivity measurement set up

As the incident light intensity from the monochrometer shone on the diode is low (~10 nW on 300 μm diameter diode), the photocurrent is small compared to the dark current except for the 0V bias case. To measure the photocurrent accurately, a lock-in method is applied. The basic setup is shown in Fig. 3.5. The incident light from the monochrometer is chopped at a frequency of 401Hz. This chopping frequency is used as a reference input to a lock-in amplifier. A preamplifier supplies a DC voltage to the diode while reads out the current that passes through the diode at the same time. It sends the current signal to a multimeter and the lock-in amplifier. The multimeter reads the DC part of the current, i.e., the dark current of the diode. The lock-in amplifier is synchronized to

the chopper and reads the AC part of the current, i.e., the photocurrent. This way the photocurrent can be measured with high signal to noise ratio.

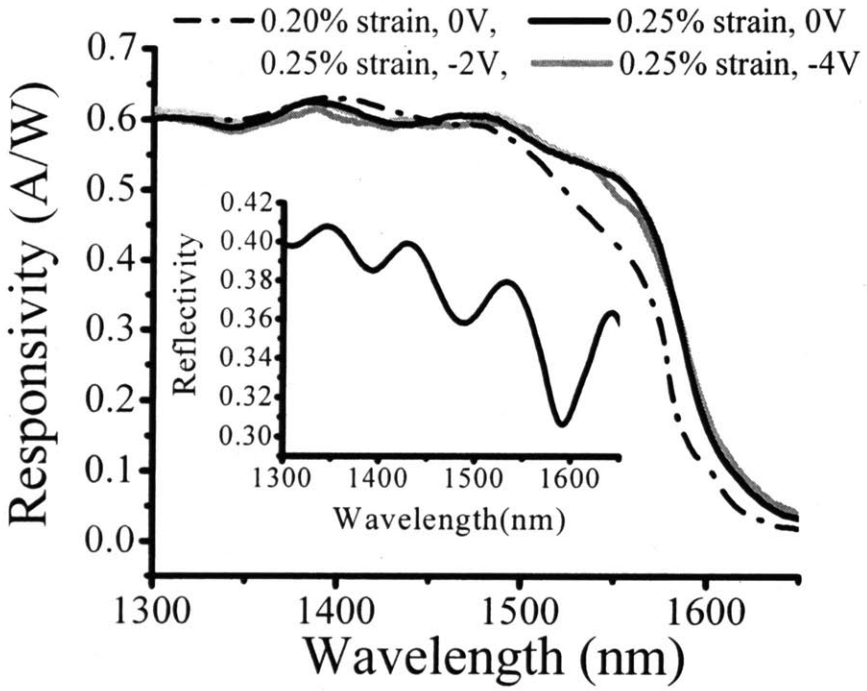

Fig. 3. 6 Responsivity of Ge/Si p-i-n diodes measured at different bias.

The responsivity spectra of the Ge photodetectors on Si with and without backside silicidation under different reverse bias are shown in Fig. 3.6. The backside silicidation increases the tensile strain in the Ge layer from 0.20 to 0.25 %, and further reduces the direct band gap from 0.773 eV (1605 nm) to 0.7640 eV (1623 nm). As a result, the responsivity at 1620 nm under 0 V bias increases dramatically from 48 mA/W to 100mA/W after backside silicidation. The responsivity at 1550 nm also increases from 422 mA/W to 520 mA/W. Thus, the strain enhancement induced by backside silicidation increases the responsivity in the C band and extends the detection range of Ge/Si photodetectors to cover the whole L band. The responsivity at 1310 nm (another telecommunication wavelength) is 600 mA/W. The reflectivity spectrum at the surface of

the devices is shown in the inset of Fig. 3.6, as measured from a 1 cm diameter photodiode on the same wafer. From these reflectivity data, we calculated that with antireflection coating the responsivity of the 0.25 % tensile strained device can be further improved to 150, 810, and 980 mA/W at 1620, 1550, and 1310 nm, respectively, effectively covering the whole wavelength range used in optical communications. The responsivity of the device at 1550 and 1310 nm is comparable to commercially available InGaAs photodetectors [78]. Another interesting feature shown in Fig. 3.6 is that nearly full responsivity was already achieved at 0 V bias in the whole spectrum range of 1300-1650 nm. The doping profile of the device measured by SIMS is shown in Fig. 3.7. The background doping level in the intrinsic Ge layer is near the detection limit of SIMS, i.e., $2\times10^{14}/cm^3$ for phosphorous and $3\times10^{13}/cm^3$ for boron. Due to the low doping background, the electric field in the intrinsic Ge layer is calculated to be ~2 kV/cm at 0V, as shown in Fig. 3.8. The drift velocity of electrons and holes in Ge at 2 kV/cm are 5.1×10^6 cm/sec [79] and 3.0×10^6 cm/sec [80], respectively. Therefore, the transit time of electrons and holes in the intrinsic Ge layer is as short as 45 and 77 ps, respectively. The carrier life time in the Ge material with 1.7×10^7 $/cm^2$ threading dislocation was determined to be ~1 ns [53], more than an order of magnitude longer than the transit time. So all the carriers generated by photons are collected before they recombine even at 0 V bias. The high collection efficiency explains why maximum responsivity can already be achieved at 0 V bias. This feature is very desirable to meet the requirement of a low driving voltage of $\leq$1.5 V in Si ultra large scale integrated circuits (ULSI) [1].

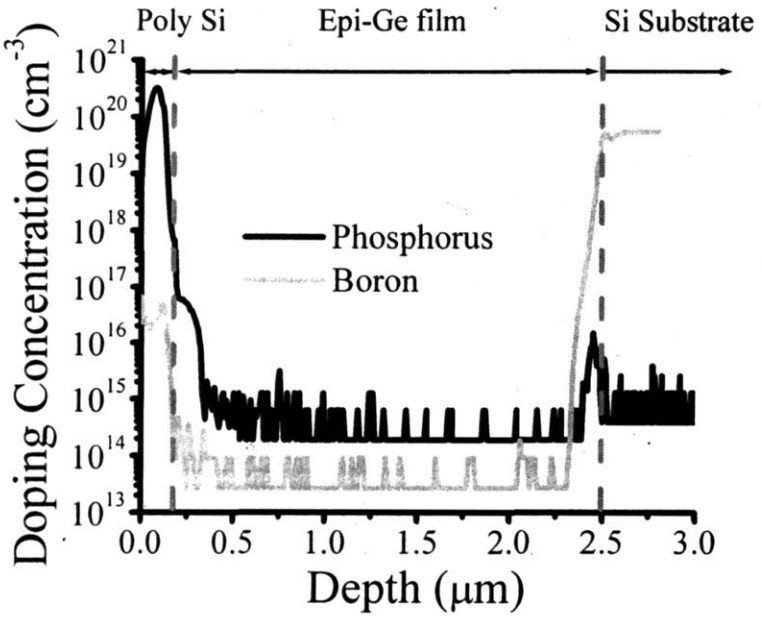

Fig. 3. 7 Secondary Ion Mass Spectroscopy (SIMS) depth profile of a 300μm diameter, 0.25% tensile strained Ge photodiode.

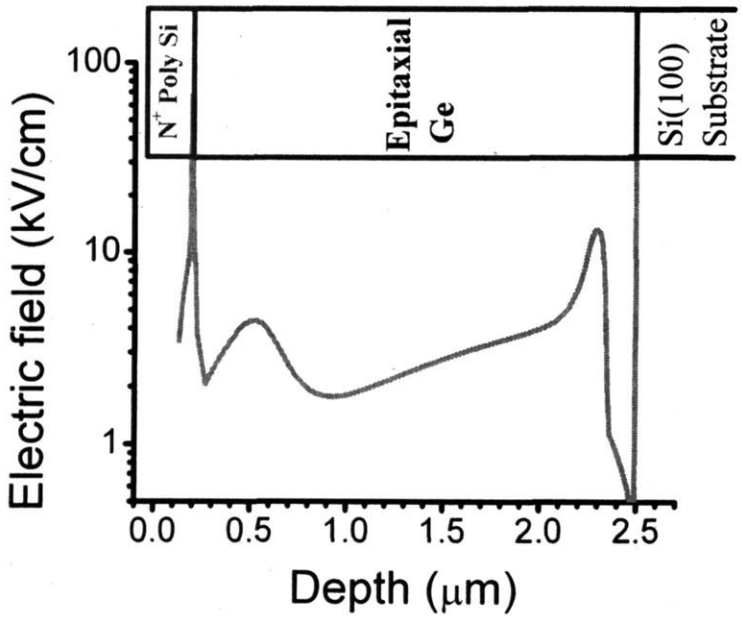

Fig. 3. 8 Electric field at 0V bias in Ge/Si p-i-n diodes calculated from the doping profile.

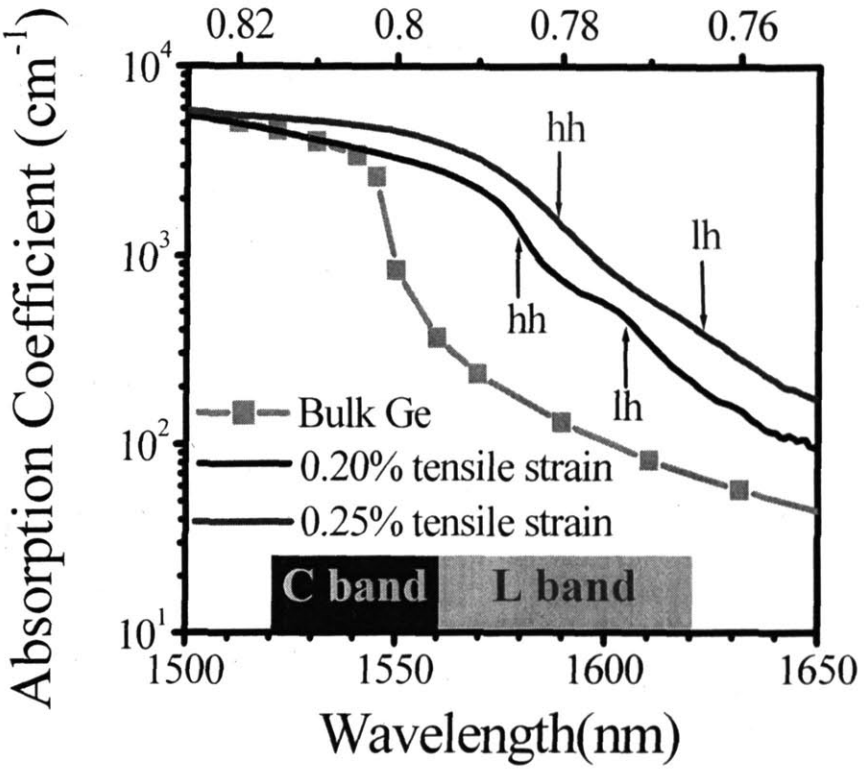

Fig. 3. 9 Absorption spectra of bulk Ge , 0.20% and 0.25% tensile strained Ge. The absorption coefficients in the L band have been enhanced by nearly an order of magnitude in 0.25% tensile strained Ge compared with bulk Ge. The direct transition energies from the top of the light and heavy hole bands to the bottom of conduction bands, calculated with the deformation potential values reported in Ref. 5, are indicated by "lh" and "hh" in the figure.

From the responsivity and reflectivity spectra in Fig. 3.6, the absorption spectra of the 0.20% and 0.25% tensile strained Ge can be derived. The absorption coefficient (α) at a certain wavelength is related to responsivity (R) and reflectivity (r) of the device by

$$\alpha = -\frac{1}{t_{Ge}} \ln\left[1 - \frac{1240}{\lambda(nm)} \bullet \frac{R(A/W)}{(1-r)}\right] \tag{3.3}$$

where t_{Ge}=2.35μm is the thickness of the Ge film, λ is the wavelength in terms of nm, and the reflectivity is shown in the inset of Fig. 3.6. The result is shown in Fig. 3.9 and compared with the absorption spectrum of bulk Ge reported in Ref. [81]. The direct transition energies from the top of the light and heavy hole bands to the bottom of

conduction bands were calculated with the deformation potential values reported in Chapter 2, indicated by "lh" and "hh" in the figure for the 0.20 and 0.25 % tensile strained samples. These calculated values correspond fairly well to the absorption edges of the experimental data. The absorption coefficient at 1620nm has been increased from 70/cm of bulk Ge to 265/cm for 0.20% tensile strained Ge and to 506/cm for 0.25 % tensile strain Ge, a significant improvement by nearly an order of magnitude. The absorption coefficient at 1550 nm has also been greatly enhanced from 840/cm of bulk Ge to 3300/cm for 0.20 % tensile strained Ge and to 4570/cm for 0.25 % tensile strained Ge. Such remarkable increase in absorption coefficients greatly improves the responsivity of the Ge photodiodes. Therefore, tensile strain has been demonstrated to significantly improve the absorption and responsivity of Ge photodiodes on Si.

3.2. Selectively Grown Ge/Si p-i-n photodiodes [82]

Selectively grown Ge photodiodes on Si are highly desirable for convenient integration with Si CMOS devices. In this section, we present the fabrication process, *J-V* characteristics, responsivity measurement and bandwidth measurement of a selectively grown Ge photodetector on Si.

3.2.1. Process Flow

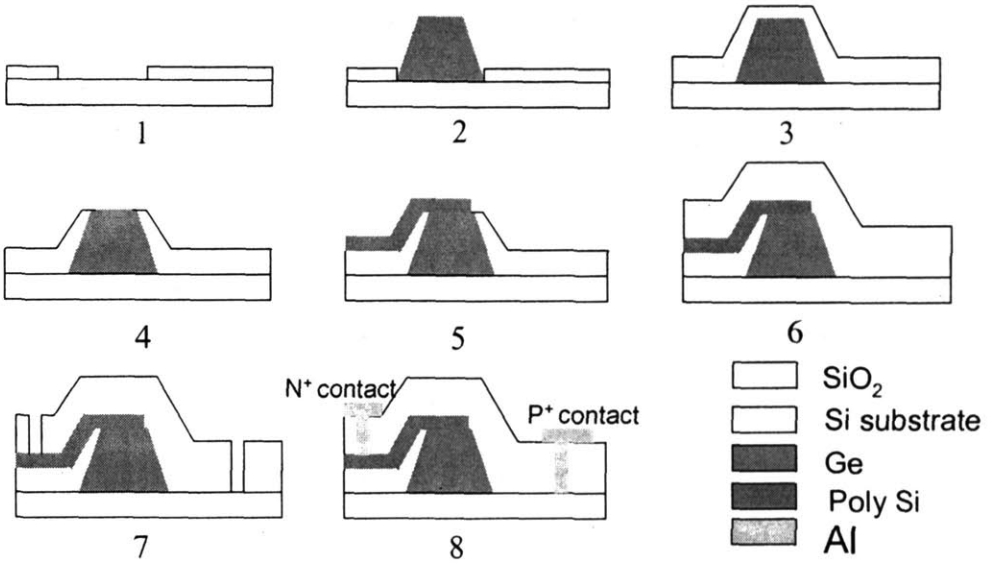

Fig. 3. 10 Process flow of selectively grown Ge/Si p-i-n photodiodes

Fig. 3.10 shows the process flow of fabricating selectively grown Ge/Si p-i-n photodiodes. A 200 nm thermal oxide was grown on top of the Si wafer, and windows are opened through the SiO_2 layer till the Si substrate is exposed (step 1). Smooth Ge epitaxial layers with a root mean square roughness of ~0.7 nm (determined by atomic force microscopy in a 10×10 μm^2 area) were selectively grown directly in these windows (step 2). A ~60 nm Ge buffer layer was grown at 335 °C followed by a high temperature growth at 700 °C to deposit 2.35 μm of Ge. The Ge layers were grown on boron doped p^+ Si wafers with a resistivity of 0.001-0.005 Ω cm. The Ge epitaxial film was then subjected to a 900 °C anneal to reduce the threading dislocation density from $8.0\times10^8/cm^2$ to $1.7\times10^7/cm^2$. Due to the thermal expansion mismatch between the Ge epitaxial layer and the Si substrate, 0.20% in-plane tensile strain was introduced into the Ge layer, reducing the direct bandgap of Ge from 0.801 to 0.773 eV and extending the effective photodetection range to 1605 nm. A low temperature oxide (LTO) is deposited on the

whole wafer (step 3), followed by lithography and etching to open a window on top of the Ge mesa (step 4). A poly Si film is deposited on top of the wafer, implanted with $5\times10^{15}/cm^2$ phosphorus at 100keV with 7 degrees' tilt, annealed at 650°C for 30 min to activate the dopant, and then subjected to lithography and etching such that an n^+ poly Si contact pad is defined on top of the intrinsic Ge layer (step 5). An 800 nm oxide layer was deposited by plasma enhanced chemical vapor deposition (PECVD) on top of the substrate (step 6), and contact holes are etched through the PECVD oxide to reach the n^+ poly Si and the p^+ substrate (step 7). Then an Al layer is deposited and etched to make metal pads that contact the n^+ poly Si and the p^+ Si substrate. The Al was sintered at 400°C in forming gas (N_2/H_2) for 20min to obtain ohmic contact with n^+ and p^+ Si. The n^+ poly Si layer forms the *n*-type side of the *p-i-n* diode, while the p^+ Si substrate naturally forms the *p*-type side of the device. No antireflection coating was deposited on the devices. The entire device was fabricated using materials and processing that can be implemented in a standard CMOS process flow.

A top-view micrograph of the device is shown in Fig. 3. 11. The electrode forms a ground-signal-ground (GSG) configuration to accommodate the requirement of high speed measurements. The center to center distance between Al pads is 100 μm. The two ground pads are connected together to make sure they have equal potential.

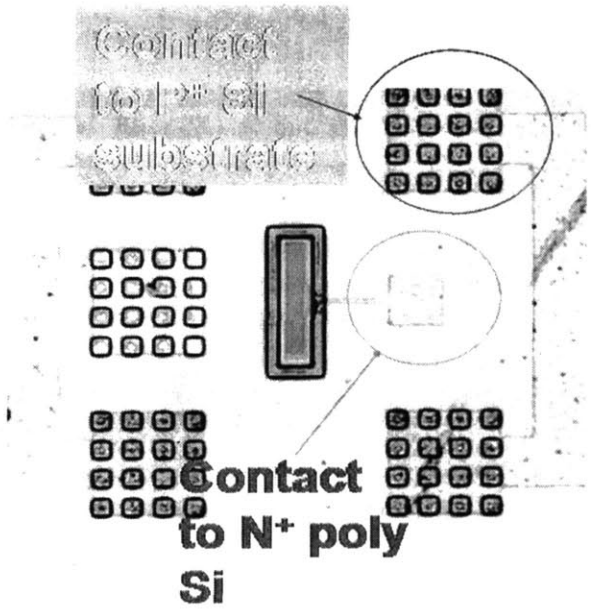

Fig. 3. 11 Top view of a selectively grown Ge p-i-n diode on Si

3.2.2 *I-V* characteristics

Fig. 3.12 shows the *J-V* characteristics of a 100μm-diameter diode before and after metallization. The one before metallization was processed up to step 5 in Fig. 3. 10, i.e., no PECVD oxide was deposited on top of the diode and no Al contact was used. The device was measured directly by top and bottom contacts of probes to n^+ poly Si and p^+ substrate, respectively. The result is shown in Fig. 3.12 (a). Compared to the blanket Ge diodes mentioned in Section 3.1, the dark current is an order of magnitude higher. The non-ideality factor increases from 1.2 to 1.8, indicating significant increase in generation/recombination current. As the dislocation density is similar to the blanket diode case, it is unlikely that such deterioration in diode performance is related to threading dislocations.

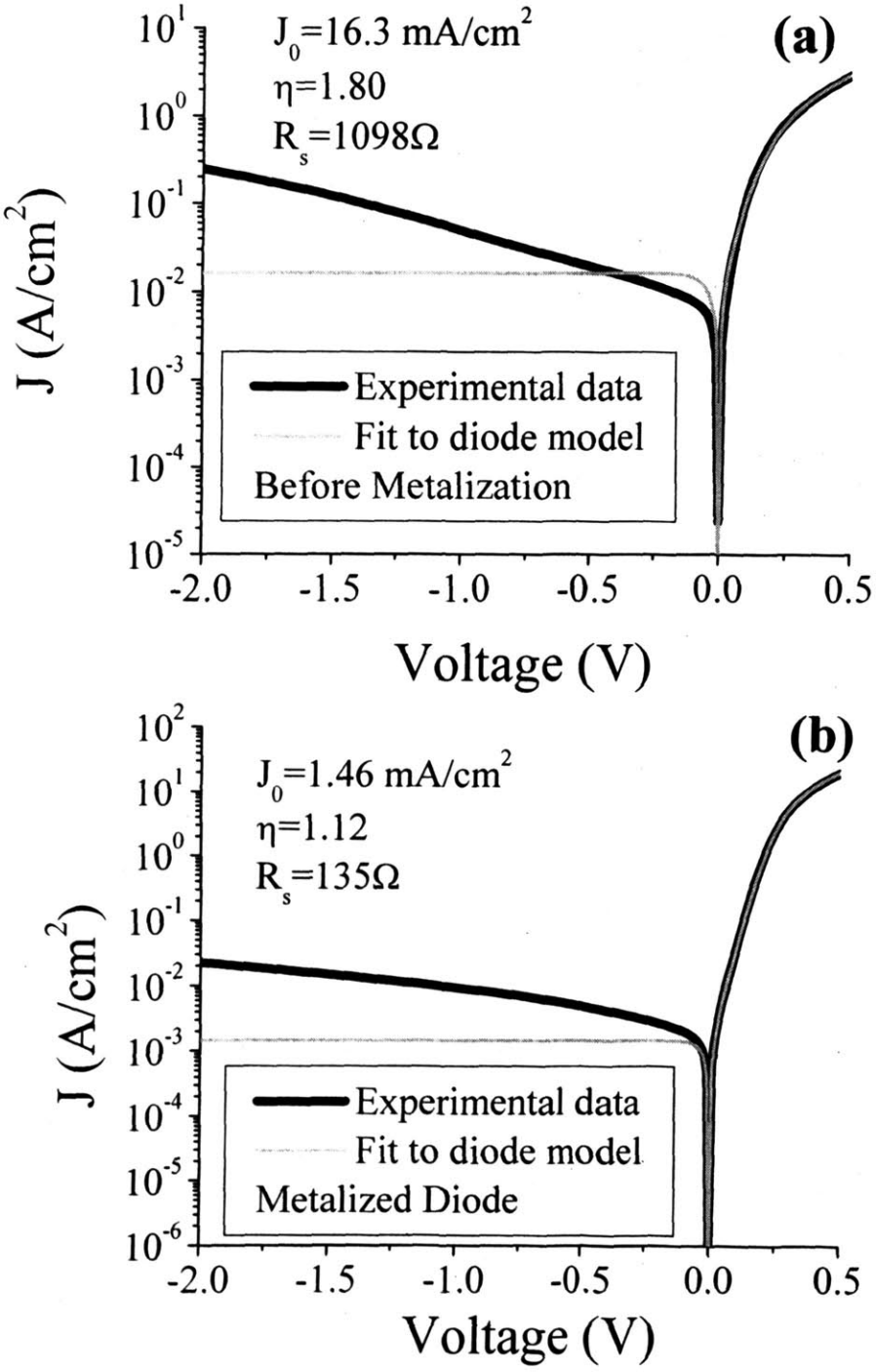

Fig. 3. 12 J-V characteristics of 100μm diameter selectively grown diodes before and after metallization.

Since the only major difference between the blanket and the selectively grown Ge is that the latter has a side wall at the edge of the mesa, it is very likely that the increase in dark current is due to the surface recombination at the sidewall of the Ge mesas. This notion is further supported by the *J-V* data after metallization, as shown in Fig. 3.12 (b). After steps 6-8 shown in Fig. 3.10, the dark current of the selectively grown diodes decreases dramatically by about an order of magnitude to the same level of blanket diodes. In fact, after metallization steps the dark current density is about 30% smaller than the blanket diodes. The non-ideality factor also decreases from 1.8 to 1.1, also a dramatic improvement compared to non-metallized diodes and even a little better than blanket diode cases (η=1.2). During these metallization steps the processing temperature was well below 500°C, while dislocation motion in Ge requires a temperature of >700°C. Therefore, it is impossible that the threading dislocation density be decreased in these processing steps. The Al deposition and sintering are also very unlikely to improve the Ge quality by any means. However, in the PECVD oxide deposition (step 6) atomic H is introduced due to the precursor gases used in the deposition. Since the deposition temperature is low (~150°C), the H atoms could be trapped into the device structure and help passivate the defects at the sidewall of the Ge mesas and threading dislocations. Therefore, a dramatic decrease in the dark current and improvement in the non-ideality factor is observed. As the *J-V* performance of metallized diodes is significantly better than the non-metallized ones while only slightly better than the blanket diodes, it seems the atomic H mainly helps to passivate the Ge mesa sidewall. This phenomenon suggests that adequate H passivation can be used to decrease the dark current in Ge diodes on Si.

3.2.3 Responsivity and Bandwidth Performance

The DC responsivity was measured with a monochromatic light source in the wavelength range of 650–1650 nm on Ge photodiodes 100 μm in diameter. The light was directed at normal incidence on the top surface of the device. The details of the responsivity measurement set up were already described in Section 3.1.

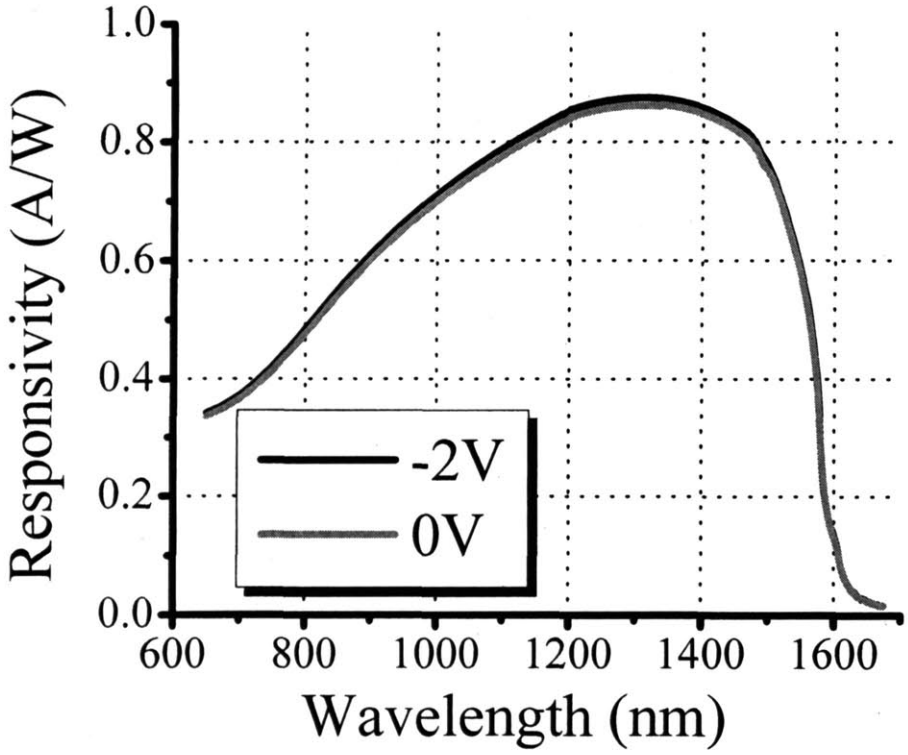

Fig. 3. 13 DC responsivity at 0 V and 2 V reverse bias in the wavelength range of 650–1650 nm without antireflection coating. With 0.20% tensile strain in the Ge layer, the effective detection limit of the device has been extended from 1550 to 1605 nm, covering the whole C band and a large part of the L band. The DC responsivity already saturates at 0 V bias, a very desirable feature for low voltage operation.

Fig. 3.13 shows the DC responsivity spectrum of the device at 0 V and 2 V reverse bias. Note that the effective detection range is extended from 1550 nm to 1605 nm compared with bulk Ge. This is due to the direct bandgap shrinkage from 0.801 to

0.773 eV induced by 0.20% tensile strain. Therefore, the device is able to effectively cover the entire C band and a large part of the L band in telecommunications. The responsivity of the device at 850, 980, 1310, 1550 and 1605 nm is 0.55, 0.68, 0.87, 0.56 and 0.11 A/W, respectively, without antireflection coating on the surface. The responsivity could be further improved with strain enhancement by backside silicidation and/or antireflection coating. The internal quantum efficiency in the wavelength range of 650–1340 nm was determined to be over 90%. The high responsivity over a broad detection spectrum makes it not only applicable for telecommunication wavelengths (1310, 1528–1605 nm), but for integrated optical interconnect wavelength (<1000 nm) as well. The responsivity at 0 V bias is more than 98% of that at 2 V reverse bias over the whole spectrum, indicating excellent carrier collection. As discussed in Section 3.1, this is due to the existence of ~2kV/cm electric field in the intrinsic Ge layer even at 0 V bias, so that the carriers can be collected well before they recombine at any defect center. The ability of the device to operate at such low reverse bias is compatible with the requirement of a low driving voltage of ≤1.5 V in Si ultra-large scale integrated circuits (ULSI) [1].

The temporal response set up is shown in Fig. 3.14. For high-speed characterization, a Tektronix 11801C digital oscilloscope with a SD-32 50 GHz sampling head was used to measure the temporal response of the photodetectors to a mode-locked Yb-fiber laser at 1040 nm [83]. The laser produces chirped pulses, which are compressible to 70 fs. For these measurements, the uncompressed pulses of ~1 ps duration were utilized. A 50 GHz ground-signal-ground (GSG) probe, a 50 GHz bias-T and 3.5 mm microwave cables were used in the measurement circuit. If the detector could

respond in no time and there is no RC delay in the circuitry, then we would see an electrical pulse that is exactly the same as the optical laser pulse. However, due to the response time of the detector and RC delay of the circuit, the pulse we measure on the oscilloscope will be broader than the input optical pulse. But analyzing the response pulse data, we can derive the response time and bandwidth of the photodetector.

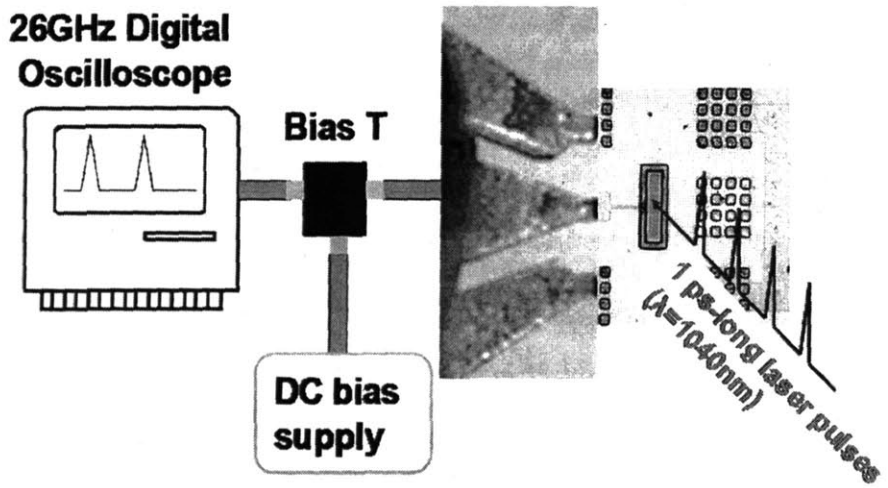

Fig. 3. 14 Schematic diagram of the temporal response setup for photodetector bandwidth measurement.

Fig. 3.15 (a) shows the temporal response of a 10×70 μm photodiode at a reverse bias of 1 V to the 1 ps-long pulses generated by the 1040 nm mode-locked fiber laser. Because the laser pulses are much shorter than the response time of the photodetector, the effect of laser pulse width on the measurement result is negligible. The resolution of the measurement is 0.2 ps. The shape of the temporal response of the photodetector is mostly Gaussian, with a small tail due to the carrier diffusion process. The full width at half maximum (FWHM) of the response pulse is 46 ps. To obtain the frequency response, a

Fourier transform of the pulse was performed without de-convolving the RC delay of the measurement circuit, and the result is shown in the inset of Fig. 3.15 (a).

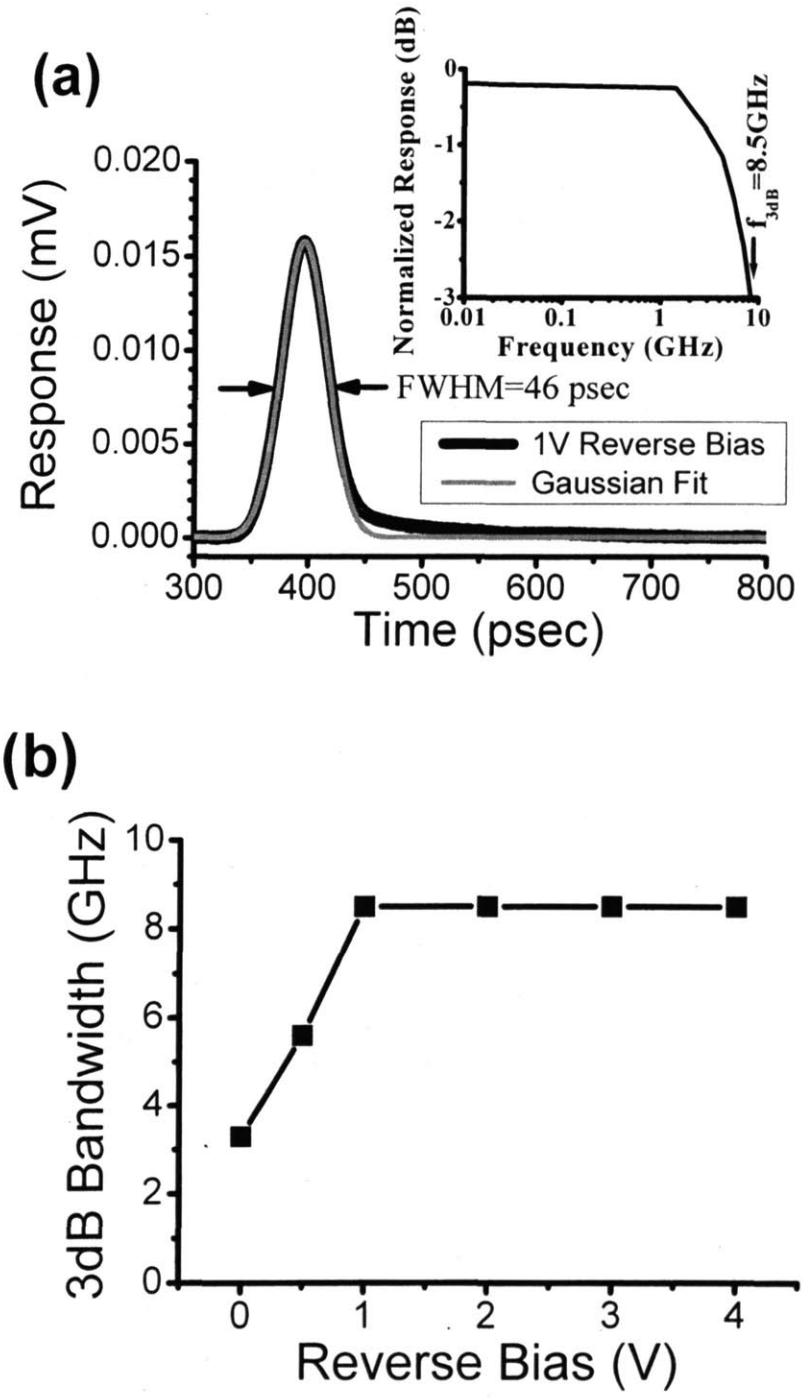

Fig. 3.15 (a) Temporal response of a 10×70 μm² Ge/Si photodetector at a reverse bias of 1 V to ~1 ps-long pulses generated by a mode-locked Yb-fiber laser at 1040 nm (black line). The gray line shows the Gaussian fit to the pulse. The full width at half maximum (FWHM) is 46 ps. The inset of the

figure shows the Fourier transform of the pulse, which gives a 3 dB bandwidth of 8.5 GHz. (b) The 3 dB bandwidth of the device as a function of reverse bias. The full bandwidth is achieved at a low reverse bias of 1 V, which is very compatible with the low driving voltage requirements (≤1.5V) of Si ULSI.

We obtained a 3 dB bandwidth of 8.5 GHz, indicating that the device is suitable for a bit rate of 12 Gb/s [84]. Note that this is a relatively conservative estimate, since a small portion of the pulse broadening is actually contributed by the measurement circuitry instead of the detector itself.

Theoretically, the 3 dB bandwidth is determined by the carrier transit time and RC delay of the device. The transit time limited bandwidth is given by [85]

$$f_{transit} = \frac{0.44 v_{sat}}{W}, \tag{3.3}$$

where v_{sat} is the saturation drift velocity in Ge, and W is the thickness of the intrinsic Ge film. With v_{sat} =6.0×10^6 cm/s [79, 80] and W =2.35 μm in our case, one calculates $f_{transit}$ =11.2 GHz. The RC limited bandwidth is given by:

$$f_{RC} = \frac{1}{2\pi RC}. \tag{3.4}$$

With a load resistance R=50 Ω and the capacitance of the device C=0.18 pF, f_{RC} is determined to be 17.7 GHz. The 3 dB frequency of the device can be estimated by

$$f_{3dB} = \sqrt{\frac{1}{1/f_{transit}^2 + 1/f_{RC}^2}}, \tag{3.5}$$

and it is determined to be 9.5 GHz, using the results of Eqs. 3.4 and 3.5. The calculated result is very close to the measured 3 dB bandwidth of 8.5 GHz. Fig. 3b shows the bandwidth of the device as a function of the reverse bias. The full bandwidth is achieved at a low reverse bias of 1 V, which is very desirable for low voltage operation in Si ULSI.

The bandwidth of the device is mainly limited by the transit time, which can be improved by reducing the film thickness. This is especially applicable for waveguide-integrated Ge detectors, in which the thickness of the Ge can be reduced to ~500 nm and the transit time limited bandwidth can be increased to ~50 GHz. Also, in the current device about 80% of the capacitance is due to the 50×50 μm^2 Al pads on SiO_2. In waveguide-integrated photodetectors these large pads are no longer necessary in every detector device, so the RC limited bandwidth can also be greatly improved.

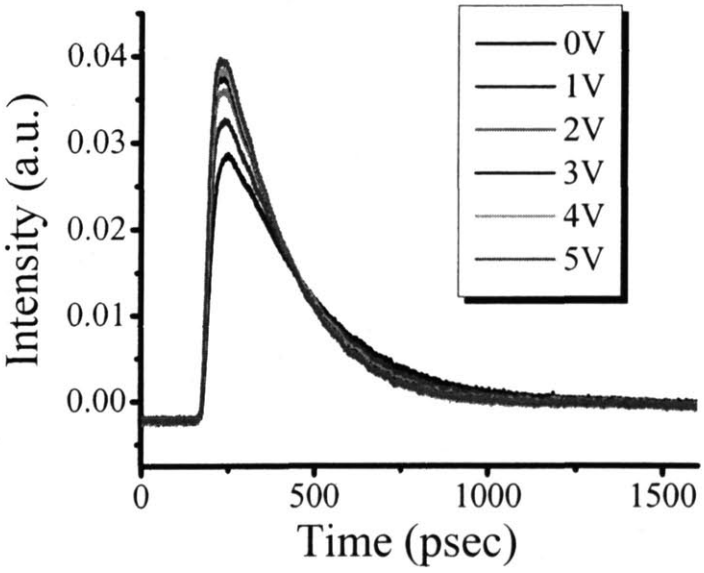

Fig. 3.16. Temporal response of the 10×70 μm^2 Ge/Si photodetector device at 1550 nm

Fig. 3.16 shows the temporal response data measured with a 1550 nm mode-locked Er fiber laser. The measurement circuit set up is the same as Fig. 3.14, except that the incident wavelength is centered at 1550 nm instead of 1040 nm. Compared to the result we measured at 1040 nm, the rise time (the time it takes for the pulse to rise from

10% of the peak intensity to 90% of the peak intensity) is almost the same (~20 ps), while the decay time is much longer.

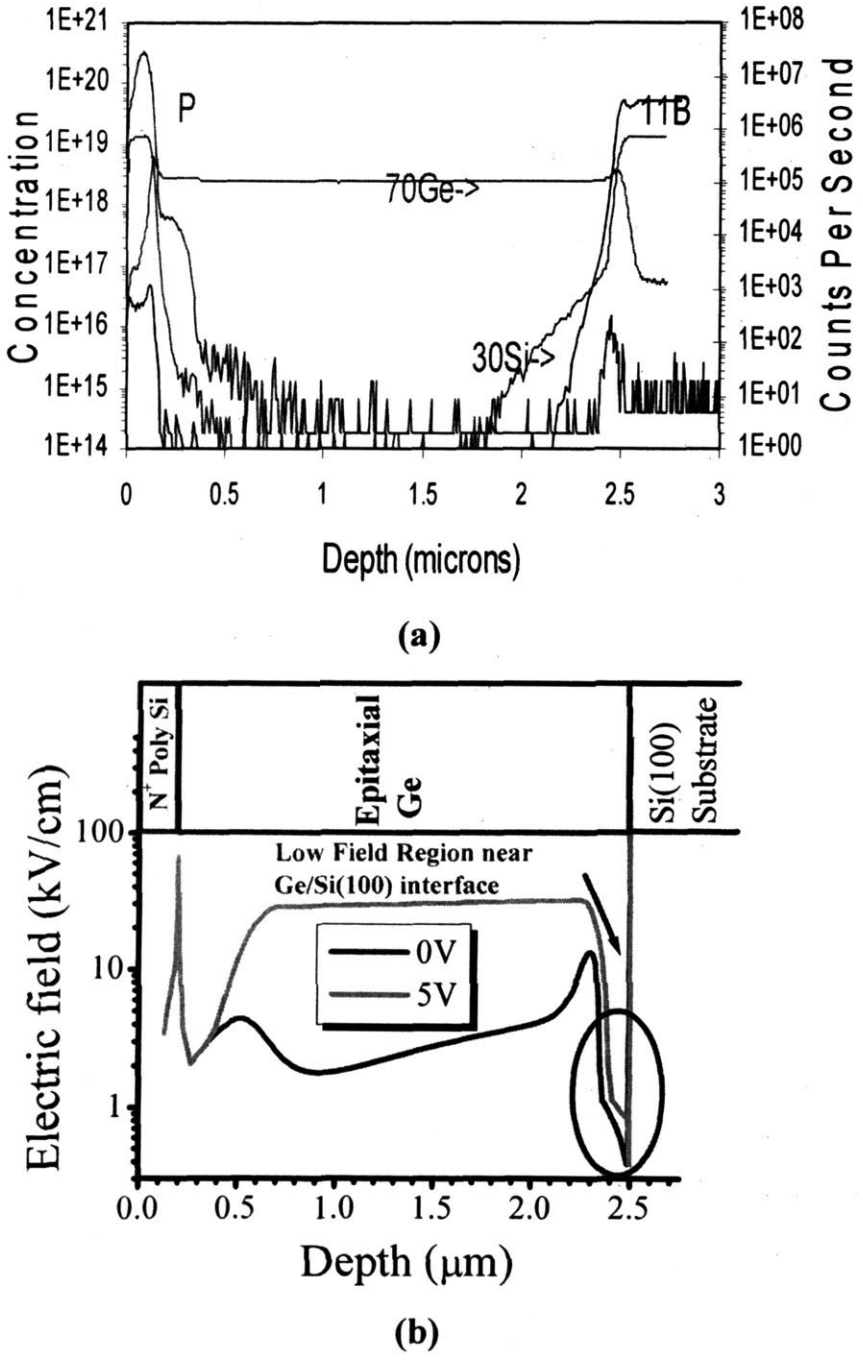

Fig. 3.17. (a) Doping profile from SIMS analysis, and (b) Electric field distribution in the Ge layer at 0V and 5V reverse bias calculated from the doping profile.

The bandwidth obtained from the fast Fourier transform (FFT) of the temporal response is ~2.5 GHz at >3V reverse bias. Since the results are measured on the same device, the difference between the measurement at 1550nm and 1040nm cannot be due to the RC delay. From the doping profile shown in Fig. 3.17 (a), we calculate the electric field distribution in the Ge layer. Because of the B diffusion tail from the p^+ Si substrate to the Ge layer, there is a low electric field region at the interface of the Ge film and the Si substrate. Due to the low field, photon-generated carriers in this region have to diffuse into the depletion region before they are collected, which is much slower than the drift process. This is especially the case for electrons, since the n^+ electrode that collects electrons is about 2 μm away from the Ge/Si interface. As the absorption coefficient of Ge at 1040 nm is as high as 16000/cm [86] and the thickness of the Ge layer in front of this low field region is ~2 μm, only about 4% of the light can reach the low field regime at the Ge/Si (100) interface in the temporal response measurement at 1040 nm. Therefore, the slow carrier diffusion around the Ge/Si (100) interface only contributes to a small tail in the temporal response spectrum in Fig. 3.15(a). In the case of 1550 nm illumination, however, about 50% of the light can reach the Ge/Si (100) interface since the absorption coefficient of 0.2% tensile strained Ge at 1550 nm is 3300/cm, much smaller than that at 1040nm. Therefore, the slow carrier diffusion process near the Ge/Si (100) interface contributes a lot more to the whole response spectrum compared to the case of 1040 nm illumination, and a long tail in the diode's temporal response at 1550 nm is observed in Fig. 3.16. Comparing the response of the detector in the time domain at 1040 nm and 1550 nm, we estimate that the delay due to carrier diffusion around the Ge/Si interface is about 160 ps. Since the low electric field layer around the Ge/Si interface is about 200

nm thick, the diffusivity is estimated to be ~2.5 cm^2/ V sec. Such a low carrier diffusivity could be due to the scattering of defects in this layer, since it includes the low temperature buffer layer grown at 335 °C which has a dislocation network. The fact that we can still collect carriers generated in this region also implies that the carrier lifetime in this region is greater than 160 ps despite of the high dislocation density.

Clearly, B diffusion from the Si substrate has to be suppressed in order to get rid of the slow carrier diffusion process at 1550 nm. Based on the diffusion coefficient of B in Ge [87], we calculated that the B diffusion during the 700°C growth is only less than 20 nm, while the B diffusion during 900°C 1h annealing is as much as 350 nm. Therefore, the most effective method to reduce the B diffusion is to decrease the annealing temperature. For example, an 850°C 1h annealing also helps to get rid of the dislocations and point defects in the Ge layer, while the B diffusion length is <100 nm under this annealing condition. Another way is to use rapid thermal processing (RTP) instead of furnace annealing. For example, a cyclic RTP between 850°C and 650°C with 10 cycles and 30 sec duration at each temperature point has also been proved to remove the defects in the Ge layer, while the total B diffusion length can be reduced to ~30 nm. To sum up, the bandwidth performance of the photodetector at 1550 nm could also be improved to ~8.5 GHz by controlling the doping diffusion during the processing.

3.2.4. Signal-to-Noise Ratio Considerations [88,89,90]

One concern about Ge photodetectors is that the signal-to-noise ratio may be adversely affected by the relatively large dark current as a result of higher intrinsic carrier and dislocation density in the Ge layer compared to III-V materials. In state-of-the-art

digital circuits, a bit error rate (BER) of $<10^{-12}$ is required. In this section we will analyze the signal-to-noise ratio (SNR) of our selectively grown Ge/Si photodetector, and calculate the required input optical power for a BER of $<10^{-12}$ as a function of clocking frequency (f_{clock}) in an digital integrated circuit. The detector noise is mostly from three sources: thermal noise (I_t), shot noise (I_s) and dark current noise (I_d). As the noises are random in nature, the total noise is given by

$$I_{tot}^2 = I_s^2 + I_t^2 + I_d^2 \tag{3.6}$$

Thermal noise, also known as Johnson or Nyquist noise, is caused by the random motions of carriers in resistors at finite temperatures. These motions give rise to a random electric current even in the absence of an external electrical power source. Any resistor in series with the photodetector such as the junction resistance (R_j), series resistance (R_s) or the load resistance (R_l), can give rise to the thermal noise. In our detector we have R_s=30Ω and R_l=50 Ω. Therefore

$$I_t^2 = 4kTf_{clock}\left(\left(\frac{1}{R_s}\right)+\left(\frac{1}{R_l}\right)\right) = 8.9\times10^{-22} f_{clock}\ (A^2), \tag{3.7}$$

Note that thermal noise has nothing to do with the dark current and it is always present since series resistance is inevitable and load resistance is required in a transceiver circuit. At f_{clock}=8.5 GHz (the 3dB frequency of the detector) we have I_t=2.7 μA from Eq. 3.7.

Shot noise is due to the fact that photons arrive at a photodetector at random intervals. As a result, the signal has some variation with time. The higher the clocking frequency or the smaller the time interval we are looking at, the more fluctuations we see. Assuming an input optical power of P_{in}, and considering a DC responsivity of 0.56A/W at 1550nm and the frequency response of the detector $R(f)$ in Fig. 3.15, we have

$$I_s^2 = 2ef_{clock}R(f_{clock})P_{in} \tag{3.8}$$

With P_{in}=0.1 mW and f_{clock}=8.5 GHz, we have $I_s = 0.33\mu A$.

The dark current noise is due to the random generation of electron/hole pairs in the depletion region. In our device the dark current at -1V is 0.8 μA. So we have

$$I_d^2 = 2ef_{clock}I_{dark} = 2.6\times10^{-25}f_{clock}(A)^2 \tag{3.9}$$

With f_{clock}=8.5 GHz we have $I_d = 0.047\mu A$. From the analysis above, we find that the noise related to dark current is 1-2 orders of magnitude smaller than the thermal noise and shot noise of the circuits. Therefore, the noise due to dark current can be neglected.

The signal-to-noise ratio is given by

$$SNR = \frac{I_p}{I_{tot}}, \tag{3.10}$$

where I_p is the photocurrent and I_{tot} is the total noise current. The BER is related to SNR by

$$BER \approx \frac{1}{2\pi}\frac{e^{-SNR^2/2}}{SNR}. \tag{3.11}$$

Fig. 3.18 shows the required input optical power of our Ge/Si photodetector for a BER of $<10^{-12}$ as a function of clocking frequency (f_{clock}) in a digital integrated circuit. Only 60 μW input power is needed for 10 GHz operation. The optical power available in telecommunication network is in the order of mW. Therefore, the Ge/Si detector is applicable in the state-of-the-art telecommunication network in terms of bandwidth, power consumption and bit error rate.

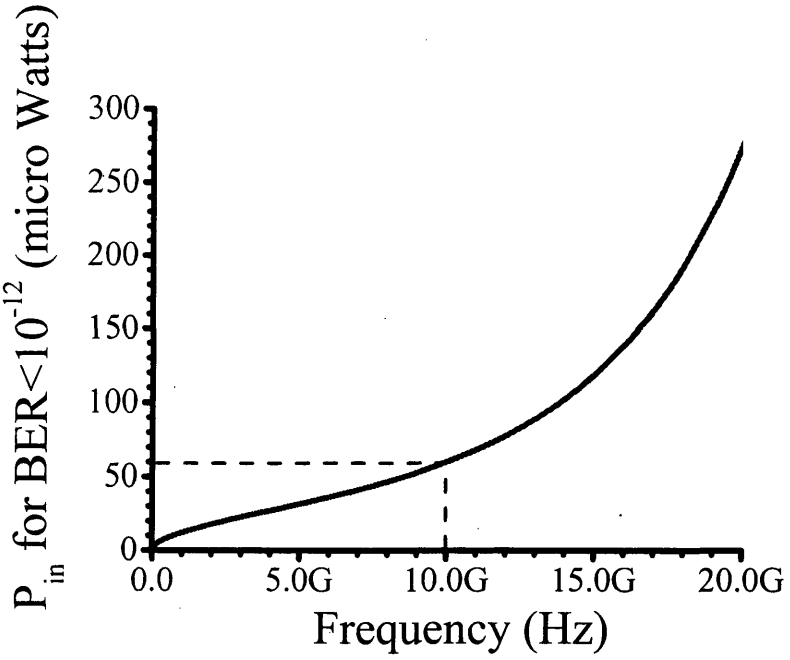

Fig. 3.18. Required input optical power of the Ge/Si photodetector for a bit error rate (BER) of $<10^{-12}$ as a function of clocking frequency (f_{clock}) in a digital integrated circuit.

Chapter 4: Design of Waveguide-Integrated GeSi Electro-absorption Modulators and Photodetectors

In the previous chapter we focused on discrete photodetectors for free space light coupling. However, electron-photonic integrate circuits (EPIC) requires the integration of waveguides with modulators and photodetectors on a single chip. In this chapter we present the design of $Ge_{1-x}Si_x$ electro-absorption (EA) modulators and photodetectors integrated with Si waveguides. We first begin with the Franz-Keldysh (FK) effect in Ge and GeSi material, including an experimental study on the Franz-Keldysh effect in epitaxial Ge films on Si and its comparison with the theoretical results predicted by FK theory. We then discuss the figure of merit (FOM) of the electro-absorption (EA) modulator material and present a composition design of the $Ge_{1-x}Si_x$ material for optimal EA modulation around 1550nm. Finally, we design a butt-coupling scheme from Si(core)/SiO_2(cladding) waveguide to the GeSi EA modulator or photodetector. Device dimensions are optimized for the optimal overall performance.

4.1 Franz-Keldysh Effect in Ge and GeSi materials

4.1.1 Physical Model of Franz-Keldysh Effect

We have briefly discussed the effect of electric field on the dielectric function of semiconductor materials in Chapter 2 to explain the physical principles of photoreflectance (PR) measurements. In fact, the PR measurement result itself already indicates that Franz-Keldysh (FK) effect is present in epitaxial Ge film on Si. Here we

present some more detailed discussions on the FK effect, especially the derivation of absorption coefficient as a function of electric field and photon energy.

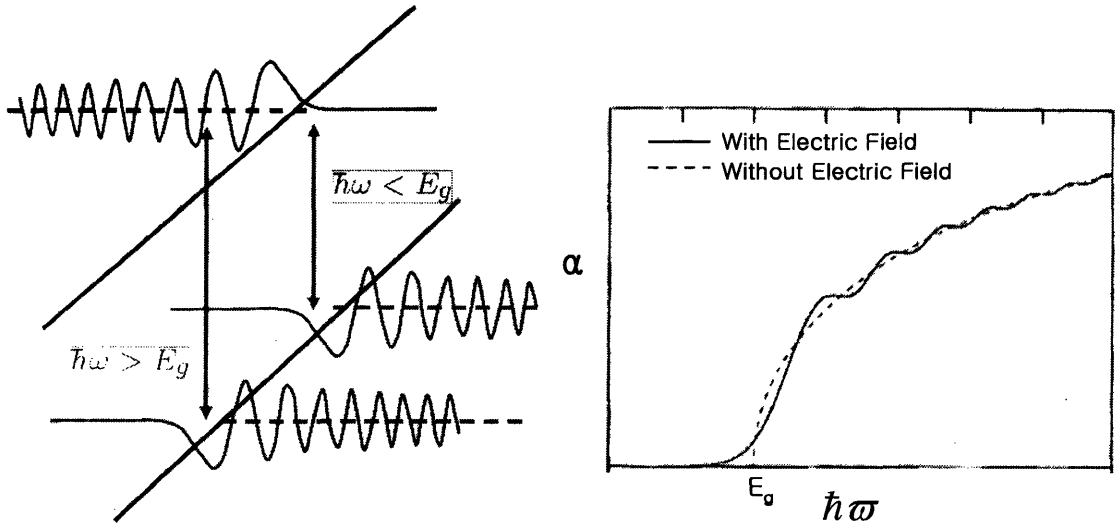

Fig. 4. 1 Schematic diagrams showing the physical principle of Franz-Keldysh effect (left) and its effect on the absorption spectrum of a semiconductor material (right).

The left hand side of Fig. 4.1 schematically shows the wave function of the conduction and valence bands in the presence of an electric field. An important feature is that the evanescent tails of the wave functions in the conduction and valence bands significantly extend into the band gap due to the electric field, meaning the electrons and holes have a certain probability of tunneling into the band gap. Due to this tunneling process, even the photon energy ($\hbar\omega$) is smaller than the band gap (E_g) it still has a chance to excite an electron from the valence band to the conduction band in the presence of an electric field. Therefore, for photon energy $\hbar\omega < E_g$ the absorption coefficient increases with the applied electric field, as shown in the right hand side of Fig. 4.1. On the other hand, for $\hbar\omega > E_g$ the possibility of transition is related to the overlap of the

oscillating wave functions inside the conduction and valence bands under a given electric field and a photon excitation of $\hbar\omega$. Due to the interference of the electron waves in the conduction and valence bands, the transition is enhanced for some photon energy, while reduced for other photon energies for $\hbar\omega > E_g$. It is very much like a Fabre-Perot effect in optics. Therefore, for $\hbar\omega > E_g$ the absorption coefficient oscillates as a function of photon energy. This is the so-called Franz-Keldysh oscillations. On the whole, one can expect an absorption spectrum change shown on the right hand side of Fig. 4.1.

For a quantitative study on the absorption coefficient vs. electric field, we consider the Schrödinger's equation of an electron-hole pair in the presence of an electric field [91]. For simplicity we assume a uniform electric field along the z direction in the derivation. This is a fairly good approximation, for a $p-i-n$ diode structure is usually used to apply a high and nearly uniform electric field in the intrinsic region, and the electric field is perpendicular to the surface of the device. We also assume the effect of the applied electric field dominates over the exciton effect related to electron-hole interactions, so that we can neglect the Coulomb potential of electron-hole interaction in the derivation. We further focus our considerations on the electrons and holes near the band edges of the conduction and valence bands since they contribute the most to the band-to-band transitions. Now we have

$$\left(-\frac{\hbar^2}{2m_r}\frac{d^2}{dz^2} + eFz\right)\phi(z) = E_z\phi(z), \tag{4.1}$$

where $m_r = m_e m_h/(m_e + m_h)$ is the reduced effective mass of electrons and holes. The total energy E is given by

$$E = \frac{\hbar^2}{2m_r}(k_x^2 + k_y^2) + E_z . \tag{4.2}$$

To solve Eq. 4.1, we change the variable

$$Z = \left(\frac{2m_r eF}{\hbar^2}\right)^{1/3}\left(z - \frac{E_z}{eF}\right). \tag{4.3}$$

Therefore, Eq. 41 transforms into

$$\frac{d^2\phi(Z)}{dZ^2} - Z\phi(Z) = 0 . \tag{4.4}$$

This is a classical differential equation and the solutions are the Airy functions $Ai(Z)$ and $Bi(Z)$. Because the wave function has to decay as z approaches $+\infty$, $Ai(Z)$ has to be chosen. Under the normalization condition

$$\int_{-\infty}^{+\infty} \phi_{E_{z1}}(z)\phi_{E_{z2}}(z)dz = \delta(E_{z1} - E_{z2}) \tag{4.5}$$

and continuous requirement of the wave function, we have the solution

$$\phi_{E_z}(z) = \left(\frac{2m_r}{\hbar^2}\right)^{1/3} \frac{1}{(eF)^{1/6}} Ai\left[\left(\frac{2m_r eF}{\hbar^2}\right)^{1/3}\left(z - \frac{E_z}{eF}\right)\right]. \tag{4.6}$$

Therefore, the total wave function is

$$\psi_{k_x,k_y,E_z}(\vec{r}) = \frac{e^{i(k_x x + k_y y)}}{\sqrt{A}}\phi_{E_z}(z), \tag{4.7}$$

where A is the area. On the other hand, it can be derived from Fermi's Golden Rule that the absorption coefficient is given by

$$\alpha(\varpi) = \frac{\pi e^2 E_p}{3n_r c\varepsilon_0 m_0 \varpi}\sum_n |\phi_n(\vec{r} = 0)|^2 \, \delta(E_n + E_g - \hbar\varpi). \tag{4.8}$$

where n_r is the real part of the refractive index of the material, and E_p is a constant related to the transition matrix element of the material. E_p =26.3 eV for Ge [27]. Substituting Eq. 4.7 into 4.8 , we have

$$\alpha(\varpi) = \frac{\pi e^2 E_p}{3 n_r c \varepsilon_0 m_0 \varpi} \sum_{k_x} \sum_{ky} \int \frac{dE_z}{A} | e^{i(k_x x + k_y y)} \phi_{E_z}(z) |^2_{x,y,z=0} \, \delta(E_t + E_z + E_g - \hbar\varpi), \quad (4.9)$$

where $E_t = \frac{\hbar^2 (k_x^2 + k_y^2)}{2m_r} = \frac{\hbar^2 k_t^2}{2m_r}$ is the kinetic energy in the transverse plane (x-y plane).

Since

$$\frac{1}{A} \sum_{k_x, k_y} = \int \frac{d^2 k_t}{(2\pi)^2} = \frac{m_r}{2\pi\hbar^2} \int dE_t , \quad (4.10)$$

we have

$$\alpha(\omega) = \frac{e^2 E_p}{6 n_r c \varepsilon_0 \varpi \hbar^2} \left(\frac{m_r}{m_0} \right) \int\int dE_t dE_z \, | \phi_{E_z}(z=0) |^2 \, \delta(E_t + E_z + E_g - \hbar\omega)$$

$$= \frac{e^2 E_p}{6 n_r c \varepsilon_0 \omega \hbar^2} \left(\frac{m_r}{m_0} \right) \int_{-\infty}^{\hbar\omega - E_g} dE_z \, | \phi_{E_z}(z=0) |^2$$

$$= \frac{e^2 E_p}{6 n_r c \varepsilon_0 \omega \hbar^2} \left(\frac{m_r}{m_0} \right) \int_{-\infty}^{\hbar\omega - E_g} dE_z \left(\frac{2 m_r}{\hbar^2} \right)^{2/3} \frac{1}{(eF)^{1/3}} Ai^2 \left[\left(\frac{2 m_r eF}{\hbar^2} \right)^{1/3} \left(z - \frac{E_z}{eF} \right) \right]$$

(4.11)

Let $\hbar\theta_F = \left(\frac{\hbar^2 e^2 F^2}{2m_r} \right)^{1/3}$, $\tau = -\frac{E_z}{\hbar\theta_F}$, $\eta = \frac{E_g - \hbar\omega}{\hbar\theta_F}$, we find the integral is equal to

$$\alpha(\omega) = \frac{e^2 E_p}{12 n_r c \varepsilon_0 m_0 \omega} \left(\frac{2m_r}{\hbar^2} \right)^{3/2} \sqrt{\hbar\theta_F} \left[-\eta Ai^2(\eta) + Ai'^2(\eta) \right], \quad (4.12)$$

where $Ai'(\eta)$ is the derivative of $Ai(\eta)$.

Eq. 4.12 quantitatively describes the effect of electric field on the absorption of a semiconductor material. Note that this equation only considers electron-photon interaction, so it is only suitable for direct gap transitions. It also neglects the exciton effect, which could be significant for photon energies slightly larger than the direct band gap. In the case of Ge and GeSi, though, we are indeed mostly interested in the FK effect of the direct gap because its magnitude is about three orders higher than that of the indirect gap [92,93], and the wavelength regime we are interested in (1520-1650 nm) is much closer to the direct gap (~1550-1610 nm depending on the tensile strain) than the indirect gap (~1900 nm, less sensitive to the strain than the direct gap). Further, we are mostly interested in the FK effect in the weakly absorbing regime of Ge and GeSi, where the photon energy is smaller than the direct gap. This is because this regime will see a significant relative change in the absorption coefficient under the applied electric field due to the low absorption background at 0 electric field and high sensitivity of absorption to electric field in the tunneling process for $\hbar\omega < E_g$. The exciton effect in this region is much smaller than that around the band edge. Therefore, this model can be applied to calculate the electro-absorption modulation in the weakly absorbing regime below the direct band gap of Ge.

4.1.2 Franz-Keldysh Effect in Tensile Strained Ge

Franz-Keldysh effect of the direct band gap in bulk Ge materials has been studied by several authors [92,93, 94,95,96]. Both the absorption enhancement below the direct band gap and the FK oscillations above the direct band gap have been observed. The experimental results generally agree with the FK theory, but in some cases the FK theory

is not quantitatively consistent with the experimental data due to the neglect of the exciton effect. To study the FK effect in our tensile strained Ge/Si, *p-i-n* diodes similar to those mentioned in Chapter 3 are fabricated. The only difference is that the Ge thickness is decreased to 1.3 μm so that a significantly large electric field can be applied to the intrinsic Ge layer at a reasonably low reverse bias. The tensile strain in the Ge layer is 0.193%. The residual doping level in the intrinsic region calculated from C-V data was ~ 10^{16} cm^{-3}, or about three orders of magnitude lower than the n^+ phosphorus and the p^+ boron doping levels. Accordingly, the Ge layer is fully depleted and the electric field under applied reverse bias was nearly uniform in the Ge epitaxial layer. To obtain the absorption coefficients under different electric fields, we measure the responsivity of the diode at different bias and derive the absorption coefficient with Eq. 3.3. The relation between electric field and applied reserve bias is calculated using a one dimensional finite-difference simulator. The calculated result is shown in Fig. 4.2. The biases used in the experimental study are marked by the black squares in the figure. It is clear that with a bias of $\leq 5V$ we can achieve a large electric field of 70 kV/cm. Such a high level of electric field should induce significant FK effect according to Eq. 4.12

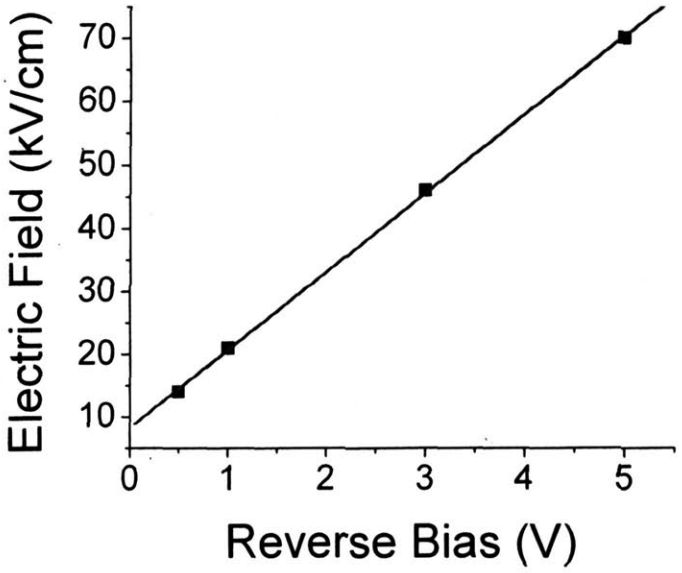

Fig. 4. 2. The relation between the electric field in the intrinsic Ge layer (1.3 μm thick) and the reverse bias calculated by a one dimensional finite difference simulator. The black squares indicate the biases used in the experimental study.

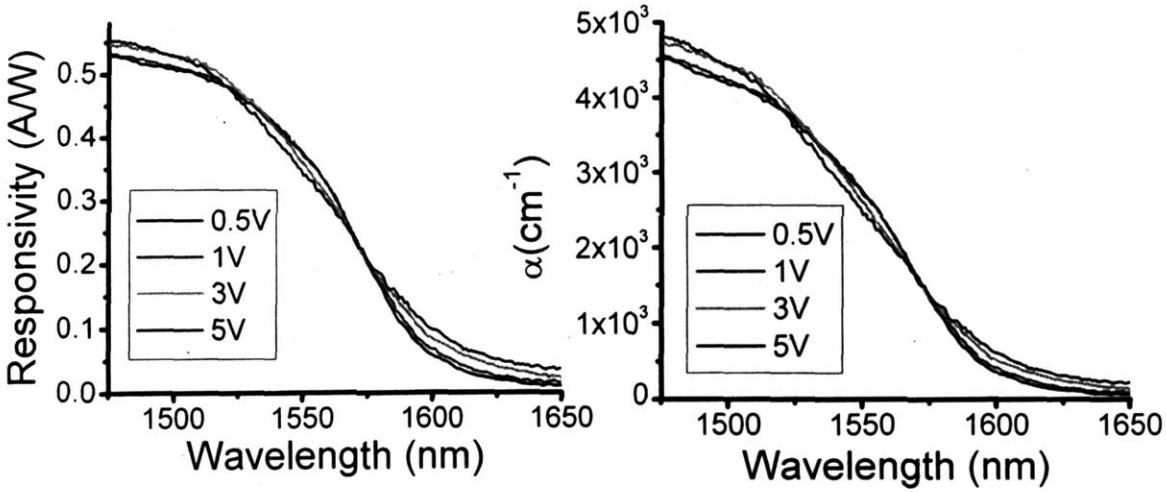

Fig. 4. 3. (a) Responsivity of a 300μ- diameter Ge/Si diode with 1.3 μm thick Ge layer at different biases. (b) The derived absorption coefficient at different biases.

The responsivity at different biases of a 300μm-diameter diode is shown in Fig. 4.3(a). At 0.5-5V bias, one can clearly see that as the bias increases the responsivity is enhanced at some wavelengths, while reduced at other wavelengths. For example, compared to the responsivity measured at 0.5V reserves bias, the one measured at 5V reverse bias shows an increase in responsivity for 1570-1650nm, a decrease for 1520-1569 nm, and an increase again for 1475-1520nm. Note that this phenomenon is obviously not due to the enhancement in collection efficiency at higher bias, because in that case the responsivity should be enhanced at all wavelengths instead of being oscillated. The derived absorption coefficients at different biases are shown in Fig. 4.3b. The experimental results we observed is consistent with the features of the FK effect described previously, i.e., the absorption increases below the band gap and oscillates above the band gap.

The Franz-Keldysh effect in tensile strained Ge can be modeled with the theory we described in Sec. 4.1.1. In this model, we mainly consider the FK effect of the direct band gap of Ge, because it dominates the absorption in the wavelength range we are interested in (1450-1650nm). As the light and heavy hole bands become non-degenerate under tensile strain, the absorption coefficient of the direct gap is modeled with a modification of Eq. 4.12:

$$\alpha(\omega)=\frac{e^2E_p}{12n_rc\varepsilon_0m_0\omega}\left\{\left(\frac{2m_{r,lh}}{\hbar^2}\right)^{3/2}\sqrt{\hbar\theta_{F,lh}}\left[-\eta_{lh}Ai^2(\eta_{lh})+Ai'^2(\eta_{lh})\right]+\left(\frac{2m_{r,hh}}{\hbar^2}\right)^{3/2}\sqrt{\hbar\theta_{F,hh}}\left[-\eta_{hh}Ai^2(\eta_{hh})+Ai'^2(\eta_{hh})\right]\right\}$$

$$\text{where } m_{r,lh} = \frac{m_e^{\Gamma} m_{lh}}{m_e + m_{lh}},\ m_{r,hh} = \frac{m_e^{\Gamma} m_{hh}}{m_e + m_{hh}},\ \hbar\theta_{F,lh} = \left(\frac{\hbar^2 e^2 F^2}{2m_{r,lh}}\right)^{1/3},\ \eta_{lh} = \frac{E_g^{lh} - \hbar\varpi}{\hbar\theta_{F,lh}},$$

$$\hbar\theta_{F,hh} = \left(\frac{\hbar^2 e^2 F^2}{2m_{r,hh}}\right)^{1/3} \text{ and } \eta_{hh} = \frac{E_g^{lh} - \hbar\varpi}{\hbar\theta_{F,hh}}. \tag{4.13}$$

This is because the absorption from the direct gap is a combination of the transitions from the light and heavy hole bands. The material constants of Ge are: $E_P = 26.3eV$, $E_g^{lh} = 0.773eV$, $E_g^{hh} = 0.785eV$, $m_e^{\Gamma} = 0.038m_0$ (note that this is the electron effective mass at Γ *valley* instead of L valley), $m_{lh} = 0.043m_0$ and $m_{hh} = 0.33m_0$ [27]. The FK effect of the indirect gap is three orders of magnitude lower than that of the direct gap and can be neglected in the modeling [92,93]. The contribution of the indirect gap to the absolute absorption coefficients in the wavelength range of 1450-1650 nm is not negligible, though, and it is obtained by extrapolating the experimental data in Ref. [92]. The total absorption coefficient is a sum of the contribution from the direct and indirect band gaps of Ge.

The calculated absorption spectra under different electric fields are compared to the experimental results in Fig. 4.4. The theoretical and experimental results are in reasonable good agreement with each other. The calculated absorption coefficient is slightly less than the experimental results right near the heavy hole band gap E_g^{hh}. This is probably because we did not consider the exciton absorption in our model, which could be significant near the band edge. This is not a big issue for our purpose, though, since we are more interested in the wavelength regime of >1600 nm to obtain low background absorption for the modulator device, as will be discussed in the next section.

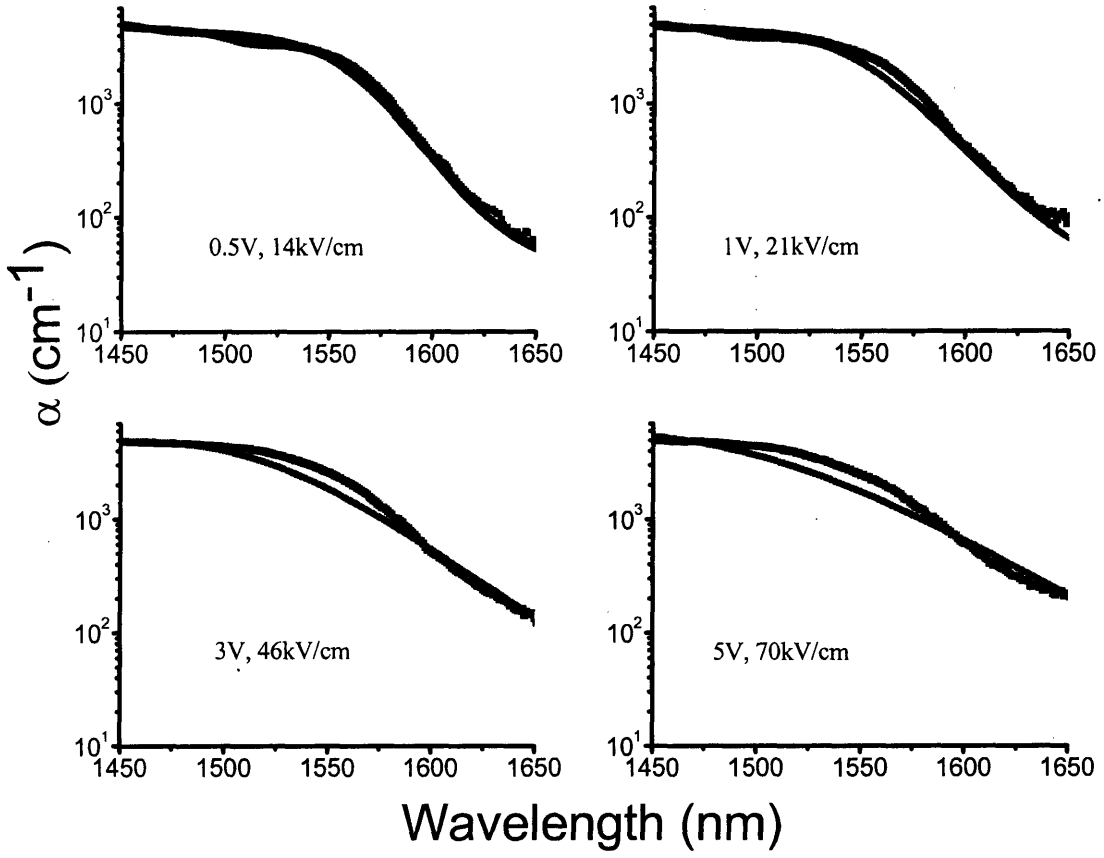

Fig. 4. 4 Comparison of the absorption spectra of tensile strained Ge at different electric field with theoretical calculations.

4.1.3 Figure of Merit of Electro-absorption Modulator Materials.

In this section we will discuss what material parameters should we optimize for an EA modulator. Two most important characteristics of modulators are the insertion loss and extinction ratio. Insertion loss refers to the loss of optical power at the optical "on" state in terms of dB. At optical "on" state the modulator is supposed to be completely transparent to light, but due to the material absorption, the scattering loss associated with the surface/sidewall roughness of the modulator, and/or the optical mode mismatch between the waveguide and modulator, there could still be some loss at optical "on" state,

leading to a non-zero insertion loss. Since we focus on the material properties in this section, we only consider the contribution of the material absorption loss. Therefore,

$$Insertion\ loss(dB) = -10\lg(e^{-\alpha_{on}L}) = 4.343\alpha_{on}L, \tag{4.14}$$

where α_{on} is the absorption coefficient of the material at the optical "on" state and L is the length of the device.

Extinction ratio refers to the ratio of the output optical power from the modulator at optical "off" state (opaque state) to that at the "on" state (transparent state) in terms of dB. In the case of EA modulator, the absorption coefficient of the modulator material at the operating wavelength is enhanced by applying a larger reverse bias at optical "off" state compared to "on" state, so less light comes out of the device at "off" state than "on" state. The higher the extinction ratio, the larger the difference in output power between "on" and "off" states, and the higher the signal-to-noise ratio. It is easy to derive that

$$Extinction\ ratio(dB) = -10\lg\left(\frac{e^{-\alpha_{off}L}}{e^{-\alpha_{on}L}}\right) = 4.343(\alpha_{off} - \alpha_{on}) = 4.343\Delta\alpha \tag{4.15}$$

Obviously, we need a modulator with low insertion loss and high extinction ratio. Therefore, a basic figure of merit for an EA modulator material can be expressed as:

$$FOM_{basic} = \frac{Extinction\ \ Ratio}{Insertion\ \ loss} = \frac{\Delta\alpha}{\alpha_{on}} \tag{4.16}$$

We call it "basic FOM" because it has not considered other important factors of the modulator yet, like bandwidth, power consumption, etc. Note that given the same applied electric field at the optical "off" state, this basic FOM is only related to the optoelectronic properties of the material if we do not consider coupling loss. Therefore, it can be used as

a useful guide for the choice of an EA modulator material working at a certain wavelength.

For maximum $\Delta\alpha/\alpha_{on}$ we need a small α_{on} and a large $\Delta\alpha$. For a small α_{on} we would like to work at a weakly absorbing regime where $\hbar\omega < E_g^{\Gamma}$, so that only the indirect gap contributes to a relatively low background absorption. For a large $\Delta\alpha$, $\hbar\omega$ has to be close to the direct band gap (E_g^{Γ}) since the FK effect is most significant around the band edge. Therefore, we expect to see a maximum $\Delta\alpha/\alpha_{on}$ at a photon energy slightly smaller than the direct band gap. Fig. 4.5 plots $\Delta\alpha/\alpha_{on}$ of 0.193% tensile strained Ge as a function of wavelength from both experimental results and theoretical calculations. Here at "on" state the reverse bias $V_{on} = 0.5$ V (F=14 kV/cm), while at "off" state the bias V_{off} =5 V (F=70 kV/cm). As shown in the figure, both the theoretical and experimental results show that $\Delta\alpha/\alpha_{on}$ is optimized at ~1647nm. As expected, the corresponding photon energy is 0.753 eV, slightly smaller than the direct gap of 0.193% tensile strained Ge (0.773 eV). The theoretical calculation predicts an optimal $\Delta\alpha/\alpha_{on}$ of 3.1, while experimental result demonstrates a $\Delta\alpha/\alpha_{on}$ of ~2.7, in reasonably good agreement with the theoretical prediction. This result indicates that the approximations in Eq. 4.12 and 4.13 are applicable to predict the basic FOM of tensile strained Ge as an EA modulator material. By comparison, the bulk Ge material can only achieve a $\Delta\alpha/\alpha_{on}$ of ~1.1 at 1647 nm [92]. This is because the strain shifts the direct band edge closer to 1647 nm and the FK effect of the direct band gap exerts more influence at this wavelength. From Fig. 4.5 we can see that the 0.193% tensile strained Ge has a $\Delta\alpha/\alpha_{on}$ of >2 in the

wavelength range of 1633-1660nm. Therefore, an EA modulator device made of this material can achieve an extinction ratio of ≥8dB at the cost of 4dB insertion loss in this wavelength range. From the results above, we can conclude that tensile strained Ge is a good candidate material for EA modulation in the L-band of telecommunications.

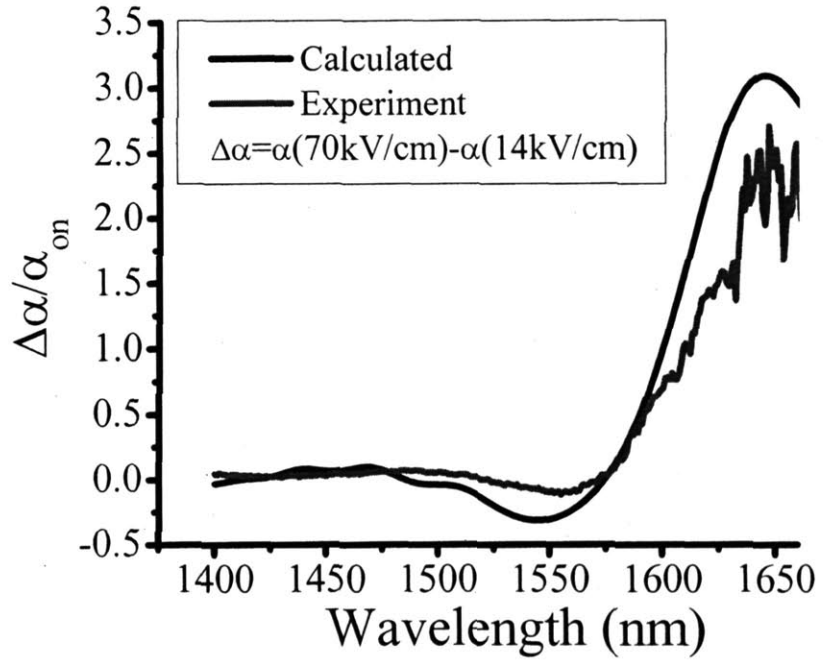

Fig. 4. 5. Experimental and theoretical $\Delta\alpha/\alpha_{on}$ vs. wavelength for 0.193% tensile strained Ge material

4.1.4 Material Design of $Ge_{1-x}Si_x$ for Optimal EA Modulation Properties at 1550nm

For telecommunications 1550nm is the most interesting wavelength because it has the lowest transmission loss in SiO_2 optical fibers. As discussed in the previous section, tensile strained Ge is most suitable for optical modulation at in the wavelength range of 1633-1650 nm and is not adequate for applications at 1550nm. To optimize the performance of the material at 1550nm, we must shift the band edge of the Ge to higher energy (shorter wavelength) by doping a small amount of Si. From Eq. 4.13, we can see that the band gap, the refractive index, the effective masses and the transition matrix

energy E_p are needed to calculate the absorption coefficient of $Ge_{1-x}Si_x$ under the electric field. Next we will have a detailed discussion on these basic material parameters of $Ge_{1-x}Si_x$.

The direct gap of Si at room temperature is 4.06 eV, and the direct gap of $Ge_{1-x}Si_x$ alloy can be linearly interpolated between Si and Ge by $E_g^{\Gamma}(Ge_{1-x}Si_x) = 0.80 + 3.26x$ [97,98,99]. For example, with 2% Si incorporation the direct band gap of zero-strained GeSi can already be shifted from 0.800 to 0.865 eV, which corresponds to a wavelength shift from 1550 to 1428 nm. Therefore, addition of less than 2% Si can already significantly modify the absorption of Ge in the C and L bands. A $Ge_{1-x}Si_x$ alloy with dilute Si doping (x<2%) is our candidate material for the EA modulator operating at 1550nm. The indirect bandgap shift for x<15% is given by: $E_g^{L}(Ge_{1-x}Si_x) = 0.66 + 1.2x$ [100,101]. The indirect band edge shift would modify the absorption coefficient at optical "on" state since it is mainly due to the indirect gap absorption. Compared to the shift of the direct gap, the indirect gap shift is much less at the same Si content. Therefore, the direct and indirect gaps become further and further apart with the addition of Si, which deteriorates the optoelectronic properties of the material since it becomes more and more like an indirect gap material. With the interpolation of band gap described above, we can calculate the effect of Si composition on the band gap of $Ge_{1-x}Si_x$ material.

To calculate the band gap of $Ge_{1-x}Si_x$, we also have to take into account the effect of tensile strain. As the $Ge_{1-x}Si_x$ materials with x<0.02 has almost the same thermal expansion coefficient as pure Ge [102], the thermally induced tensile strain in the blanket epitaxial $Ge_{1-x}Si_x$ material is also ~0.2%, as confirmed by our XRD studies on blanket $Ge_{1-x}Si_x$ films with Si composition x<5%. When we make a $Ge_{1-x}Si_x$ modulator device, it

is selectively grown in an elongated rectangular window defined on the Si substrate. This method enables an easy coupling with low loss Si waveguides, as will be discussed in more detail in the next session. The shape of the device is elongated because we need a small cross-section ($<1\times1$ μm^2) to keep the device single mode, while it has to be long enough (tens of μm) to achieve a high enough extinction ratio. As we have discussed in Chapter 2, Section 2.2, due to the faceting induced elastic strain relaxation such structures are strained in the longitudinal direction while almost fully relaxed in the transverse direction. The strain in the longitudinal direction remains similar to the blanket film when the length is > 50 μm. Such an anisotropic in-plane strain in the structure is very different from the isotropic in-plane strain in the blanket $Ge_{1-x}Si_x$, and it affects the band structure differently. Due to kinetic reasons, faceting during the Ge selective growth can be suppressed if the growth rate is fast enough. It has been reported that no facets were formed during the Ge growth by reduced pressure chemical vapor deposition (RPCVD) when the growth rate exceeds 1600 nm/h [103]. The maximum Ge growth rate we can achieve in our UHV-CVD system is ~500 nm/h, and it has been reported that at this growth rate faceting still occur during the growth [67]. Therefore, we consider that our $Ge_{1-x}Si_x$ grown in an elongated rectangular trench would have ~0.2% strain along the trench direction while almost relaxed in the transverse direction. In device fabrications, trenches defined by lithography are usually along the <110> direction, because the flat of the Si wafer is cut along the <110> direction and it is used to align the wafers in the lithography. So now we will consider the band structure modification due to a ~0.2% tensile strain along the [011] direction of $Ge_{1-x}Si_x$. Let us call the longitudinal strain ε_L, transverse strain ε_T, and the strain perpendicular to the substrate $\varepsilon_\perp$. We have $\varepsilon_L \approx 0.2\%$,

and $\varepsilon_T \approx 0$ due to the strain relaxation in the transverse direction. Since the film is free to expand in the vertical direction, the stress perpendicular to the film $\sigma_\perp = (C_{12}\varepsilon_L + C_{12}\varepsilon_T + C_{11}\varepsilon_\perp) = 0$. Therefore we have $\varepsilon_\perp = -C_{12}(\varepsilon_L + \varepsilon_T)/C_{11} \approx -C_{12}\varepsilon_L / C_{11}$. In this case, the light hole, heavy hole and split-off band gaps are given by [31]

$$E_g^\Gamma(lh) = E_g^\Gamma(0) + a(\varepsilon_L + \varepsilon_T + \varepsilon_\perp) - 1/4\left[(\delta E_{100})^2 + 3(\delta E_{111})^2\right]^{1/2} - 1/4(\delta E_{100} + 3\delta E_{111})^2/\Delta_0;$$

$$E_g^\Gamma(hh) = E_g^\Gamma(0) + a(\varepsilon_L + \varepsilon_T + \varepsilon_\perp) + 1/4\left[(\delta E_{100})^2 + 3(\delta E_{111})^2\right]^{1/2} - 3/32(\delta E_{100} - \delta E_{111})^2/\Delta_0,$$

$$E_g^\Gamma(so) = E_g^\Gamma(0) + \Delta_0 + a(\varepsilon_L + \varepsilon_T + \varepsilon_\perp) + 1/4\left[(\delta E_{100})^2 + 3(\delta E_{111})^2\right]^{1/2} + 3/32(\delta E_{100} - \delta E_{111})^2/\Delta_0$$

where $\delta E_{100} = 2b(\varepsilon_L + \varepsilon_T - 2\varepsilon_\perp) \approx 2b(1 + 2C_{12}/C_{11})\varepsilon_L$, and

$$\delta E_{111} = (d/\sqrt{3})(S_{44}/S_{12})\varepsilon_\perp \approx (d/\sqrt{3})(S_{44}/S_{12})(-C_{12}\varepsilon_L/C_{11}) = \frac{d}{\sqrt{3}}\frac{(C_{11}-C_{12})(C_{11}+2C_{12})}{C_{44}C_{11}}\varepsilon_L$$

(4.17)

In Eq. 4.17, $E_g^\Gamma(0)$ is the direct band gap of the material with no strain, d is the devitorial deformation potential in <111> direction, C_{44} is an elastic constant matrix element, $S_{44} = 1/C_{44}$ and $S_{12} = \dfrac{-C_{12}}{(C_{11}-C_{12})(C_{11}+2C_{12})}$ are the compliance constants, and the definition of other parameters are the same as Eq. 2.1.

Although we do not know the deformation potential of the direct gap of $Ge_{1-x}Si_x$ alloy with x<0.02, it is a good approximation just to linearly interpolate between the deformation potentials of the direct band gaps of Ge and Si, as well as the elastic constants [102]. The deformation potential constants of the direct gap of Si are $a(Si)$=-

5.1 eV, $b(Si)$ = -2.2 eV and $d(Si)$ = -4.8 eV. [47]. From our study in Chapter 2 we have determined $a(Ge) = -8.97\,\text{eV}$ and $b(Ge) = -1.88\,\text{eV}$, and $d(Ge) = -4.7\,\text{eV}$ from literature [47]. Using linear interpolation we have $a(Ge_{1-x}Si_x) = -(8.97 - 3.87x)eV$, $b(Ge_{1-x}Si_x) = -(1.88 + 0.32x)eV$, and $d(Ge_{1-x}Si_x) = -(4.7 + 0.1x)eV$. The elastic constants of $Ge_{1-x}Si_x$ are given by $C_{11}(Ge_{1-x}Si_x) = (128.53 + 37.27x)eV$, $C_{12}(Ge_{1-x}Si_x) = (48.26 + 15.64x)eV$, $C_{44}(Ge_{1-x}Si_x) = (66.80 + 12.80x)eV$. Substituting these deformation potential constants and elastic constants into Eq. 4.17, we can evaluate the band gap shift of $Ge_{1-x}Si_x$ due to strain.

To calculate the absorption coefficient with Eq. 4.13, we also need the refractive index, effective masses and transition matrix energy E_p. The refractive index of $Ge_{1-x}Si_x$ can be interpolated as $n_r(Ge_{1-x}Si_x)$=4.10-0.64x [104]. For x<0.02 the effective masses of electrons and holes of $Ge_{1-x}Si_x$ is indistinguishable from those of pure Ge from the experimental reports so far [105]. Therefore we just use the effective masses of pure Ge in our modeling. The transition matrix element parameter of the direct gap of $Ge_{1-x}Si_x$ alloy is not reported in literature. However, from k·p theory we have [106]:

$$\frac{m_0}{m_e(\Gamma)} = -1 + \frac{E_p}{3}\left(\frac{1}{E_g^{\Gamma}(lh)} + \frac{1}{E_g^{\Gamma}(hh)} + \frac{1}{E_g^{\Gamma}(so)}\right) = -1 + \frac{E_P}{3\overline{E_g^{\Gamma}}}, \tag{4.18}$$

where $m_e(\Gamma)$ is the electron effective mass at Γ valley, $E_g^{\Gamma}(so)$ is the energy gap of the split-off band, and

$$\frac{1}{\overline{E_g^{\Gamma}}} = \frac{1}{E_g^{\Gamma}(lh)} + \frac{1}{E_g^{\Gamma}(hh)} + \frac{1}{E_g^{\Gamma}(so)}. \tag{4.19}$$

Rearranging the equation we get

$$E_p = 3\overline{E_g^{\Gamma}}\left(\frac{m_0}{m_e(\Gamma)}+1\right). \tag{4.20}$$

This equation has been shown to agree fairly well with the experimental results of most group IV and III-V semiconductor materials [106]. Since the electron effective mass $m_e(\Gamma)$ of $Ge_{1-x}Si_x$ is nearly the same as pure Ge when x<0.02 and we can calculate $\overline{E_g^{\Gamma}}(Ge_{1-x}Si_x)$ as a function of Si composition and strain, $E_p(Ge_{1-x}Si_x)$ can also be easily obtained.

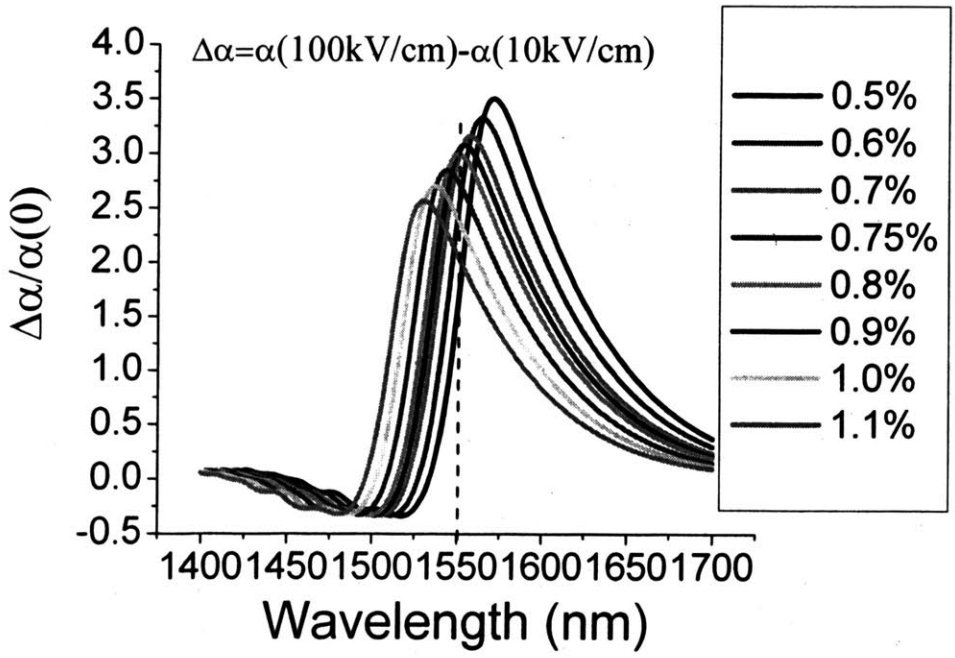

Fig. 4. 6. $\Delta\alpha/\alpha_{on}$ as a function of wavelength for different Si compositions assuming an applied electric field of 100 kV/cm at optical "off" state and 10 kV/cm built-in electric field under 0 bias at optical "on" state.

Now that we have obtain all the material parameters required in Eq. 4.13, we can model the FK effect in dilute Si-doped, 0.2% tensile strained $Ge_{1-x}Si_x$ alloy (x<0.02). Fig.

4.6 plots $\Delta\alpha/\alpha_{on}$ as a function of wavelength for different Si compositions assuming an applied electric field of 100 kV/cm at optical "off" state, and a built-in electric field of 10 kV/cm under 0 bias at optical "on" state due to the *p-i-n* diode structure. By increasing the Si composition from 0.5% to 1.1%, the optimal operating wavelength (i.e., the wavelength at which $\Delta\alpha/\alpha_{on}$ is maximized) shifts from 1570 to 1530nm. The magnitude of the peak $\Delta\alpha/\alpha_{on}$ decreases with the increase of Si content. This is because the addition of Si increases the difference between the direct and indirect band gaps and the material is more and more like an indirect band gap material. Therefore, the indirect gap absorption becomes more dominant and the influence of the FK effect of the direct gap on the absorption coefficient change is reduced.

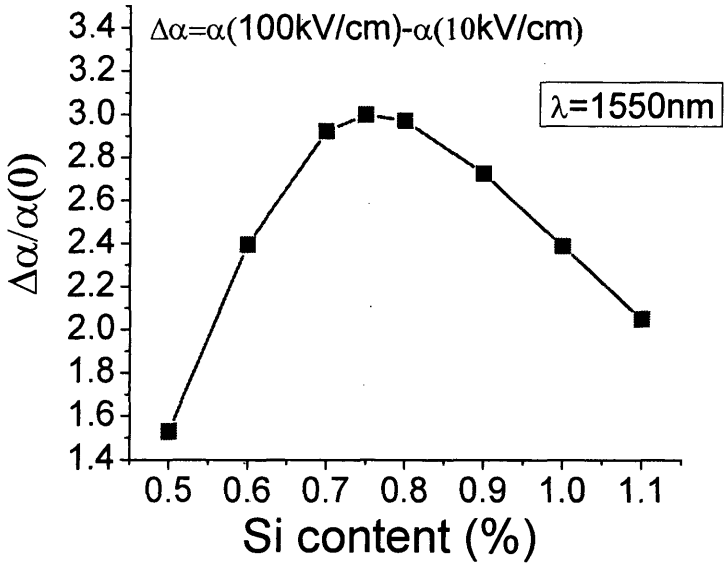

Fig. 4. 7 $\Delta\alpha/\alpha_{on}$ at 1550 nm vs. Si composition assuming an applied electric field of 100 kV/cm at optical "off" state and 10 kV/cm built-in electric field under 0 bias at optical "on" state.

As we are most interested in the performance around 1550nm, Fig. 4.7 plots $\Delta\alpha/\alpha_{on}$ at 1550 nm vs. Si composition in the 0.2% tensile strained $Ge_{1-x}Si_x$ alloy. It was found that a Si composition of 0.7-0.8% is optimal for maximum $\Delta\alpha/\alpha_{on}$ at 1550nm.

The peak $\Delta\alpha/\alpha_{on}$ value is ~3.0. Therefore, we can achieve ~12 dB extinction ratio at a cost of ~4 dB insertion loss with an electric field of 100 kV/cm at optical "off" state if the coupling loss can be engineered to be much smaller than the material absorption loss. It is also interesting to know the absolute value of the absorption coefficient of the material at 1550 nm, since it determines how long the device should be. Fig. 4.8 plots the absorption coefficient at 1550 nm vs. electric field for x=0.75%, an optimal composition for operation at 1550 nm. At 0 electric field the absorption coefficient is calculated to be ~125/cm. As a result, the length of the device should not exceed 70 μm for <4 dB insertion loss. The breakdown electric field of Ge is ~130 kV/cm. At this electric field an absorption coefficient of 720/cm can be achieved at 1550 nm. Therefore, the maximum possible $\Delta\alpha/\alpha_{on}$ at 1550nm that can be achieved before the material breaks down is around 4.7. One may not want to apply such a high electric field in the real application, though, since it may deteriorate the lifetime of the device. In our design we assume a maximum applied electric field of 100 kV/cm instead of 130 kV/cm.

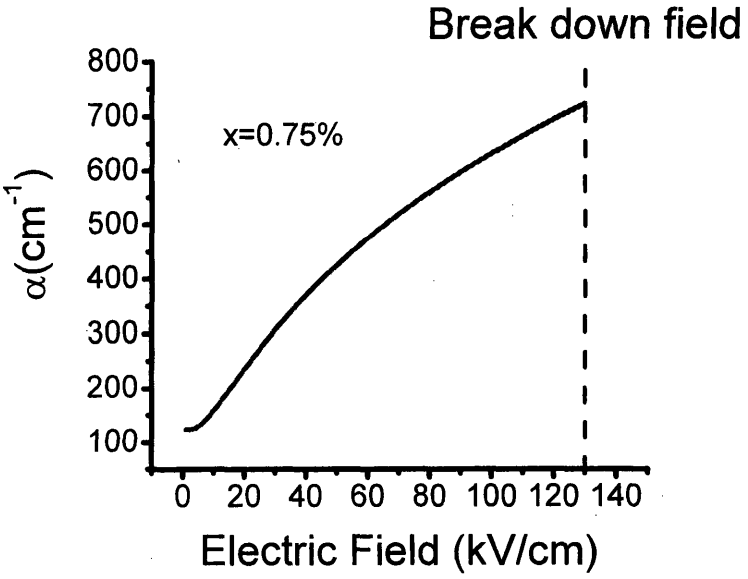

Fig. 4. 8 Absorption coefficient at 1550 nm vs. electric field for x=0.75% in $Ge_{1-x}Si_x$.

It is interesting to note that the same $Ge_{0.9925}Si_{0.0075}$ material can also be used for photodetector at 1550 nm. For example, with 100 kV/cm electric field the absorption coefficient of the material is 632/cm, and with a length of 25 μm 80% internal quantum efficiency can be achieved at 1550 nm. The advantage of using the same material for EA modulator and photodetector is that the material can be deposited at the same time. This saves the trouble of deposition one material for one device, covering the device area, and doing another deposition to fabricate the other kind of device. Therefore, when we refer to $Ge_{1-x}Si_x$ in the later text, the composition is x=0.75% by default for both the EA modulator and the photodetector.

4.2 Waveguide-Modulator Coupling Design

As discussed in the previous section, the length of the $Ge_{0.9925}Si_{0.075}$ EA modulator cannot exceed 70 μm for <4 dB loss due to the indirect band gap absorption of the material. Obviously, it cannot be used as a waveguide material globally on the chip since the length of global waveguides is in the order of cm. For small bending loss and high packing density, high index contrast Si(core, refractive index n_r =3.48)/SiO_2(cladding, n_r=1.46) waveguides are the most attractive candidates in EPIC chips. For simplicity we will call this kind of waveguide the "Si waveguide" in the later text. To decrease the insertion loss, we need to find some ways to couple light efficiently from the input Si waveguide to the $Ge_{1-x}Si_x$ (x=0.75%) EA modulator and then to the output Si waveguide. In this section two coupling schemes are proposed: (1) butt-coupling and (2) side coupling with tapered structures. The former one is more straight forward but has some coupling loss due to the mode mismatch between the Si/SiO_2

waveguide and the $Ge_{1-x}Si_x$ (x=0.75%) modulator. To our knowledge, this is the first example of butt-coupling design in high index contrast system. The second one can achieve exact mode match and maximum coupling efficiency, but the fabrication is much more difficult since the tip radius of the taper has to be <80nm. Such sharp tapered structure requires expensive lithography and etching tools. Now we discuss about these two coupling schemes in detail.

4.2.1 Butt-coupling between the Si Waveguide and the $Ge_{0.9925}Si_{0.0075}$ EA Modulator

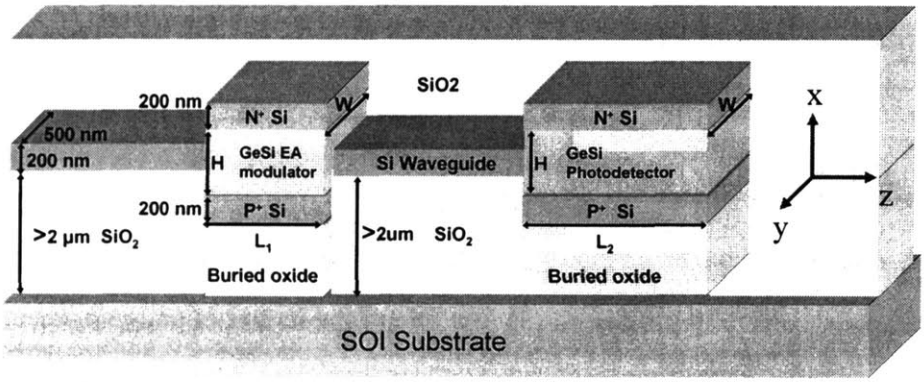

Fig. 4.9 Schematic drawing of the butt-coupling structure between the Si/SiO_2 waveguide and the $Ge_{1-x}Si_x$ (x=0.75%) EA modulator.

Fig. 4.9 schematically shows the butt-coupling structure between the Si waveguide and the $Ge_{1-x}Si_x$ (x=0.75%) EA modulator. The >2 μm SiO_2 under-cladding of the Si waveguide is used to prevent the light in the Si waveguide from leaking to the Si substrate. The idea of butt-coupling is very simple: to align the center of the waveguide to that of the modulator, just like connecting two pipes together. To achieve optimal coupling, though, the cross-sectional dimensions (W and H in Fig. 4.9) of the modulator have to match those of the Si waveguide such that the mode in the modulator has the maximum overlap with that in the Si waveguide. The Si waveguide is usually chosen to

be 500 nm wide and 200 nm high [107,108]. The reason for such a choice is that the width of the waveguide has to be defined by lithography and features narrower than 500 nm is hard to achieve with the optical lithography tools in MIT. Therefore, a width of 500 nm is chosen for the Si waveguide. Once the width is determined, the height has to be small enough so that the waveguide supports only one mode. Therefore, a cross-sectional dimension of 500×200 nm is chosen for the Si waveguide.

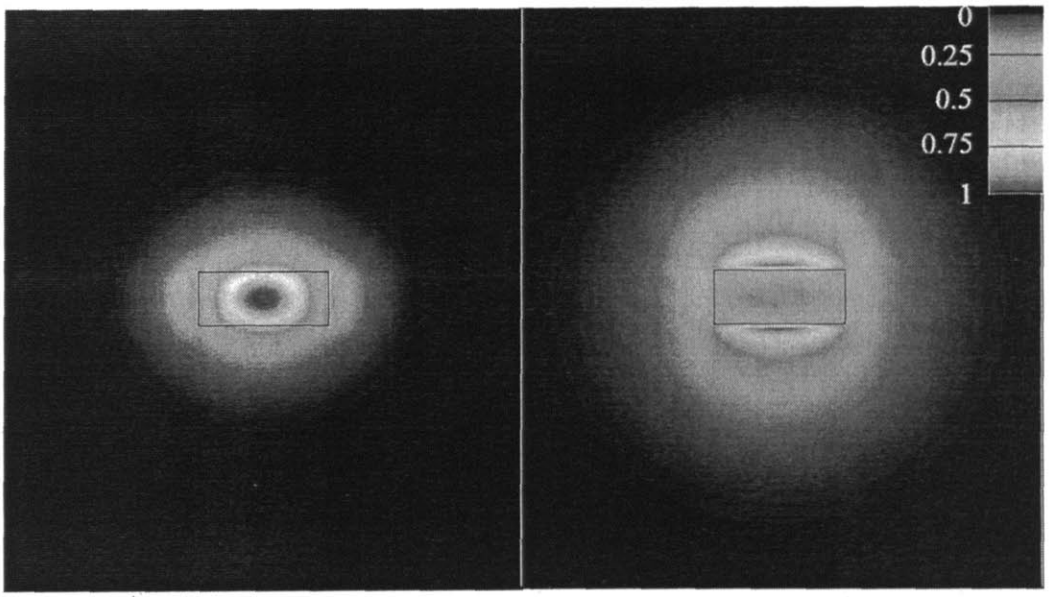

Fig. 4.10 TE and TM mode profiles of a 500×200 nm Si waveguide (with SiO_2 cladding).

Fig. 4.10 shows the fundamental TE and TM modes of a 500×200 nm Si waveguide with 2 μm under-cladding SiO_2 on a Si substrate at a wavelength of 1550 nm. The mode profile was solved with *Apollo Photonics Solution Suite Ver. 2.3* [109]. We will call this cross-sectional plane "x-y" plane in the later text, while z direction refers to the light propagation direction. The boxes in the figure indicate the position of the Si waveguide core. Here TE mode means the electric field polarization is parallel to the

surface of the substrate, while TM mode means the electric field polarization is perpendicular to the substrate. The TE mode has an effective index of 2.443 and a confinement factor of 0.825 (i.e., the fraction of power that is confined in the Si core). The TM mode, on the other hand, has an effective index of 1.737 and a confinement factor of 0.524. Since the TE mode has a much larger confinement factor, the bending loss is much lower than that of the TM mode. For example, with 2 μm bending radius the bending loss of TE and TM modes are calculated to be 2.1 dB/mm and 1346 dB/mm, respectively. Therefore, for microphotonic applications TE mode of the Si waveguide is preferred for higher packing density. In the later text we will focus on the mode overlapping between the TE modes of the Si waveguide and the SiGe EA modulator.

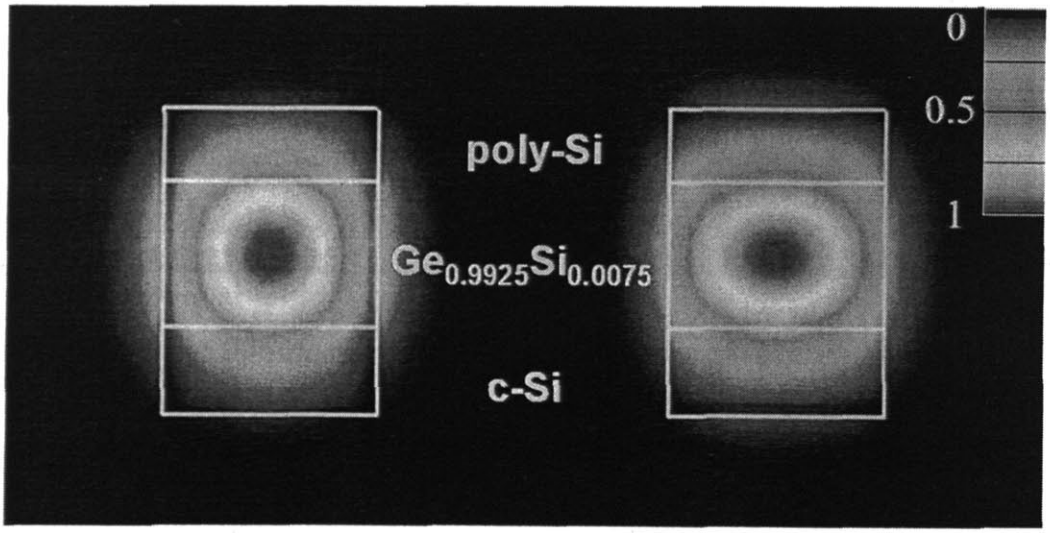

Fig. 4.11 TE and TM modes of $Ge_{1-x}Si_x$ (x=0.75%) EA modulator with H=400 nm, W=600 nm (see Fig. 4.9) for the device structure.

As an example, Fig. 4. 11 shows the fundamental TE and TM modes of the $Ge_{1-x}Si_x$ (x=0.75%) EA modulator assuming the incident wavelength $\lambda = 1550\,\text{nm}$, $Ge_{1-x}Si_x$

height H=400 nm, $Ge_{1-x}Si_x$ width W=600 nm, upper poly Si thickness=200nm, lower crystalline Si thickness=200 nm (SOI substrate), and SiO_2 under-cladding thickness=2 μm. The material absorption of the structure has to be taken into account in order to evaluate the device performance as an EA modulator. In coupling efficiency calculation, absorption information is also needed to calculate the reflection between the Si waveguide and $Ge_{1-x}Si_x$ (x=0.75%) EA modulator correctly. Assuming 0 V bias at optical "on" state and 3.3 V reverse bias at optical "off-state" (the maximum DC bias allowed for <180 nm CMOS technology), the $Ge_{1-x}Si_x$ (x=0.75%) absorption coefficients are determined to be 158/cm and 624/cm, respectively, with FK theory described in the previous section. We also assume an n^+ doping of $2\times10^{19}/cm^3$ in the top poly-Si layer and a p^+ doping of $2\times10^{19}/cm^3$ in the bottom c-Si layer in the p-i-n diode structure. The free carrier absorption in Si is given by [110]

$$\alpha_f = 2.6\times10^{-27} n_e \lambda^3 + 2.7\times10^{-24} p_h \lambda^2, \tag{4.21}$$

where n_e and p_h are the electron and hole densities in terms of cm^{-3}, and λ is the wavelength in terms of nm. With this equation we calculate a free carrier absorption of 193 and 130/cm in the top and bottom Si layers, respectively. In the simulation the absorption coefficients are converted into the imaginary part of the refractive index by

$$n_i = (\alpha\lambda)/4\pi, \tag{4.22}$$

where α is the absorption coefficient and n_i is the imaginary part of the refractive index. The simulation shows that TE mode has a real effective index of 3.710 and a confinement factor of 0.886 (i.e., the fraction of optical power confined in the $Ge_{1-x}Si_x$ core), while the TM mode has an effective index of 3.728 and a confinement factor of 0.881. Note that the confinement factor of the $Ge_{1-x}Si_x$ (x=0.75%) EA modulator is an important

parameter in its design, since only the light confined in the $Ge_{1-x}Si_x$ (x=0.75%) material can be modulated. Ideally we would like a confinement factor as close to 1 as possible. The imaginary parts of the effective refractive indices ($n_{eff,i}$) are both 0.00210 for TE mode TM modes at 0V bias, equivalent to a modal absorption coefficient (α_{mod}) of 170/cm.

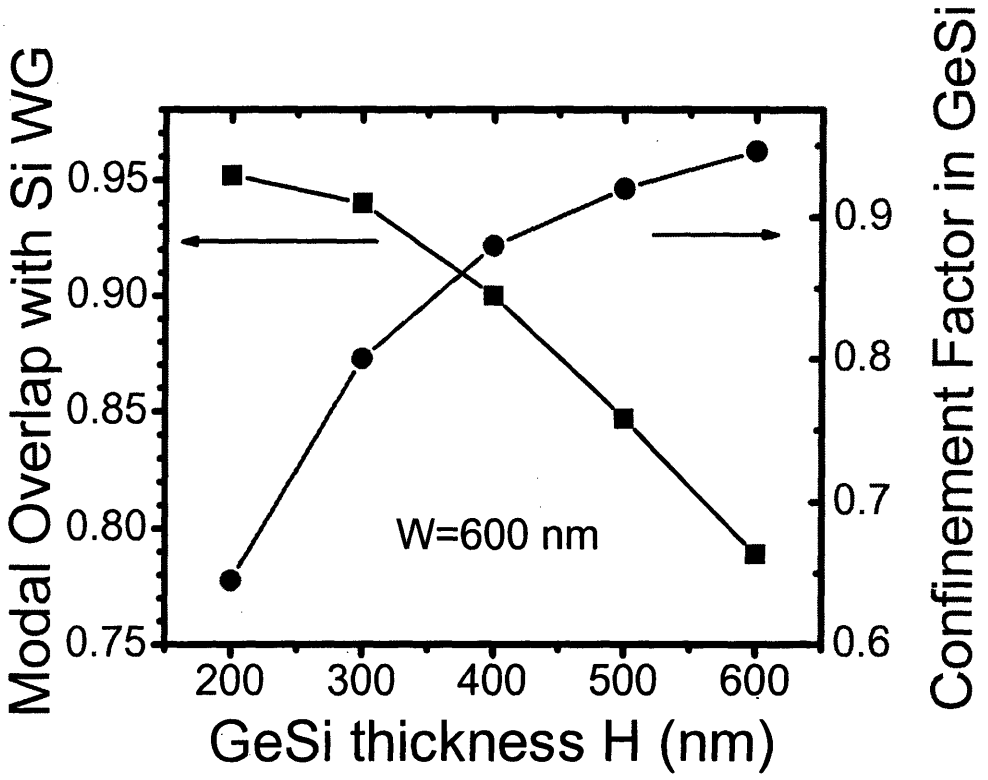

Fig. 4.12 modal overlap between the $Ge_{1-x}Si_x$ (x=0.75%) EA modulator and the Si waveguide for different $Ge_{1-x}Si_x$ thickness (H), keeping the width (W) at 600 nm

At 3.3 V reverse bias $n_{eff,i}$ is 0.00767 for the TE mode and 0.00733 for TM mode, corresponding to an α_{mod} of 622/cm and 594/cm, respectively. The reason why the TM mode shows a slightly less modal absorption at 3.3V bias is that a little less light is confined in the high absorption $Ge_{1-x}Si_x$ (x=0.75%) material compared to TE. The

overlap between the TE modes of the $Ge_{1-x}Si_x$ (x=0.75%) modulator and the Si waveguide is calculated to be 0.902 when the centers of the Si core and the $Ge_{1-x}Si_x$ (x=0.75%) core are aligned. The mode overlap describes the coupling efficiency in the x-y plane. Therefore, the higher the modal overlap, the higher the coupling efficiency. Fig. 4.12 shows the modal overlap between the $Ge_{1-x}Si_x$ (x=0.75%) EA modulator and the Si waveguide for different $Ge_{1-x}Si_x$ (x=0.75%) thickness (H), keeping the width (W) at 600 nm. The mode overlap increases from 0.789 to 0.952 as the $Ge_{1-x}Si_x$ (x=0.75%) thickness decreases from 600 to 200 nm. Therefore, it seems that a thinner $Ge_{1-x}Si_x$ (x=0.75%) layer is preferred from a coupling point of view.

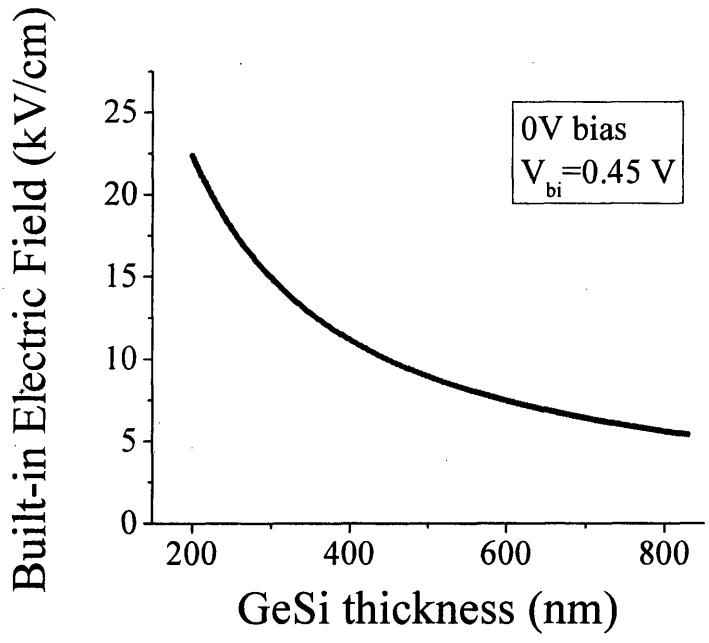

Fig. 4.13. Built-in electric field in the $Ge_{1-x}Si_x$ (x=0.75%) layer as a function of thickness. The built-in voltage V_{bi}~0.45V

However, if we consider the whole device performance thinner $Ge_{1-x}Si_x$ (x=0.75%) layer also has two disadvantages: (1) The confinement factor is decreased, meaning less light is confined in the active $Ge_{1-x}Si_x$ (x=0.75%) layer so that a less fraction of the

optical power is modulated. As we can see from the right hand axis of Fig. 4.12, the confinement factor of the TE mode decreases from 0.926 to 0.625 as the height of $Ge_{1-x}Si_x$ (x=0.75%) decrease from 600 to 200 nm. This would decrease the extinction ratio of the device. (2) The built-in electric field in the $Ge_{1-x}Si_x$ (x=0.75%) material increases at 0 V bias. Fig. 4.13 shows the built-in electric field in the intrinsic $Ge_{1-x}Si_x$ (x=0.75%) material at 0 bias as a function of layer thickness. The built-in voltage V_{bi}~0.45V. As the $Ge_{1-x}Si_x$ (x=0.75%) thickness decreases from 600 to 200 nm, the built-in electric field at 0 V bias increases from 7.5 to 22.5 kV/cm. From Fig. 4.8 we can find out that the absorption coefficient increases from 140/cm to 254/cm correspondingly. These are the absorption coefficients at the optical "on" state and are directly related to the insertion loss. Assuming 100 kV/cm electric field in the optical "off" state (which is almost the maximum electric field that can be applied on Ge before it breaks down), we have α_{off}=632/cm. So $\Delta\alpha/\alpha_{on}$ decreases from 3.5 to 1.5 as the $Ge_{1-x}Si_x$ (x=0.75%) thickness decrease from 600 to 200 nm. Therefore, the extinction ratio will decrease when the $Ge_{1-x}Si_x$ (x=0.75%) layer gets too thin. From the above discussions we learn that for optimal design of the whole $Ge_{1-x}Si_x$ (x=0.75%) modulator device we have to trade off between different parameters. As we mainly focus on the description of coupling scheme in this section, we will discuss the overall optimization of the modulator dimension in more detail in the next section.

To derive the total coupling loss, one also has to consider the reflection in the z direction (propagation direction) in addition to the mode overlap in the x-y plane. This can be achieved by propagation matrix element method, using the effective refractive indices of the Si waveguide and $Ge_{1-x}Si_x$ (x=0.75%) EA modulator obtained from mode

solving. This is because the effective index n_{eff} describes the effective phase delay of the light in the waveguide, and the propagation constant is related to n_{eff} by $\beta = \frac{2\pi n_{eff}}{\lambda_0}$, where λ_0 is the wavelength in vacuum. Therefore, the light in the waveguide travels as if it is in a homogenous media with a refractive index of n_{eff}, and we can use this parameter to derive the refection/transmission at the interface of the Si waveguide and the $Ge_{1-x}Si_x$ (x=0.75%) EA modulator.

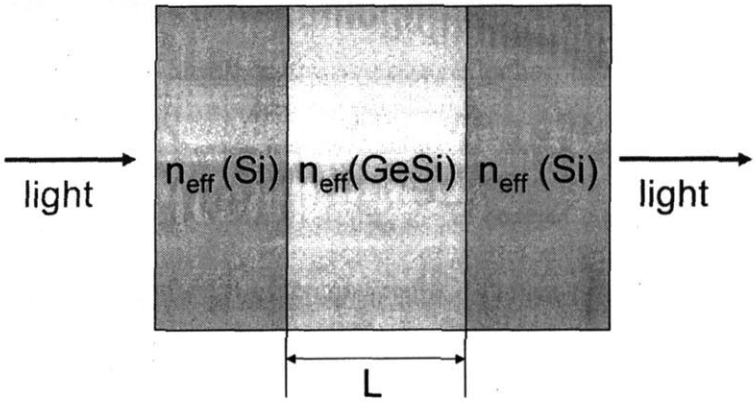

Fig. 4.14 Schematic diagram showing the equivalent structure for reflection/transmission calculation in the z-direction

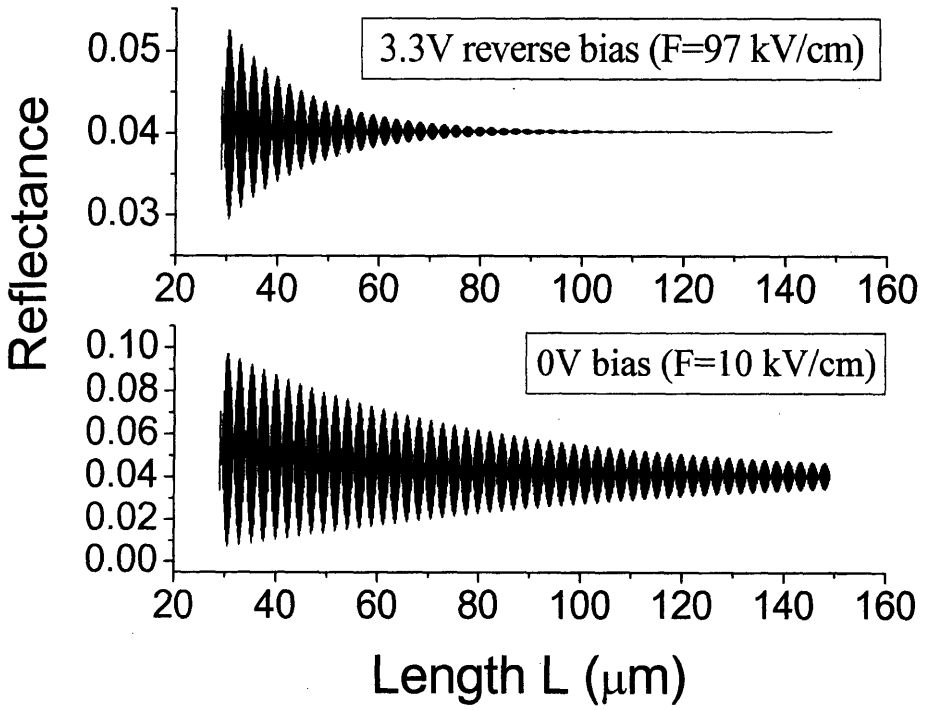

Fig. 4.15 Reflectance vs. $Ge_{1-x}Si_x$ (x=0.75%) modulator length in the propagation direction of the waveguide

Fig. 4. 14 schematically shows the equivalent structure for reflection calculation in the z-direction. The effective indices can be obtained from mode calculations, like the ones shown in Fig. 4. 10 and Fig. 4. 11. Since the propagation matrix element method is rather simple and widely used in reflection/transmission calculation of multilayered structures, we will not discuss about it in detail here. Readers can refer to Ref [111] for more details. Fig. 4.15 shows the reflectance of 1550 nm light in the z direction as a function of the length (L) of the $Ge_{1-x}Si_x$ (x=0.75%) EA modulator at 0V and 3.3 V reverse bias, assuming W=600 nm, H=400 nm, and the length of input and output Si waveguides is 2 mm. Oscillations due to interference effect is clearly seen in the figure, especially for L<50 μm. As the modulator length or the absorption coefficient increases, the oscillation damps down since the reflected power at the interface of the modulator

and the output Si waveguide decreases due to more absorption loss in the modulator. As a result, its interference effect also decreases. In the case of 3.3 V reverse bias, as the length increases above 100 μm the reflectance converges at 0.0424. This number is exactly the reflectance at the input waveguide/$Ge_{1-x}Si_x$ (x=0.75%) modulator interface assuming $Ge_{1-x}Si_x$ (x=0.75%) is infinitely long ($r=(3.710-2.443)^2/((3.710+2.443)^2=0.0424$). This is because almost all the light is absorbed when it reaches the interface between the $Ge_{1-x}Si_x$ (x=0.75%) modulator and the output waveguide, so it does not see this interface anymore. The average reflectance is 0.0435 and 0.0403 for 0 V and 3.3 V reverse bias, respectively. Therefore, the average reflection loss is only ~0.2 dB.

The total coupling loss is a sum of the modal overlap loss in the x-y plane and the reflection loss in the z direction. For example, in the case of coupling the Si waveguide to a 600×400 nm $Ge_{1-x}Si_x$ (x=0.75%) EA modulator, the mode overlap loss in the x-y plane is $-10\log_{10}(0.902^2)=0.9$ dB. The average refection loss is ~0.2 dB, as mentioned previously. Therefore, the total coupling loss is ~1.1 dB in this case. When the thickness of the $Ge_{1-x}Si_x$ (x=0.75%) layer decreases to 200 nm the mode overlap loss and average reflection loss are 0.43 dB and 0.13 dB, respectively, and the total coupling loss is only 0.56 dB.

From the simulations and discussion above, we find that with butt-coupling scheme ~1 dB coupling loss is achievable. The largest modal overlap that can be obtained between the $Ge_{1-x}Si_x$ (x=0.75%) EA modulator and the Si waveguide is ~0.96, and average reflection can be decreased to ~0.03 with adequate modulator length. Therefore, the minimum coupling loss achievable is ~0.49 dB with butt coupling scheme.

4.2.2 Tapered Side-coupling between the Si Waveguide and the $Ge_{0.9925}Si_{0.0075}$ EA Modulator

Tapers are commonly used in photonic devices to decrease the coupling loss between two different waveguide materials [112, 113]. When the light travels toward the tip of the taper, the mode expands because the dimension of the high index core material decreases. If the taper angle is small enough so that this process happens gradually, then there is no loss as the light propagates along the taper. This is called an "adiabatic taper". If we design tapers of two waveguides adequately and put the two tapers in close proximity at an adequate relative position, then at some point along the tapers the mode profile in the first taper is almost identical to that in the second taper. At this point the light can resonantly couple into the second taper with a very high coupling efficiency. Our tapered side-coupling between the Si waveguide and the $Ge_{1-x}Si_x$ (x=0.75%) EA modulator is based on such a principle.

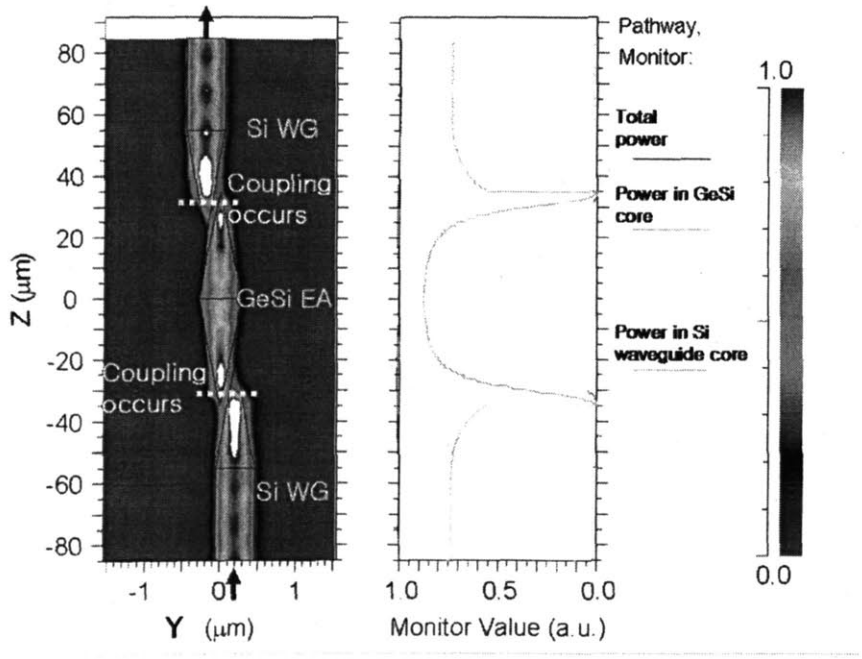

Fig. 4.16 A simulation of tapered side-coupling between Si/SiO_2 waveguide and $Ge_{1-x}Si_x$ (x=0.75%) EA modulator with nearly 0 coupling loss.

Fig. 4. 16 shows the top view of a simulation of our side coupling design for TE polarization by the Beam Propagation Method (BPM) [114]. The simulation was performed with Rsoft BeamPROP software suite [115]. The $Ge_{1-x}Si_x$ (x=0.75%) thickness is 400 nm, and the cross-section of the Si waveguide is still 500×200 nm. The centers of the $Ge_{1-x}Si_x$ (x=0.75%) core and Si waveguide core are of the same height. Basically, the $Ge_{1-x}Si_x$ (x=0.75%) and Si waveguide structure are the same as the butt coupling case, except for the tapered structures and the side coupling scheme. To single out the coupling efficiency, we set the absorption coefficient of $Ge_{1-x}Si_x$ (x=0.75%) to 0 in the simulation so that we do not see the absorption loss. The $Ge_{1-x}Si_x$ (x=0.75%) modulator is now consisted of two tapered parts, coupling to the tapered input and output Si waveguides, respectively. The coupling points are clearly seen in the figure, indicated by the light yellow dashed lines in the figure. By monitoring the total power of the light propagating along the structures, we found nearly 0 coupling loss. To double check this result, we also calculate the modal overlap between the Si waveguide and $Ge_{1-x}Si_x$ (x=0.75%) EA modulator at the coupling point. As the light propagates in the taper, it gradually transforms from TE into TM mode due to the gradual change in the geometric shape of the cross-section. At the coupling point the cross-section of the $Ge_{1-x}Si_x$ (x=0.75%) modulator is 59×400 nm, while that of the Si waveguide is 169×200nm. The overlap integral between the TM modes of the Si waveguide and $Ge_{1-x}Si_x$ (x=0.75%) modulator at the coupling point is as high as 0.9999. Therefore, the light resonantly couples from the input Si waveguide into the $Ge_{1-x}Si_x$ (x=0.75%) modulator with nearly 0 coupling loss. After the light is modulated in the $Ge_{1-x}Si_x$ (x=0.75%) modulator and coupled back to the output Si waveguide, the polarization gradually changes back to TE

again in the taper due to the gradual change in the cross-section of Si waveguide. This way, a modulator with nearly 0 coupling loss can be achieved theoretically.

Despite of its intrinsic advantage in terms of physics, one should note that such a structure is hard to fabricate in reality. At the coupling point the $Ge_{1-x}Si_x$ (x=0.75%) modulator taper width is only 59 nm, and the horizontal gap between the Si waveguide taper and the $Ge_{1-x}Si_x$ (x=0.75%) modulator is only 100 nm. This requires nanoscale lithography tools, which is not widely available. Therefore, despite the intrinsic advantage of using tapered structure, from a device fabrication point of view the butt coupling is much easier to achieve.

4. 3 Overall Device Design of Waveguide-coupled $Ge_{0.9925}Si_{0.0075}$ EA Modulator and Photodetectors

4.3.1 Device Design of Waveguide-coupled $Ge_{0.9925}Si_{0.0075}$ EA Modulators

As we mentioned in the previous section, overall device design of the modulator requires considerations of all the relevant parameters like mode overlap, reflection, confinement factor, and relative change in absorption coefficient after an electric field is applied. Trade-off among these parameters is needed to achieve the optimal overall performance. In this section we will discuss about the overall design in detail. The aim is, again, to maximize the extinction ratio and minimize the insertion loss. For convenience we will use dB as the unit for both extinction ratio and insertion loss in the later text.

In the modulator device the insertion loss is composed of two parts: the absorption loss at 0 V bias $\kappa_a(0)$ and the coupling loss κ_c. The absorption loss is given by

$$\kappa_a(0) = -10\lg_{10}\left(e^{-\alpha_{\mathrm{mod}}(0)L}\right) = 4.343\alpha_{\mathrm{mod}}(0)L, \tag{4.23}$$

where $\alpha_{\mathrm{mod}}(0)$ is the modal absorption coefficient of the $Ge_{1-x}Si_x$ (x=0.75%) modulator at 1550 nm under 0 V bias. This parameter can be derived from the imaginary effective index $n_{eff.i}$ of the modulator. It is related to the absorption coefficients of $Ge_{1-x}Si_x$ (x=0.75%) (α_{GeSi}), n^+ poly Si (α_{n-Si}) and p^+ c-Si materials (α_{p-Si}) as well as the fraction of power confined in these materials (Γ_{GeSi}, Γ_{n-Si} and Γ_{p-Si})

The coupling loss is given by

$$\kappa_c = -10\lg_{10}\left((1-r)\Omega^2{}_{GeSi,Si}\right), \tag{4.24}$$

where $\Omega_{GeSi.Si}$ is the modal overlap between the $Ge_{1-x}Si_x$ (x=0.75%) EA modulator and the Si waveguide in the x-y plane, and r is the reflectance in the z direction. The total insertion loss is just $\kappa_a(0)+\kappa_c$.

The extinction ratio is equal to $(\kappa_a(V)+\kappa_c)-(\kappa_a(0)+\kappa_c)=\kappa_a(V)-\kappa_a(0)$, where

$$\kappa_a(V) = -10\lg_{10}\left(e^{-\alpha_{\mathrm{mod}}(V)L}\right) = 4.343\alpha_{\mathrm{mod}}(V)L \tag{4.25}$$

is the absorption loss when a reverse bias V is applied on the modulator, and $\alpha_{\mathrm{mod}}(V)$ is the modal absorption coefficient of the $Ge_{1-x}Si_x$ (x=0.75%) modulator at 1550 nm under a reverse bias of V. Therefore, our basic figure of merit (FOM) is:

$$FOM = \frac{Extinction\ \ Ratio}{Insertion\ \ loss} = \frac{\kappa_a(V)-\kappa_a(0)}{\kappa_a(0)+\kappa_c} = \frac{\Delta\alpha_{\mathrm{mod}}}{\alpha_{\mathrm{mod}}(0)+0.23026\kappa_c/L}, \tag{4.26}$$

where $\Delta\alpha_{mod} = \alpha_{mod}(V) - \alpha_{mod}(0)$. Now we can see that the parameters that determine the basic FOM are: the modal absorption coefficients $\alpha_{mod}(0)$ and $\alpha_{mod}(V)$, the modal overlap in the x-y plane ($\Omega_{GeSi,Si}$), and the reflectance r in the z direction. The modal absorption coefficients are related to the absorption coefficients of $Ge_{1-x}Si_x$ (x=0.75%) (α_{GeSi}), n^+ poly Si (α_{n-Si}) and p^+ c-Si materials (α_{p-Si}) as well as the confinement in these materials (Γ_{GeSi}, Γ_{n-Si} and Γ_{p-Si}). Note that the α_{GeSi} is not only related to the material properties, but also the thickness (H) of the $Ge_{1-x}Si_x$ (x=0.75%) layer because the electric field in this layer is determined by both the reverse bias and the thickness. The absorption in n^+ and p^+ Si is determined by the doping level. Confinement factors and modal overlap $\Omega_{GeSi,Si}$ are determined by the cross-section (H and W) of the $Ge_{1-x}Si_x$ (x=0.75%) as well as those of n^+ and p^+ Si, while r is related to all the three dimensions (L, H and W) of $Ge_{1-x}Si_x$ (x=0.75%) EA modulator. It is interesting to see that the $Ge_{1-x}Si_x$ (x=0.75%) thickness has influence on all the parameters that determine the extinction ratio and insertion loss. Therefore, it has the most influence on the final result.

To simulate the performance of the whole device, we can adopt two ways of simulation: (1) Mode solving method. Use an optical mode solver to obtain the modal absorption coefficients and the modal overlap in the x-y plane, then calculate the reflection in the z-direction using effective index method. Thus, the insertion loss and extinction ratio can be calculated with Eqs. 4.23-4.26. For example, we have shown in section 4.2.1 that a $Ge_{1-x}Si_x$ modulator with a cross-section of 600×400 nm has modal absorption coefficients of $\alpha_{mod}(0)$=170/cm, $\alpha_{mod}(3.3V)$ =622/cm, and an average κ_c of 1.1 dB. Here we assume a reverse bias of 3.3 V at the optical "off" state because a

voltage of <3.3V is required in sub 180 nm CMOS technology. Assuming L=50 μm, we obtain an insertion loss of 4.80 dB and an extinction ratio of 9.81 dB. The basic FOM is 9.81/4.80=2.04. (2) BPM simulation plus reflection correction. Use a 3D BPM simulation that takes into account all the parameters except for the reflectance *r* in the z-direction, since BPM method does not calculate reflection in the structure. The reflection loss is, again, calculated by the effective index method described previously, and is added to the final result of BPM simulation to obtain the correct insertion loss and extinction ratio.

Fig. 4. 17 shows an example of a BPM simulation on a 600×400 nm $Ge_{1-x}Si_x$ (x=0.75%) EA modulator with a length of 50 μm. In the simulation the absorption coefficient of $Ge_{1-x}Si_x$ (x=0.75%) material is taken into account by setting a complex refractive index. The doping level in the top and bottom Si layer of the modulator was assumed to be $2\times10^{19}/cm^3$ and the absorption coefficient due to free carrier absorption is taken into account (see section 4.2.1). After correction for the reflection, the result shows an insertion loss of 4.76 dB and an extinction ratio of 9.61 dB. Therefore, the basic FOM is 8.9/4.6=2.02. We can see that the simulation results on the same structure given by these two methods are very similar, and the difference is within 5%.

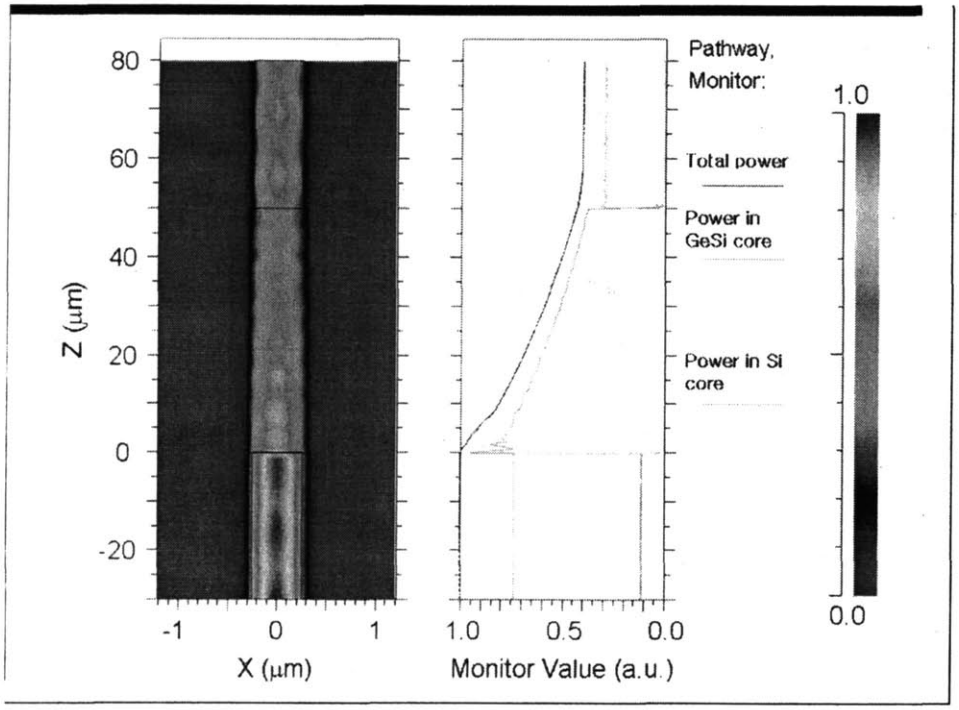

(a) 0V bias, 4.76 dB insertion

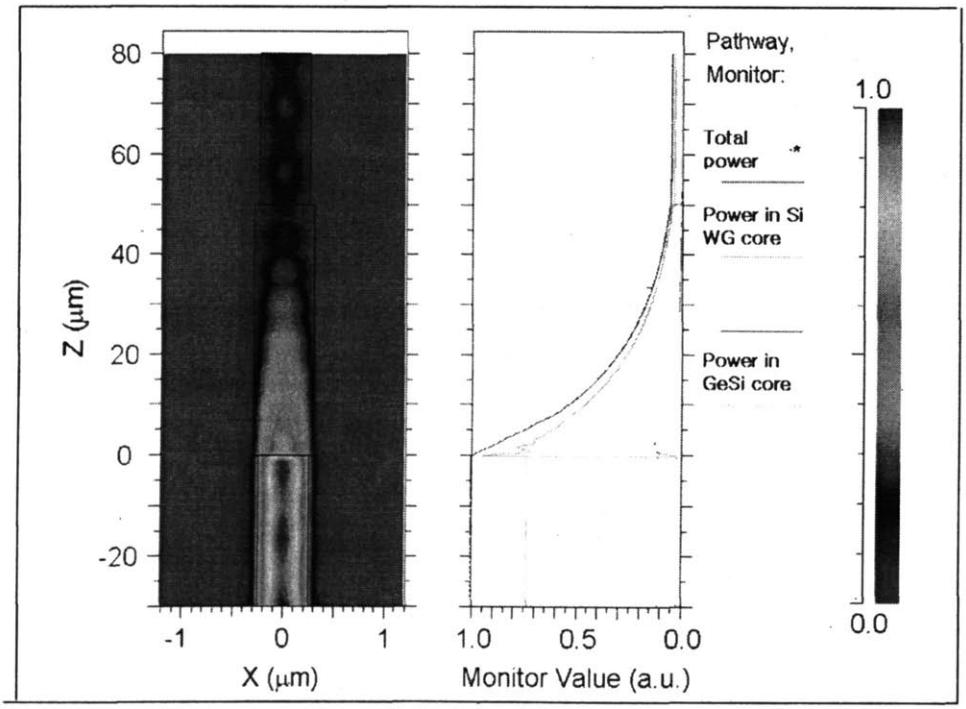

(b) 3.3 V reverse bias, 9.61 dB extinction ratio

Fig. 4.17 Simulation of a butt-coupled, 600×400 nm $Ge_{1-x}Si_x$ (x=0.75%) EA modulator with BPM method. The reflection calculated with effective index method has been added. The results shows 4.76 dB insertion loss and 9.61 dB extinction ratio.

With the two simulation methods described above, the basic FOM (i.e., extinction ratio over insertion loss) of the modulator with different dimensions can be calculated. Fig. 4.18 (a) plots the FOM of 50 μm-long GeSi EA modulator devices with different width (W) and thickness (H) of the GeSi active layer. In this calculation, we specify that the reverse bias applied at the optical off-state of the modulator should not exceed 3.3 V to be compatible with 180 nm CMOS technology. Nor should the electric field exceed 100 kV cm^{-1} due to the limit of material breakdown. The optimal GeSi thickness is determined to be ~400 nm. Below this thickness the optical confinement in the GeSi active layer decreases significantly and the extent of optical modulation is reduced. Above this thickness the modal overlap with the Si waveguide in the x-y plane and the electric field at 3.3 V reverse bias both decrease, leading to a higher coupling loss and lower extinction ratio. The optimal width is ~700 nm. However, for H=400 nm the FOM is almost identical for W=600-800 nm. To reduce the capacitance for higher speed and lower power consumption, a narrower device is preferred. Therefore, we choose a dimension of H=400 nm and W=600 nm, and the corresponding FOM is 2.05. To double check the results, Fig. 4.18 (b) compares the simulation results of the mode solving method to the BPM method for W=600 nm and L=50 μm. The two simulation methods agree fairly well with each other, enhancing the validity of the calculated results.

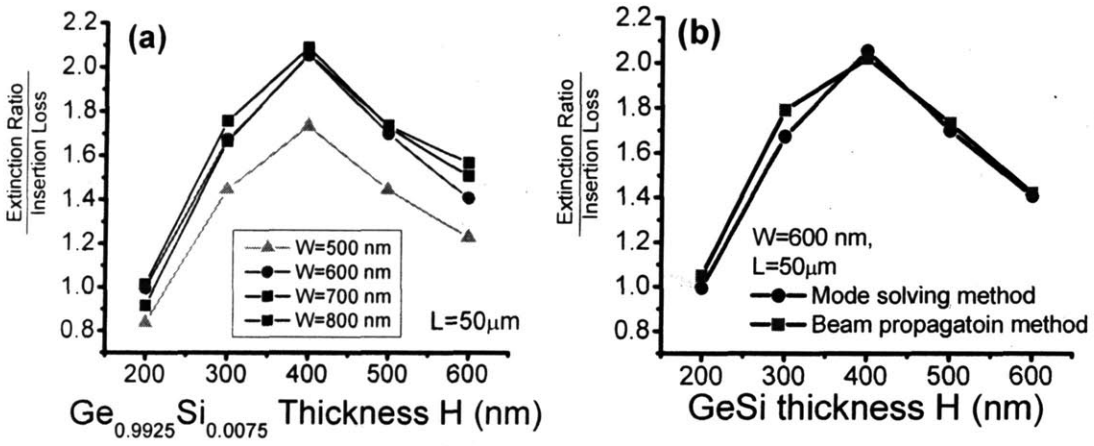

Fig. 4.18 (a) Extinction ratio over insertion loss (basic FOM) of 50 μm-long $Ge_{0.9925}Si_{0.0075}$ EA modulators with different cross-sectional dimensions, and (b) comparison of simulation results by the mode solving method and the BPM method. The two simulation methods agree fairly well with each other.

Fig. 4.19 shows the simulation result of a tapered side coupled structure. Due to nearly 0 coupling loss, a higher basic FOM of 2.6 can be achieved. With 4.0 dB insertion loss, an extinction ratio of 10.4 dB can be obtained. The fabrication of such fine tapers is challenging, though. Judging from the fact that a comparable performance of 9.8 dB extinction ratio at the cost of 4.8 dB insertion loss can still be achieve with butt-coupling, it is more attractive to adopt butt-coupling in real device fabrications.

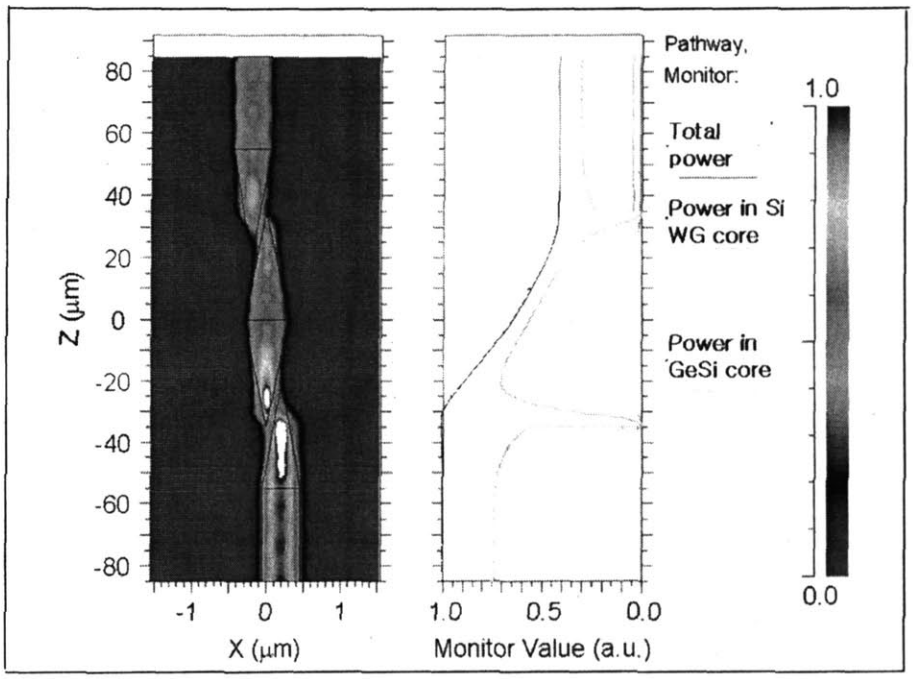

(a) 0V bias, 4.0 dB insertion loss

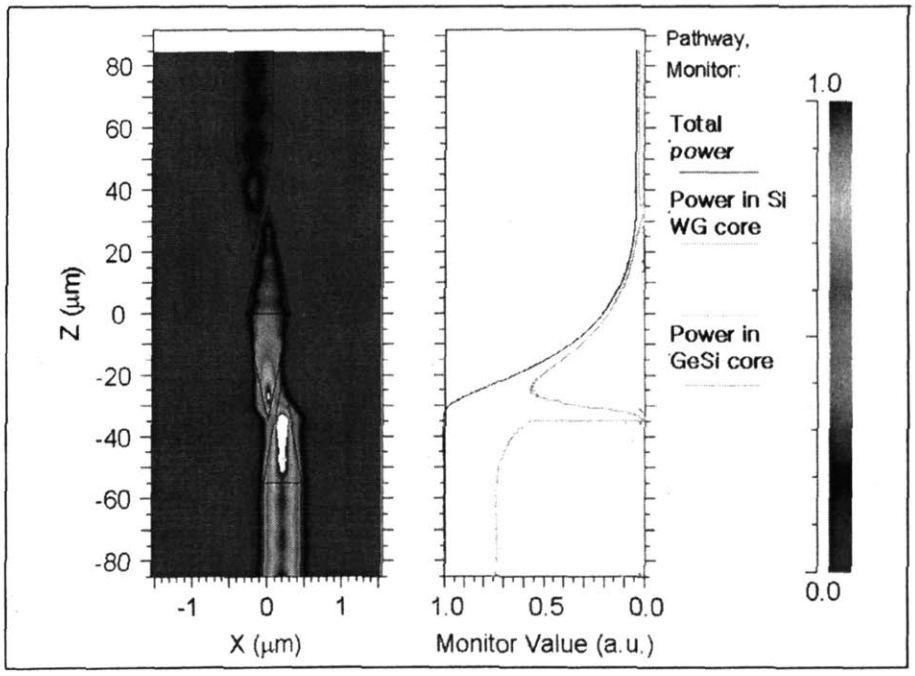

(b) 3.3V bias, 10.4 dB extinction ratio

Fig. 4.19 Simulation of a tapered side-coupled $Ge_{1-x}Si_x$ (x=0.75%) EA modulator with BPM method. The results shows 4.0 dB insertion loss and 10.4 dB extinction ratio.

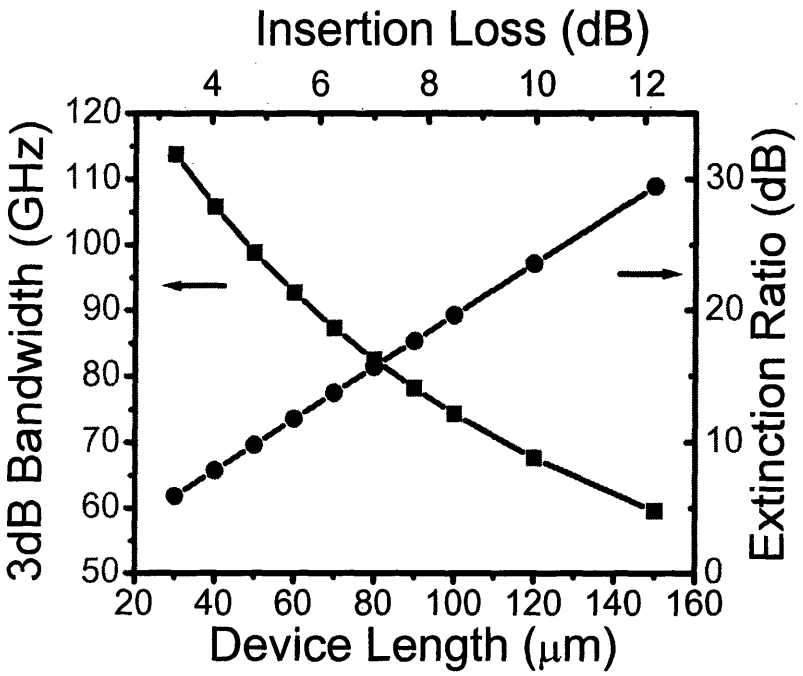

Fig. 4.20 Insertion loss, extinction ratio and 3dB band width as a function of device length (L) of a $Ge_{1-x}Si_x$ (x=0.75%) EA modulator with H=400 nm and W=600 nm.

Fig. 4.20 plots the bandwidth, extinction ratio and insertion loss as a function of device length for a $Ge_{1-x}Si_x$ EA modulator device with W=600 nm and H=400 nm. As mentioned earlier, the longer the device, the higher the extinction ratio, but also the higher the insertion loss due to indirect gap absorption at 0 bias. We assume 50×50 μm^2 metal contact pads with a vertical distance of 4 μm from the substrate, so the pad capacitance is 21.6 fF. Franz-Keldysh effect itself is a fast transition that takes place in the order of sub-picosecond, as mentioned in Chapter 1. Therefore, the bandwidth is mainly limited by the RC delay of the device. As shown in the figure, with a 50 μm long GeSi modulator we can achieve a high extinction ratio of 10 dB and a 3dB bandwidth of >50 GHz at 5 dB insertion loss. Such performance is comparable to the III-V semiconductor materials currently used in telecommunications [116]. Depending on the

applications, insertion loss and extinction ratio can be adjusted by varying the device length. The size of the metal contact pad can be decreased to further increase the RC-limited bandwidth.

4.3.2 Device Design of Waveguide-coupled $Ge_{0.9925}Si_{0.0075}$ Photodetectors

As mentioned earlier, the EA modulator structure can also be used as a photodetector since photocurrent would be generated in the device when the light travels in $Ge_{1-x}Si_x$. The same coupling scheme used in waveguide-modulator coupling is equally applicable to waveguide-detector coupling. In photodetectors the most important parameter is the external quantum efficiency (EQE). Taking into account the coupling efficiency and the absorption of the $Ge_{1-x}Si_x$ (x=0.75%) material, the EQE is given by

$$EQE = (1-r)\Omega_{Si,GeSi}(1-\exp(-\alpha_{eff,GeSi}(V)L)), \tag{4.27}$$

where $\alpha_{eff,GeSi}(V)$ is the effective absorption coefficient of GeSi in the photodetector structure at a reverse bias of V. Note that $\alpha_{eff,GeSi}(V)$ is different from the material absorption coefficient of GeSi since not all the light is confined in GeSi. To obtain $\alpha_{eff,GeSi}(V)$ we set the imaginary indexes of n^+ and p^+ Si to 0 and calculate the imaginary effective index $n_{i,eff}(V)$ of the detector structure. The mode profile remains the same in this way, and $n_{i,eff}(V)$ is only due to the absorption of $Ge_{0.9925}Si_{0.0075}$. So we have $\alpha_{eff,GeSi}(V) = 4\pi\ n_{i,eff}(V) / \lambda$. The responsivity is related to the external quantum efficiency by:

$$R(A/W) = \frac{\lambda(nm)}{1240} EQE. \tag{4.28}$$

The bandwidth of the detector is determined by both the carrier transit time and the RC delay, as discussed in Chapter 3. Fig. 4.21 plots the responsivity and bandwidth of $Ge_{1-x}Si_x$ (x=0.75%) detectors at 0 V and 3.3V bias. The bias has little effect on the bandwidth, since the electric field in the $Ge_{1-x}Si_x$ (x=0.75%) layer is 10.1 kV/cm even at 0 bias and the carriers are already accelerated to the saturation velocity under such a high electric field [79,80]. The responsivity, on the other hand, is more dependent on the bias, since the absorption coefficient at 1550 nm increases with the electric field. With an 80 μm-long device, a high responsivity of ~1.1 A/W can be achieved with >35 GHz bandwidth at 3.3V reverse bias, and the footprint area is only 0.6×80 μm. Therefore, the performance of the integrated detector also meets the needs of high speed Si microphotonic circuits. It should be noted that for the convenience of integration with $Ge_{1-x}Si_x$ (x=0.75%) EA modulators, we adopt the same composition for the $Ge_{1-x}Si_x$ (x=0.75%) photodetector. The device length can be further decreased if we use pure Ge material, since the absorption coefficient of Ge at 1550 nm is about an order of magnitude higher than that of $Ge_{1-x}Si_x$ (x=0.75%). Therefore, in the cases where modulator-detector monolithic integrated are not required, pure Ge photodetector will give even better performance. The design rules are the same as we have previously discussed in this section.

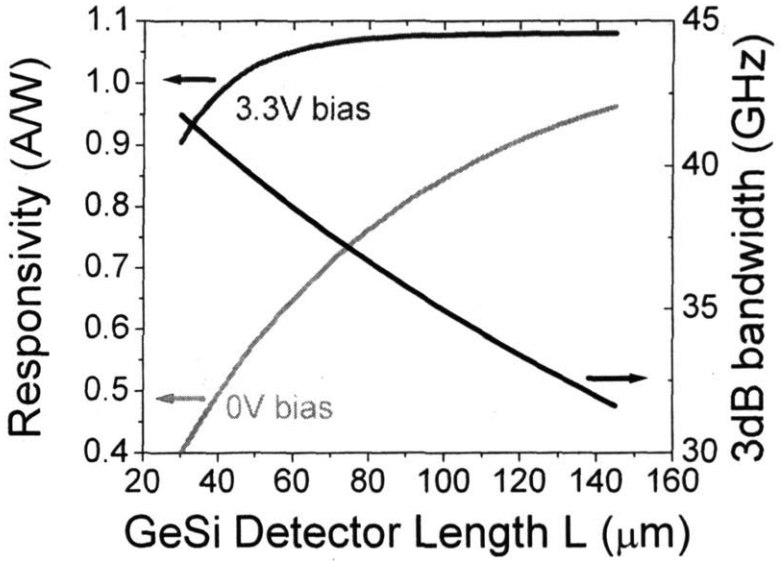

Fig. 4.21 Calculated responsivity and bandwidth of $Ge_{1-x}Si_x$ (x=0.75%) photodetectors at 0 V and 3.3V bias. Since the electric field in the $Ge_{1-x}Si_x$ (x=0.75%) layer is 10.1 kV/cm even at 0 bias and the carriers are already accelerated to the saturation velocity under such a high electric field, the bandwidth vs. device length is the same for 0V and 3.3V reverse bias.

4.3.3 Analysis on the Tolerance of Fabrication Error

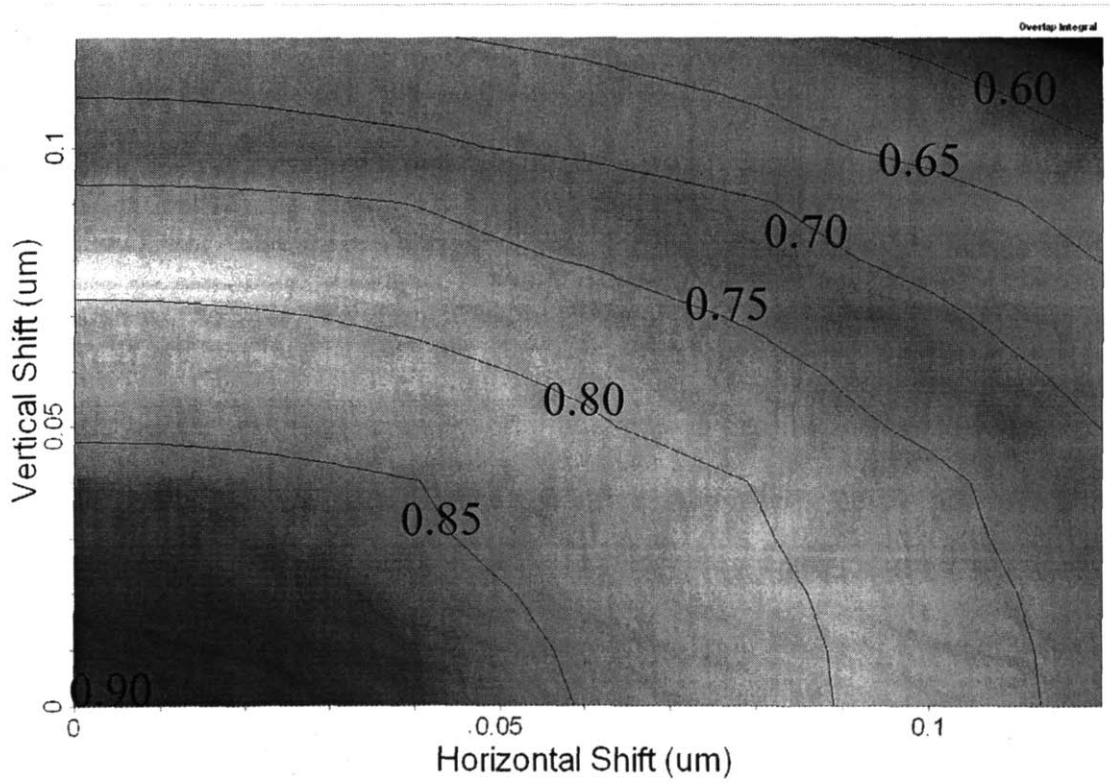

Fig. 4. 22. Modal overlap between the Si waveguide and the 600×400 nm $Ge_{1-x}Si_x$ EA modulator as a function of center-to-center misalignment in the horizontal and vertical directions.

Butt-coupling relies on the center-to-center alignment between the Si waveguide and the $Ge_{1-x}Si_x$ modulator for optimal coupling efficiency. However, in reality device fabrication errors often induces misalignments. In this section we will do an analysis on the effect of misalignment between the Si waveguide and the Ge EA modulator on the coupling efficiency.

Fig. 4.22 shows the modal overlap between the Si waveguide and the 600×400 nm $Ge_{1-x}Si_x$ EA modulator as a function of center-to-center misalignment in the horizontal and vertical directions. In 180 nm fabrication technology, the misalignment can usually be controlled to be <30 nm. We can see from Fig. 4.22 that the modal overlap is still >0.85 in this case, only slightly smaller than the modal overlap at 0 misalignment (0.90). Therefore, the device design can tolerate the fabrication error in 180 nm CMOS fabrication technology. In fact, we can still achieve ~0.70 modal overlap at 100 nm misalignment in both horizontal and vertical directions. The overall coupling loss increases to 3.2 dB in this case, just 2.1 dB higher than the case of perfect alignment. With the data in Fig. 4.22, we can conclude that our design can tolerate a misalignment of ~100 nm in the horizontal and vertical directions. Such fabrication error can be readily achieved with sub-500 nm CMOS fabrication technology.

Chapter 5. CMOS-compatible, Waveguide-integrated GeSi Modulators and Photodetectors.

Having discussed the design and expected performance of waveguide-integrated GeSi EA modulators and photodetectors, in this chapter we will present some preliminary results on the fabrication and performance of our first set of devices. We will first discuss the fabrication process to monolithically integrate the $Ge_{1-x}Si_x$ EA modulator and the photodetector. We then present the I-V characteristics of the $Ge_{1-x}Si_x$ modulator/photodetector obtained in this initial fabrication process. We further give the preliminary results on the responsivity and bandwidth of the waveguide-integrated detectors measured by injecting light from the input waveguide. Finally, we will discuss the problems to be overcome in the future runs of device fabrication to achieve detector/modulator devices with much better performance.

5.1 Fabrication Process Flow

As we mentioned in Chapter 4, with the butt-coupling scheme a 9.8 dB extinction ratio can be achieved with 4.8 dB insertion loss. With tapered coupling the performance is slightly better, but the requirement on lithography is hard to achieve. Therefore, we decide to adopt butt-coupling scheme in device fabrications. In Si microelectronic technology, devices are usually defined by sequential material deposition and etching. However, this method cannot be used to achieve butt coupling from Si waveguide to $Ge_{1-x}Si_x$ (x=0.75%) modulator in our case. Fig. 5.1 shows the reason. As we mentioned earlier, the $Ge_{1-x}Si_x$ (x=0.75%) modulator is a rectangle stripe with dimensions $0.6\times0.4\times50$ μm. If this structure is defined by lithography, then to form the Si waveguide we have to first

deposit a dielectric layer on Ge so that the Si waveguide can be elevated to the match the center of the $Ge_{1-x}Si_x$ structure, and then deposit a layer of Si on it. As a result, we will obtain a structure shown in Fig. 5.1. Obviously, this is not the structure we want to achieve in Fig. 4. 9. Therefore, another process has to be adopted to achieve an ideal butt-coupled structure.

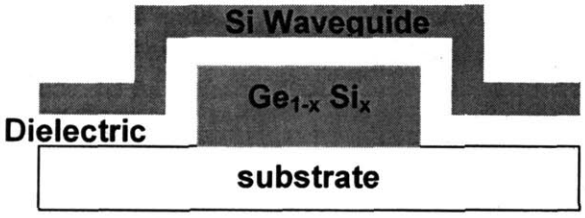

Fig. 5.1 Schematic picture showing that the conventional fabrication method of layer deposition followed by etching cannot be used to achieve butt coupling from Si waveguide to GeSi modulator.

Fig. 5.2 shows the process flow to achieve a butt-coupled $Ge_{1-x}Si_x$ modulator. The fabrication is based on an SOI substrate for an easy optical isolation from the Si waveguide to the Si substrate. As we have mentioned in Chapter 4, a Si waveguide has to be placed ~2 μm above the Si substrate to prevent the optical power from leaking into the substrate. For this reason, we choose a SOI substrate with 2 μm oxide layer. The top single crystal Si layer is doped p^+ (or n^+) by ion implantation (Fig. 5.2(a)). Si mesas are then formed by patterning the top Si layer (Fig. 5.2(b)). An oxide layer is deposited on top of the structure and planarized by chemical mechanical polishing (CMP) (Fig. 5.2(c)). We then deposit a layer of amorphous Si and pattern it to for the core of the Si waveguide, and an oxide layer is deposited on top followed by CMP to form the upper cladding of Si waveguide (Fig. 5.2(d)). Trenches are subsequently etched into this structure to expose the top of the Si mesas (Fig. 5.2(e)). Finally, $Ge_{1-x}Si_x$ material is selectively grown to overfill these trenches and planarized by CMP, and a poly-Si layer

with the opposite doping species to the single crystal Si mesas underneath the $Ge_{1-x}Si_x$ material is further deposited and patterned on top of the structure, as shown in (Fig. 5.2(f)).

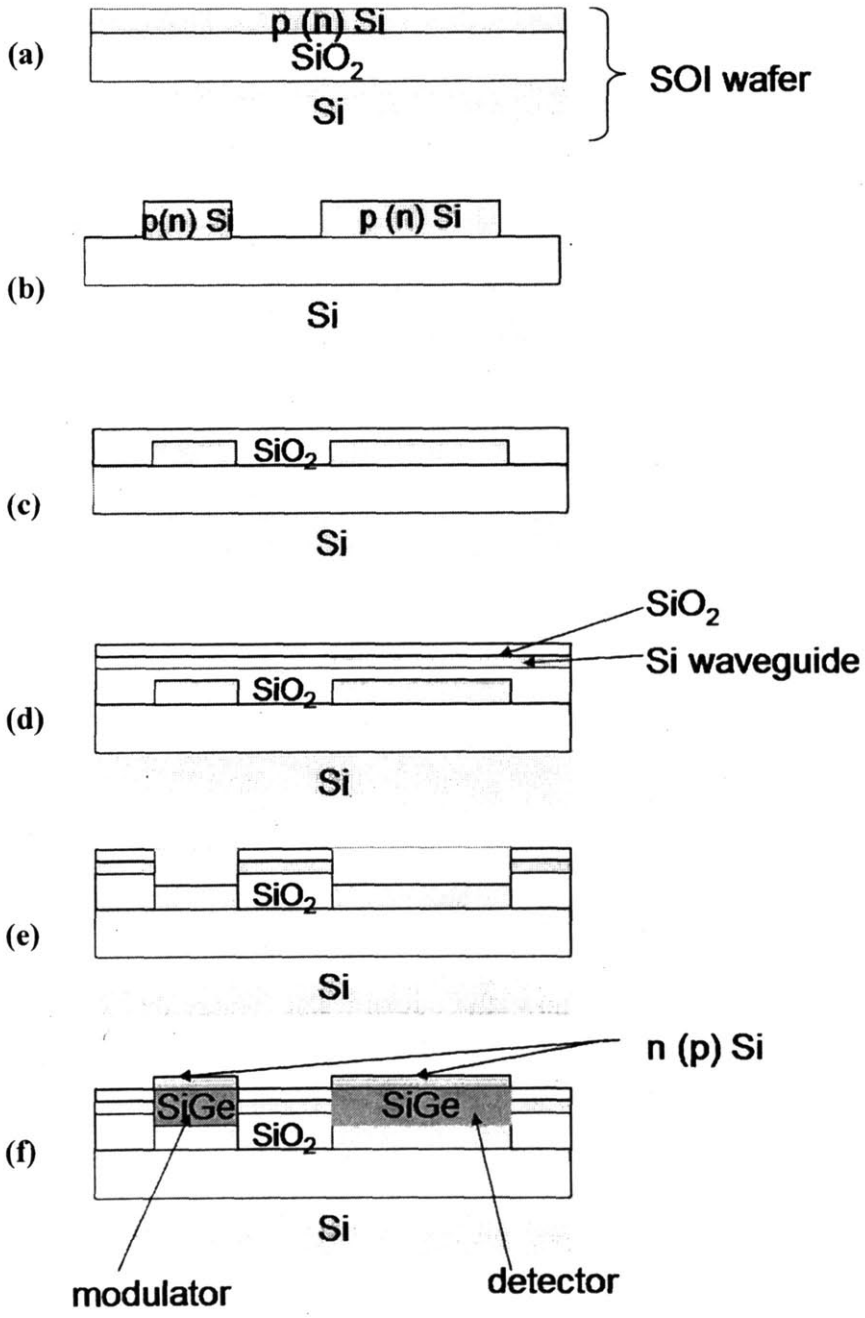

Fig. 5.2 Fabrication process of butt-coupled GeSi EA modulators and photodetectors

Metal electrodes can be used to contact the doped Si regions on tops and bottoms of the $Ge_{1-x}Si_x$ parts, and we will discuss about it in more detail in Section 5.3. The shorter $Ge_{1-x}Si_x$ structures are used as EA modulators, while the longer ones following them are used as photodetectors. This way, a monolithic integration of $Ge_{1-x}Si_x$ EA modulators and photodetectors can be achieved.

The most important step in this processing flow is the selective growth of $Ge_{1-x}Si_x$ to overfill the trenches. This process is very similar to a Cu damascene process used in CMOS circuits [117], except that we are now filling semiconductor materials epitaxially into the trenches. In the next section we will focus our discussions on the trench-filling GeSi selective growth.

5.2 Trench-filling Selective Growth of $Ge_{0.9925}Si_{0.0075}$

To achieve the trench-filling selective growth of $Ge_{1-x}Si_x$, we have to study the epitaxy surface shapes on a patterned substrate. This is very different from Cu damascene process because of the complicated faceting of semiconductor materials during the growth. Here we present how to predict the crystal shape by Borgstrom and Wulff construction, given that we know the growth rate along different crystallographic orientations.

5.2.1 The Borgstrom Construction and the Wulff Construction [118]

The shape of a growing crystal on a non-planer surface was first predetermined by a simple construction proposed by Borgstrom. It is actually rather intuitive: draw parallel lines displaced from each facet proportional to the growth rate in the orientation

perpendicular to the facet, and the shape enclosed by these lines determines the crystal shape.

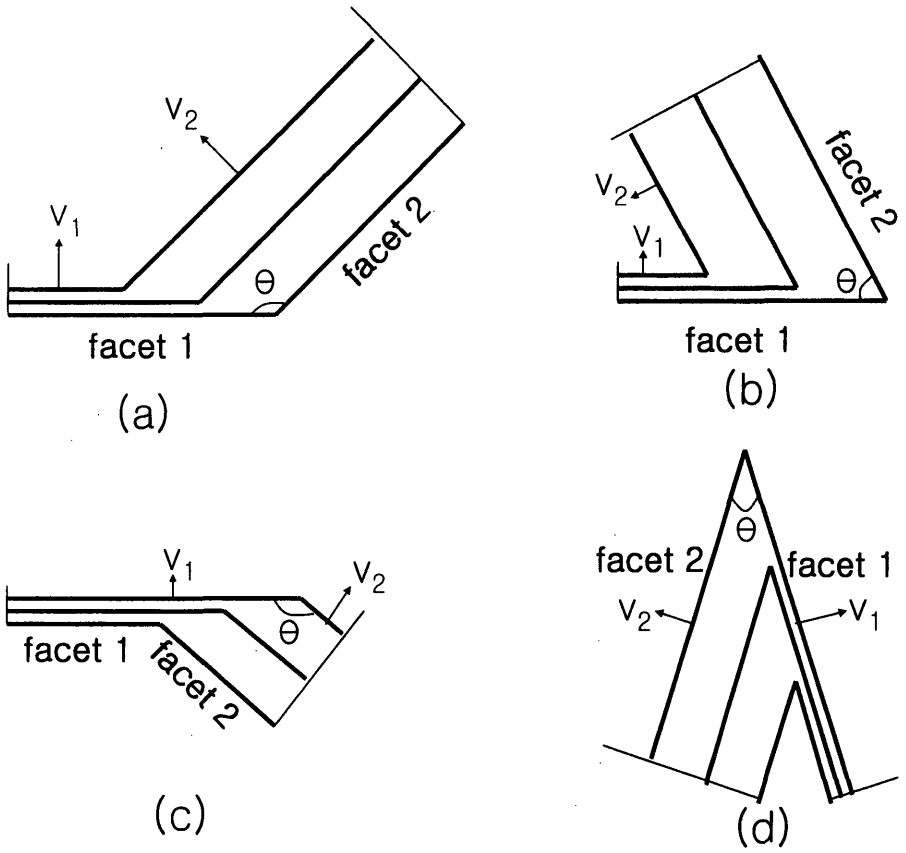

Fig. **5.3 Borgstrom construction on (a) a concave surface with $90° < \theta < 180°$, (b) a concave surface with $0° < \theta < 90°$, (c) a convex surface with $90° < \theta < 180°$, and (d) a convex surface with $0° < \theta < 90°$**

Fig. 5.3 shows such an example, with the growth rate of direction 2 faster than that of direction 1. For easy comparison, the area of facets 1 and 2 are set equal at the beginning. As shown by the construction, on a concave surface with θ>90° the area of the fast growth facet increases at the cost of area decrease of the slow growth facet (Fig. 5.3(a)), while for θ<90° the area of both facets decreases but the slow growth facet shrinks faster (Fig. 5.3(b)). On the whole, growth on a concave surface favors faster growth facets. On a convex substrate with the convex angle θ>90°, the slow growth facet would consume

the fast growth facet during growth, while for θ<90° both facets will grow in area but the slow growth facet will increase at a higher rate than the fast growth one. On the whole, growth on a convex surface favors slower growth facets. This simple approach explains why growing on convex surfaces tend to minimize the fast growth facets, while concave ones tend to minimize slow growth facets. However, this method incorporates assumptions that could lead to inaccurate constructions. The construction implicitly assumes that the growth rates of the orientations between the growth directions of two neighboring facets are linearly interpolated. But if the growth rate has other maxima or minima between the growth directions of the facets, this construction could give incorrect results.

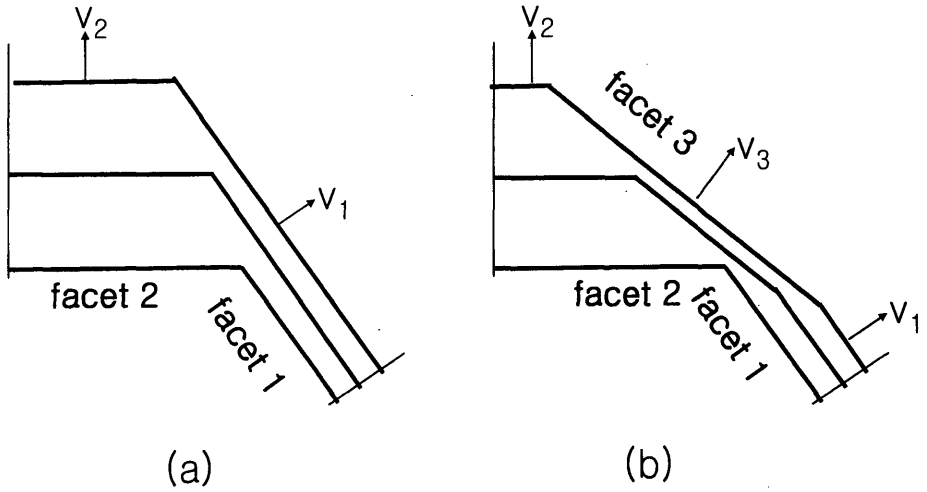

Fig. 5.4 Schematic drawings showing the difference between the Borgstrom and the Wulff construction. Assuming a convex surface consisting of facets 1 and 2, Borgstrom construction predicts the evolution in (a). However, the Wulff construction takes into account an even slower growing direction 3 between facets 1 and 2, so the result from Wulff construction in (b) is different from (a).

A more general construction method is the Wulff construction. It can not only determine the epitaxy shapes on non-planar surfaces, but also the case of selective growth in a patterned window. It takes into account the growth rate in all directions instead of

assuming the growth rates of the orientations between the growth directions of two neighboring facets are linearly interpolated. Fig. 5.4 gives an example showing the difference between the Wulff construction and the Borgstrom construction. Let us assume we start with a convex substrate with facets 1 and 2 exposed on the surface and growth rate $v_2 > v_1$. There is a direction 3 between the growth directions of facets 1 and 2, where the growth rate is lowest ($v_3 < v_1 < v_2$). From Borgstrom construction, the result will be an extension of facet 1 with the growth and facet 3 will never appear because it assumes the growth rate in direction 3 is between those in directions 1 and 2. However, the Wulff construction takes into account growth rate in all directions and correctly predicts that facet 3 will show up after some growth time.

5.2.2 Application of the Wulff Construction to $Ge_{1-x}Si_x$ Selective Growth

Ideally a complete polar diagram of growth rate in different directions should be used for the Wulff construction. In practical applications, however, the most important information is related to the orientations with a local maximum or minimum in growth rates. It has been reported that {111} and {311} are the two slowest growth facets in Si epitaxy [119]. In the case of Ge selective growth on Si, the dominant facets are also {111} and {311} when the trenches are aligned to <011> directions from our study. Since the material is grown on {100} substrate, the growth rate in [100] direction certainly has to be taken into account, too. Therefore, to predict the shape of the selectively grown Ge deposited in a narrow trench we will only consider these three facets in our Wulff construction, especially the ratio of growth rate in <111>, <311> and <100> directions.

We have studied the growth rate of Ge on Si in <111>, <311> and <100> directions with the selectively grown samples mentioned in Chapter 2, Section 2.2.

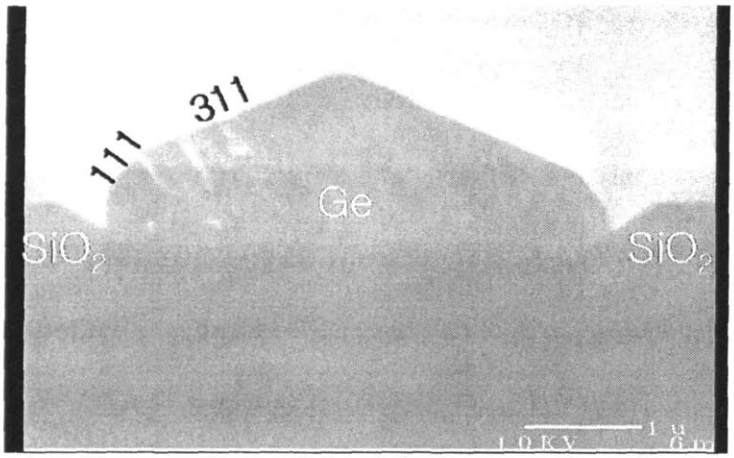

Fig. 5.5. Cross-sectional SEM image of a 4× 100 μm Ge stripe. (311) and (111) facets are revealed

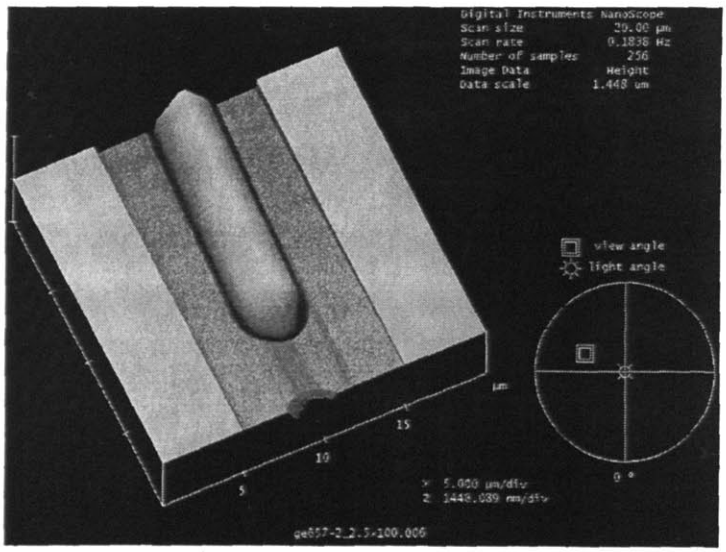

(a)

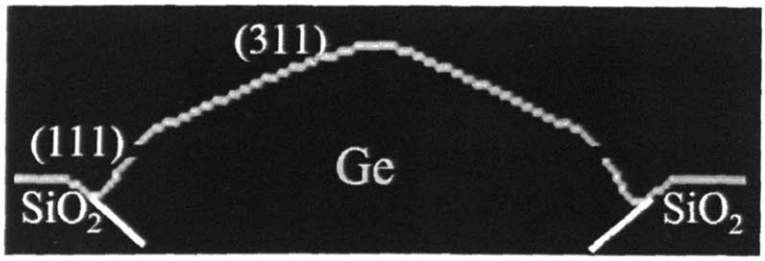

(b)

Fig. 5.6 (a) 3D AFM image of f a 4× 100 μm Ge mesa, and (b) cross-sectional profile obtained from the 3D AFM image.

The edge of the features are along the <110> directions due to the wafer alignment of the lithography. Cross-sectional SEM was used to observe the cross-section of the elongated rectangular Ge stripes and identify the facets. Fig. 5.5 shows the cross-sectional SEM image of a 4×100 μm Ge stripe. From the angles between the facets and the substrate surface (100) plane, we identify the facets to be (311) and (111). The slanted side wall of the trench results from the dilute HF wet etching. Fig. 5.6 shows an AFM image of the mesa and the cross sectional profile obtained from the 3 dimensional scan of the AFM. As we can see, AFM gives almost the same cross-sectional profile as the SEM, except for the details about the rounded corner at the joint of (111) facet and the SiO_2 side wall of the trench. This is because the AFM tip did not reach into the corner between (111) facet and the SiO_2 sidewall during the scan. Nevertheless, it gives correct information about the position of the (311) and (111) facets. Since AFM is non destructive to the samples and much easier to do than cross-section SEM, it can be used as a quick and easy alternative to cross-sectional SEM to check the facet profile. To obtain (311) and (111) facet growth rate, we compare the cross-sectional profile of 4×100 μm Ge mesas grown in the UHVCVD reactor for various time. This comparison gives the evolution of the mesa structure and allow us to derive the grow rate of (311) and (111) facets. The (100) direction growth rate was directly obtained from blanket Ge films grown on Si (100) substrate. Our results show that the ratio of the growth rate in [111] direction to [311] to [100] is 1:1.4:2.4. It is interesting to compare the grow rate ratio of [100] to [311] direction to the calculated result from a ledge flow model [120]. As shown in Fig. 5.7, the ledge flow model considers that the epitaxy results from the extension of terraces on (111) planes. As long as the substrate is not (111), these terraces already pre-exist on the

surface of the substrate, and atoms preferably deposit at the edge of the terraces to reduce the surface energy. Thus, the terraces extend in area and the thickness of the film in the growth direction increases. The extension of the terraces on (111) planes is called the "ledge flow".

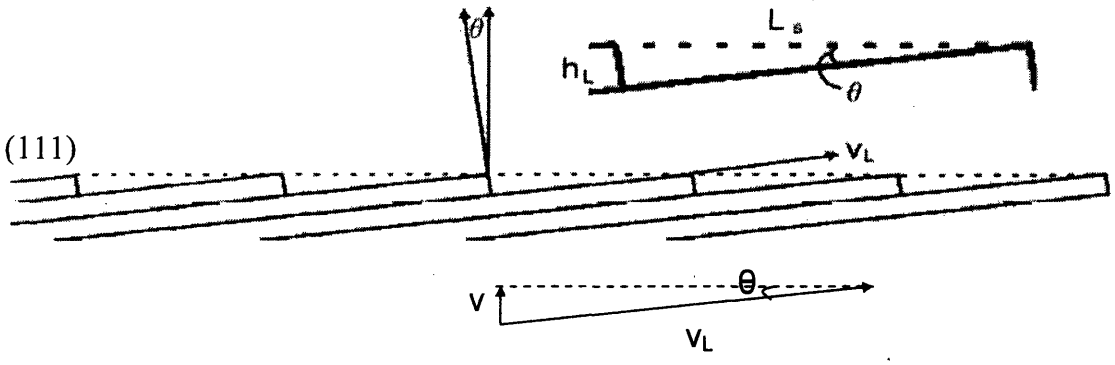

Fig. 5.7 Schematic diagram illustrating the ledge flow model of epitaxial growth.

From the geometry in Fig. 5.7, one can easily see that the growth rate in a certain direction is equal to the ledge flow rate v_L times $\sin\theta$, where θ is the angle between the surface plane and the (111) plane. The growth rate in (111) direction, on the other hand, is limited by the nucleation rate of terraces and cannot be predicted directly by the model. According to the ledge flow model, the growth rate ratio of (100) to (311) should be $v_L \sin(54.7^\circ)/v_L \sin(29.5^\circ)=1.66$. Our experimental value is 2.4/1.4=1.71, very close to the theoretical value. This result indicates that the Ge growth in [100] and [311] directions is achieved via ledge flow.

Now that we know the ratio of growth rate in [111], [311] and [100] directions, we should be able to predict the crystal profile of Ge mesas grown in an elongated, rectangular trench along <110> direction by the Wulff construction. Especially, we would like to estimate how much time it takes to fill a trench if we know the grow rate in

the [100] direction (which can be easily determined in blanket film growth). Assuming a trench with a height of h and a sidewall angle of ϕ, Fig. 5.8 shows the Wulff construction when we consider (111), (311) and (100) facet growth.

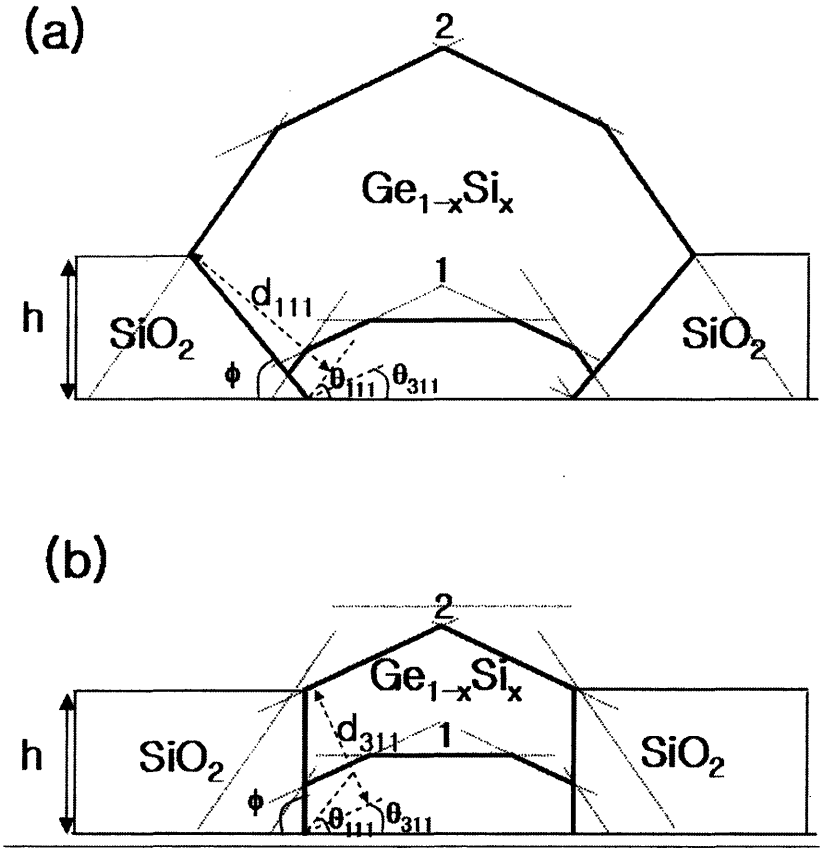

Fig. 5.8 The Wulff construction of $Ge_{1-x}Si_x$ grown in an elongated rectangular trench. The figures show the cross-sections in the transverse direction of the trenches. (a) When the sidewall angle ϕ<82.5°, the trench filling process is determined by the growth of (111) facet. (b) When the side wall angle ϕ>82.5°, the trench filling process is determined by the growth of (311) facets. The dashed lines at corner of the trench indicates the starting positions of (111) and (311) facets. The dotted lines demonstrate the Wulff construction of (111), (311) and (100) facets. The area enclosed by the dotted lines and the SiO_2 side wall determines the shape of the GeSi crystal (thick black lines). Stage 1 indicates an initial growth profile, and stage 2 corresponds to the moment when the trench is just filled up.

Note that since atoms deposit all over the bottom of the trench at the beginning, the growth of (111) and (311) facets actually start from the inner corner of the trench, as indicated by the black dashed lines in the figure. The dotted lines demonstrate the Wulff

construction of (111), (311) and (100) facets. The area enclosed by these dotted lines and the sidewall of the SiO_2 trench determines the final Ge crystal shape grown in the trench. Stage 1 in the figure indicates an initial growth profile, and stage 2 corresponds to the moment when the trench is just filled up. When $\phi<82.5^\circ$, the (111) facets will show up in the trench during the growth according to the Wulff construction, and the grow rate of (111) facets will determine the trench filling rate. As shown in Fig. 5.8 (a), in this case the time required to fill in a trench is

$$t_{fill} = \frac{d_{111}}{v_{111}} = \frac{(h/\sin\phi)\sin(\phi+\theta_{111})}{v_{111}} = 2.4h\sin(\phi+54.7^\circ)/v_{100}\sin\phi \quad (5.1)$$

. Here $\theta_{111}=54.7^\circ$ is the angle between (111) and (100) planes. When $90^\circ>\phi>82.5^\circ$, the (111) plane will not show up in the trench during the growth, and the trench filling rate is determined by the growth rate of (311) facet. In this case we have

$$t_{fill} = \frac{d}{v_{311}} = \frac{(h/\sin\phi)\sin(\phi+\theta_{311})}{v_{311}} = 1.7h\sin(\phi+25.2^\circ)/v_{100}\sin\phi \quad (5.2)$$

Note that we have not considered the effect of the rounded corners at the joints of facets and between the facets and the SiO_2 sidewall in this model. The convex corner at the joint of two facets has a small radius and a positive capillary pressure, which drives the atomic diffusion to form a rounded corner to reduce the pressure. In reality the trench filling is not fully complete due to these rounded corners. The growth time needed to fully fill a trench may thus be slightly longer than Eq. 5.1 and 5.2 indicate depending on the growth temperature and surface diffusion.

Fig. 5.9 overlaps our prediction of the crystal profile at different stages of the growth with a cross-sectional SEM image of a 1×100 μm $Ge_{1-x}Si_x$ (x=0.8%) stripe. Stage 1 in the figure indicates the profile when the trench is just filled, and stage 2 indicates the

final crystal shape after the growth is completed. The growth rate in the [100] direction in this case is ~550 nm/h. As we can see, the prediction of the ultimate shape after the growth overlaps with the cross-sectional SEM image fairly well, except of the $(1\bar{1}1)$ facet on the left side and the (111) facet on the right side near the SiO_2 surface. From the Wulff construction, these two facets should be at positions BC and its mirror position B'C'. Therefore, the formation of these two facets is due to another reason.

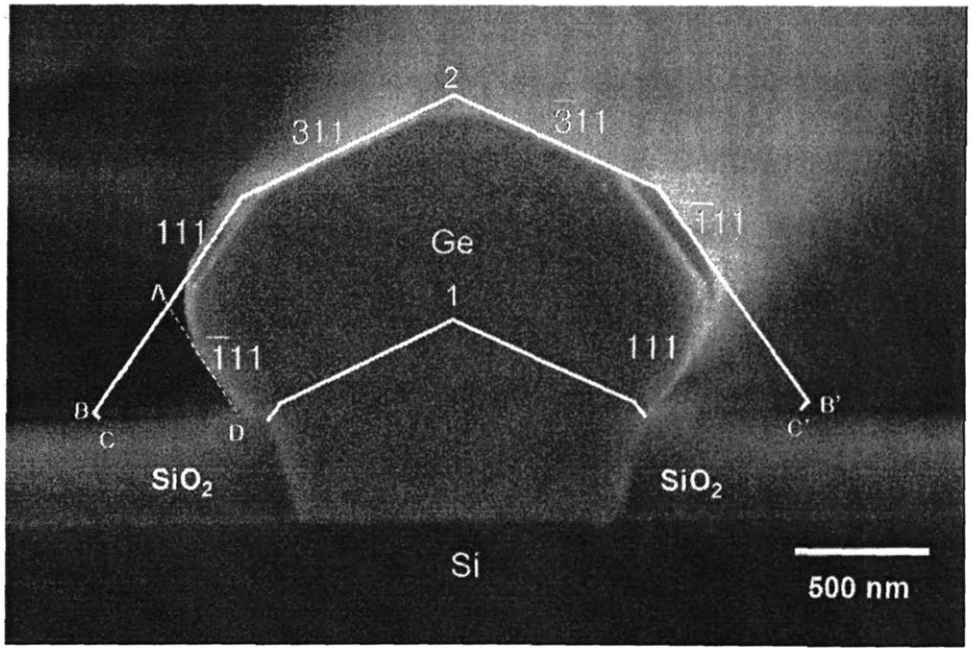

Fig. 5.9 Cross-sectional SEM of a 1 × 100 μm mesa and its comparison with the growth profile predicted by the Wulff construction. Stage 1 in indicates the profile when the trench is just filled, and stage 2 indicates the final crystal shape after the growth is completed.

Germanium is known to dewet on SiO_2 surface [121], meaning that the Ge/SiO_2 interfacial energy is high. Therefore, by forming a $(1\bar{1}1)$ facet AD instead of BC, the surface energy remains the same (since AD=AC+BC and all of them are {111} planes), while the interfacial energy of CD is eliminated. Therefore, the formation of the $(1\bar{1}1)$ facet at AD instead of BC is driven by the reduction of Ge/SiO_2 interfacial energy. This

phenomenon also indicates that the Ge facet growth at the current growth rate (550 nm/h) is still thermodynamically driven and substantial surface diffusion occurs during the growth.

In summary, we have discussed how to derive the shape of the $Ge_{1-x}Si_x$ crystal grown in a trench based on the knowledge of the growth rate ratio in some important crystal directions and the Wulff construction. The model agrees fairly well with the experimental results, and can be used to evaluate the minimum growth time required to fill a trench, as well as the ultimate shape after the growth. The growth in trenches of other crystal directions would vary based on the geometric configuration of the Wulff construction. It would be interesting to investigate the orientation dependence of trench filling in future experimental research.

5.3. Electrode Design of GeSi EA Modulators and Photodetectors

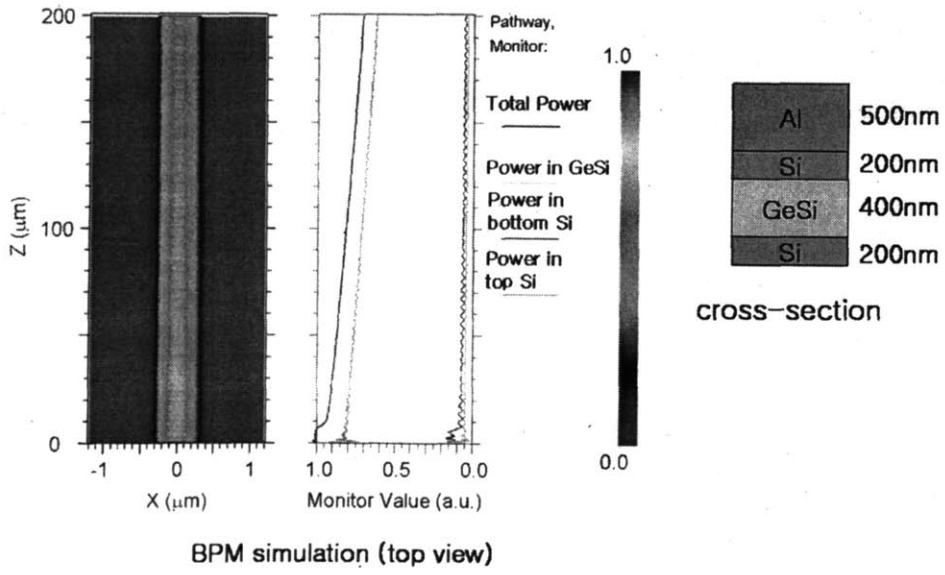

Fig. 5.10 BPM simulation of modal propagation loss due to the top Al contact.

Electrode design is usually a relatively simple issue in most devices. Metal electrodes are usually deposited all over the n^+ and p^+ semiconductor regions to achieve low contact resistance. However, in the case of waveguide integrated GeSi modulators and photodetectors, two issues should be noted: (1) the electrodes should not be too close to the active device region, since metal has a high imaginary refractive index and will increase the insertion loss of the modulator. It also disturbs the optical mode in the modulator. (2) the electrodes cannot be too far from the device region, either, since it will increase the series resistance. As and example, Fig. 5.10 shows a BPM simulation of a Al electrode right on top of a 200nm n^+ poly Si layer. The refractive index of Al at 1550 nm is $n_{Al} = 1.28+15.0i$ [122]. The modal propagation loss due to the Al layer is obtained by setting the extinction coefficient of GeSi to 0. The result shows that the propagation loss due to the Al layer is as high as 58 dB/cm. Therefore, it is clear that we do not want to put metal layer directly on top of the poly Si. Our simulation also shows that if the Al layer is placed >1 μm away from the active region, its perturbation on the optical mode can be neglected. Therefore, in our design we put the metal electrode on the sideway, as shown in Fig. 5.11. In the current CMOS technology, tungsten studs are used to contact heavily doped Si as a diffusion barrier and electrical contact. The size of the stud is about 500 nm in diameter. Since the length of the devices is in the order of tens of μm, one stud is obviously not good enough to decrease the series resistance. Therefore, we put an array of tungsten studs along the length of the device to reduce the contact resistance. In this configuration, the series resistance due to the n^+ and p^+ Si is expected to be less than 10 Ω if the doping level in Si is $2\times10^{19}/cm^3$ and there is no detrimental effect on the optical mode in the modulators detectors.

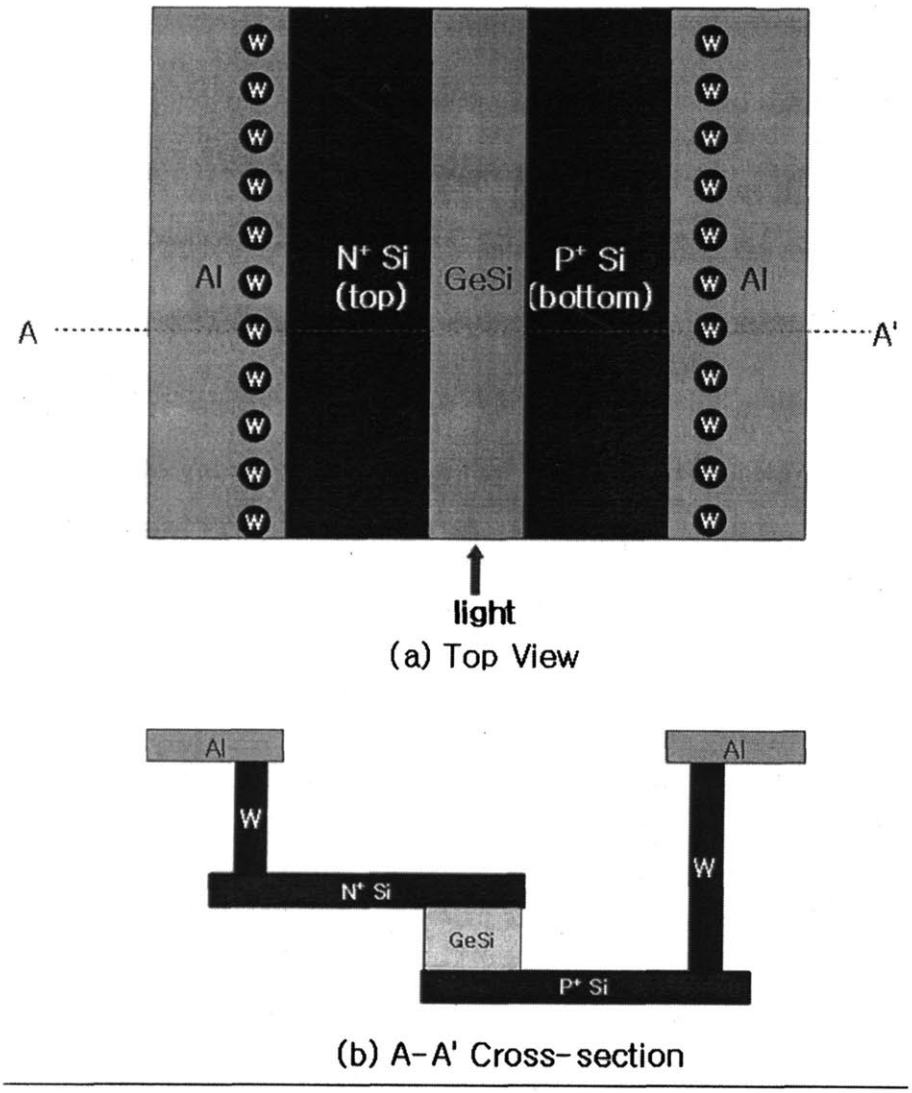

Fig. 5.11 Electrode configuration in waveguide-integrated GeSi modulator/detector design. (a) top view, and (b) Cross-section view at A-A' shown in (a).

5.4 *I-V* Characteristics of Waveguide Integrated GeSi Modulators/Photodetectors

The butt-coupled GeSi EA modulators/photodetectors are fabricated in BAE systems, Inc. with a standard 180 nm CMOS technology line. To accommodate the CMOS circuit architecture conveniently, the thickness of the GeSi modulator was chosen to be 600 nm instead of 400 nm. Other design parameters are the same as what we described in Chapter 4.

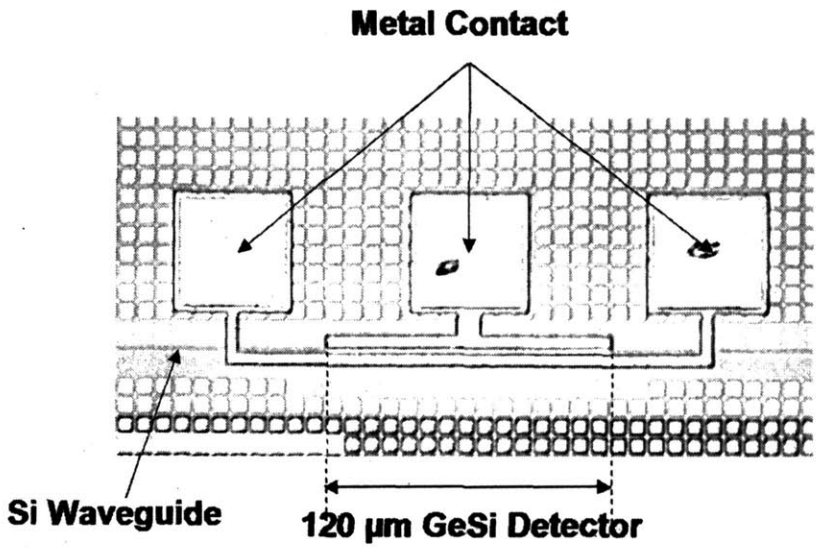

Fig. 5.12 Top view of a 120 μm long GeSi photodetector coupled with Si Waveguides.

Fig. 5.12 shows the top view of a 120 μm long GeSi photodetector coupled with Si Waveguides. For high speed measurements the metal contact pads are in the ground(left)-signal(middle)-ground(right) configuration, as already mentioned in Chapter 3. Fig. 5.13 (a) and (b) show the I-V and J-V characteristics of some waveguide-integrated $Ge_{0.992}Si_{0.008}$ *p-i-n* diodes with different length. The series resistances and the non-ideality factors are derived with the method described in Chapter 3. Although diode behavior is observed, yet the dark current density is much higher than the Ge diodes in Chapter 3. The dark current density at -2V in these device is in the order of 100 A/cm^2, while for the Ge diodes described in Chapter 3 it was only $0.02A/cm^2$. On the other hand, the non-ideality factor in the waveguide integrated devices are around 3 instead of close to 1, indicating that generation/recombination in the depletion region dominates the I-V characteristics. Some reports suggests that a non-ideality factor ~3 could be due to surface recombination processes [123, 124].

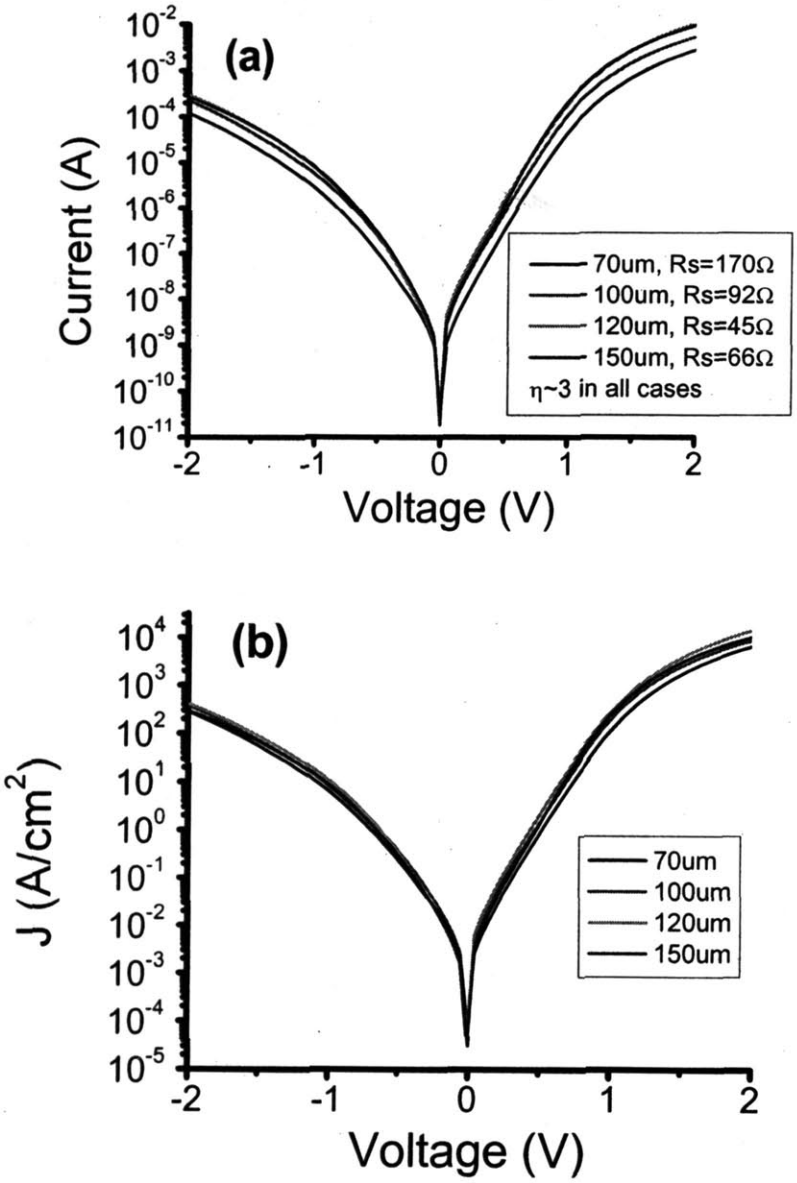

Fig. 5.13 I-V and J-V characteristics of waveguide integrated $Ge_{0.992}Si_{0.008}$ photodetector/modulator

There are several possible reasons for this high leakage current due to fabrication defects. First, the $Ge_{1-x}Si_x$ (x=0.8%) material itself has been shown to be defective. Fig. 5.14 (a) shows a high resolution cross-sectional TEM image of the interface between $Ge_{1-x}Si_x$ and Si. Due to the over-etch of the reactive ion etching (RIE) to form the trenches, a ~2 nm amorphous layer was formed on the top of the single crystalline Si. This layer has been identified to be a fairly robust fluoride material formed by the dry etching reaction [125,126,127]. When the over-etch is >10%, a ~2 nm layer on the Si surface is formed and cannot be removed with regular chemical cleaning before the epitaxial growth. The material grown on these trenches are rough and often discontinuous. The ultra- high boron doping during the ion implantation (~$10^{21}/cm^3$ at the Si surface) may also severely damage the Si lattice and induce defects in the epitaxial growth. In fact, the implantation concentration in the Si layer was designed to be $2 \times 10^{19}/cm^3$, but a much higher implantation dose was used during fabrication due to the conventional fabrication recipe in BAE systems for source/drain implantation in CMOS devices. As a result, the GeSi grows on a defective Si surface and crystal defects like micro-twins occur due to this reason.

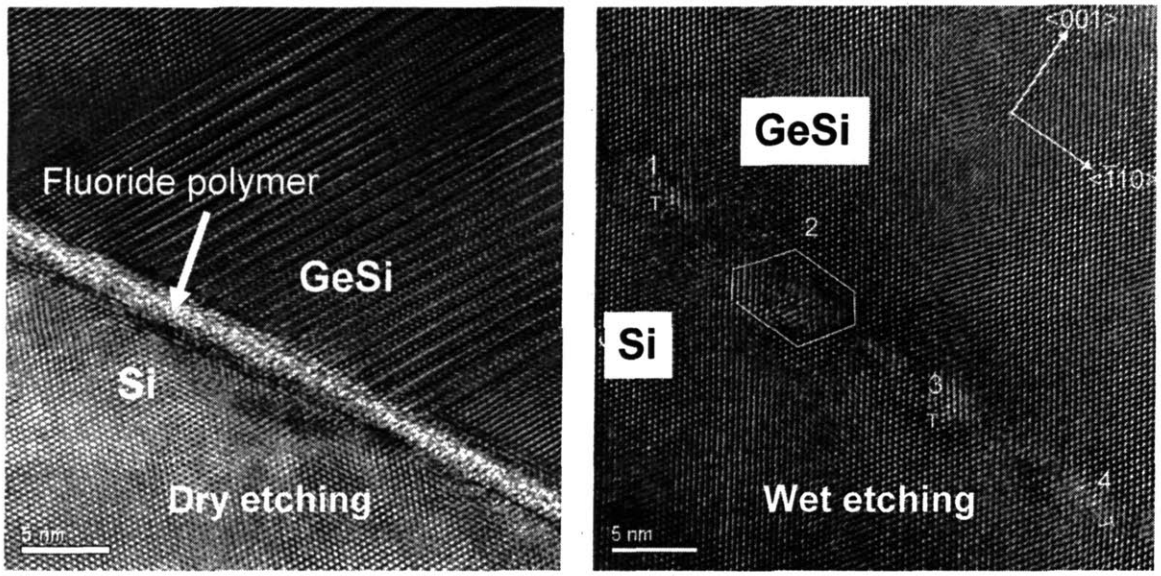

Fig. 5.14 High resolution cross-sectional TEM images at the interface between GeSi and Si of a reactive ion etched trench (left) and a wet etched trench (right). TEM analysis courtesy of Dr. Jinggang Lu, North Carolina State University.

Strictly speaking, the $Ge_{1-x}Si_x$ material is no longer single crystalline. When we mimic the implantation and reactive ion etching conditions on a blanket Si wafer, the $Ge_{1-x}Si_x$ (x=0.8%) grown on the wafer is visually blurry due to the polycrystalline nature. In contrast, the $Ge_{1-x}Si_x$ grown on wet etched Si surface is smooth (RMS roughness of about 2 nm) and there is no damaged layer at the GeSi/Si interface (Fig. 5.14(b)). Instead, misfit dislocations can be clearly identified in the HRTEM image, as indicated by numbers 1-4 in Fig. 5.14(b). Since the trenches in the integrated devices are implemented by RIE while those in free space detectors mentioned in Chapter 3 are fabricated by wet etching, the material quality in the integrated detectors/modulators is much worse than the free space ones. The defects in the $Ge_{1-x}Si_x$ layer due to the damage on the Si surface could also lead to much higher leakage current.

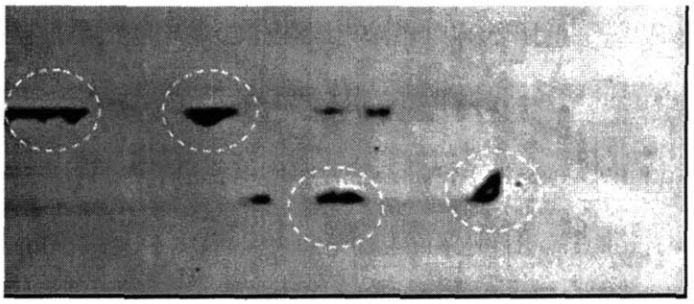

Fig. 5.15 SEM image of a GeSi stripe after CMP. The white circles indicate the defects due to the rip-off of GeSi material in the CMP process.

Secondly, the sidewall of the Ge stripes are damaged during CMP process. Fig. 5.15 shows such an example. The GeSi near the side wall was peeled off during the CMP process, and these defective edges can be the source of high peripheral leakage. Although not all the stripes show such a high density of CMP defects, there are typically some defects at the sidewall. A third possible reason is that the dopant in the top poly Si layer may diffuse along the GeSi/SiO_2 side wall boundary much faster than it does in the bulk. If so, the side wall of GeSi mesas could be heavily doped with the n-type dopant and form a conductive path, especially considering the arsenic peak concentration in the poly Si layer is $10^{21}/cm^3$ and the concentration at poly Si/Ge interface is still about $10^{19}/cm^3$. Arsenic is a fast diffuser in Ge [128] and is not ideal for our GeSi p-i-n diode device. Instead, phosphorous is a much better n type dopant in this case since it is the slowest diffuser among all n-type dopant in Ge. This is why we chose phosphorous doping in our free space detectors mentioned in Chapter 3. However, due to the convention of CMOS fabrication in BAE systems Inc., arsenic was chosen instead of phosphorus. Since the dopant activation temperature after annealing is 700 °C and the diffusion coefficient of As is about an order of magnitude higher than that of P at this temperature, using As instead of P as the n-type dopant could severely worsen the problem.

To improve these fabrication steps, we should modify the fabrication process in future device fabrications. To avoid the implantation damage on Si surface, we can adopt the originally designed B concentration of $10^{19}/cm^3$ instead of $10^{21}/cm^3$ in the current fabrication process. This way the implantation dose is two orders of magnitude lower and the implantation damage can be greatly reduced. In fact, we have grown Ge on such implanted wafers with $10^{19}/cm^3$ concentration, and the Ge quality is similar to those grown on brand new Si wafers. To get rid of the fluoride layer due to the over-etch of RIE, we can leave ~5 nm oxide layer unetched during the RIE, and take off this layer by dilute HF dip before the growth. This way the plasma will never see the Si surface directly and no fluoride polymer layer will be formed on the Si surface. This method has also been shown to be effective to achieve a high quality $Ge_{1-x}Si_x$ epitaxial layer. The CMP process can be improved by depositing a dielectric layer on top of Ge mesas/stripes before CMP. This way the Ge material will suffer much less direct impact during the CMP process and the material at the edge of the trenches will not be peeled off. Finally, the n type dopant can be changed from As to P, so that much less dopant diffusion happens in the intrinsic GeSi layer. The implantation depth can be a shallower to accommodate the dopant diffusing during activation annealing. All these solutions are still compatible with CMOS fabrication technology, and the modifications are easily achieved.

5.5 Responsivity and Bandwidth of Waveguide-coupled GeSi Photodetectors

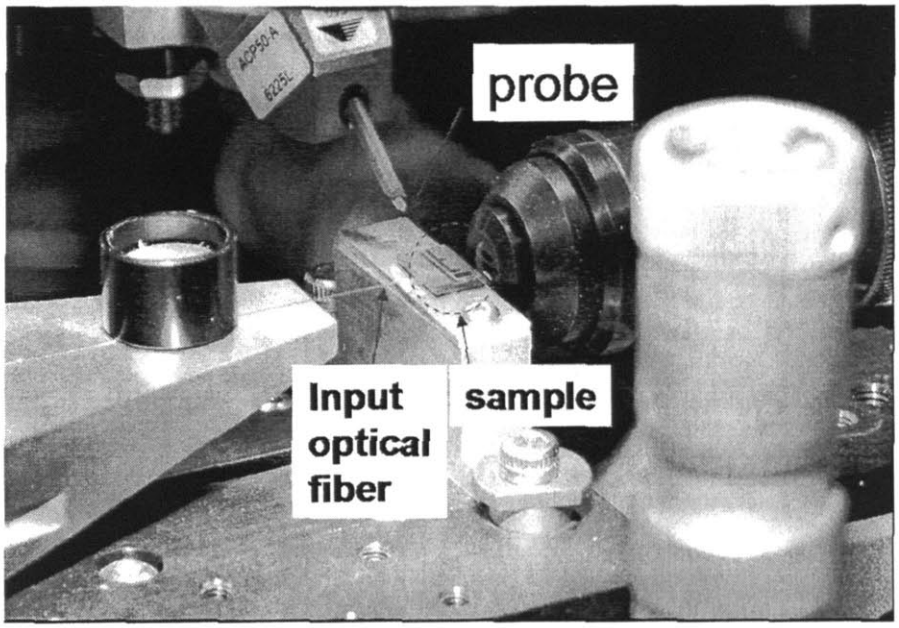

(a)

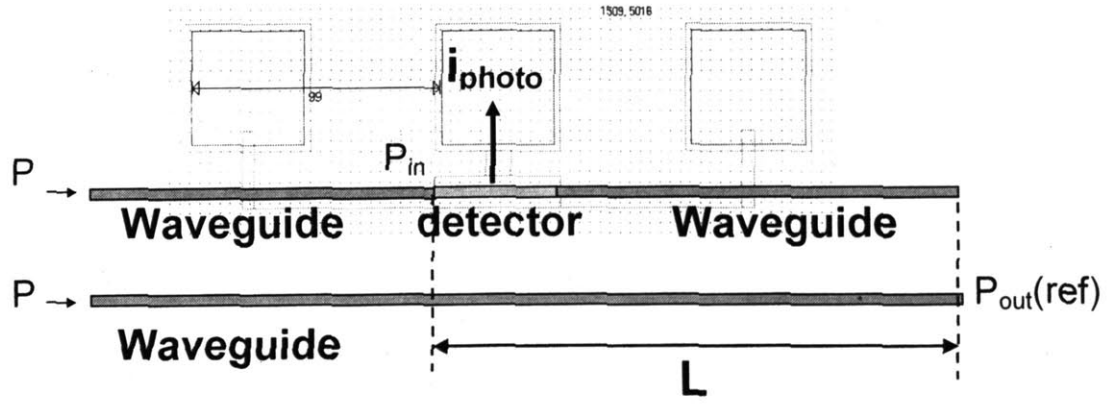

(b)

Fig. 5.16 (a) Experimental setup for the responsivity measurement of waveguide-integrated GeSi photodetectors. (b) Schematic figure showing the method of determining the detector responsivity.

Fig. 5.16 (a) shows the experimental set up we used to measure the responsivity of the waveguide coupled $Ge_{1-x}Si_x$ (x=0.8%) photodetector. The light from a single mode tunable laser source (tuning range 1480-1570 nm) is coupled into the input optical fiber and then into the input Si waveguide on the sample. The light travels along the

waveguide, passes through the $Ge_{1-x}Si_x$ modulator/detector device, and then couples into the output Si waveguide and exits the sample. An electric probe is connected to the preamplifier mentioned in Chapter 3, and can be landed on the electrical contacts of the $Ge_{1-x}Si_x$ modulator/photodetector to apply the reverse bias and read out the photocurrent at the same time. The output light is focused by an objective lens to a photodetector so that its intensity can be monitored. To decrease the noise during the measurement, the laser was chopped at a low frequency of 400 Hz, and a lock-in amplifier is connected to the preamplifier to read out the photocurrent signal, similar to Fig. 3.5. To determine the responsivity of the photodetector, we inject a certain optical power into an optical line with a $Ge_{1-x}Si_x$ detector and read out a photocurrent i_{photo}. We then keep the same input optical power and measure the output light intensity ($P_{out}(ref)$) from a reference Si waveguide in the vicinity of the line with the $Ge_{1-x}Si_x$ detector (Fig. 5.16b). We also have paper-clip waveguide structures on the same wafer so that we know the propagation loss of the light in the waveguide. Suppose the propagation loss in the Si waveguide is γ in terms of dB/cm and the distance from the input port of the $Ge_{1-x}Si_x$ detector to the output end of the output Si waveguide is L in unit of cm (Fig. 5.16b). Then the input optical power at the beginning of the $Ge_{1-x}Si_x$ detector is $P_{in}=10^{\gamma L/10} P_{out}(ref)$. Therefore, the responsivity is just $R = \frac{i_{photo}}{10^{\gamma L/10} P_{out}(ref)}$.

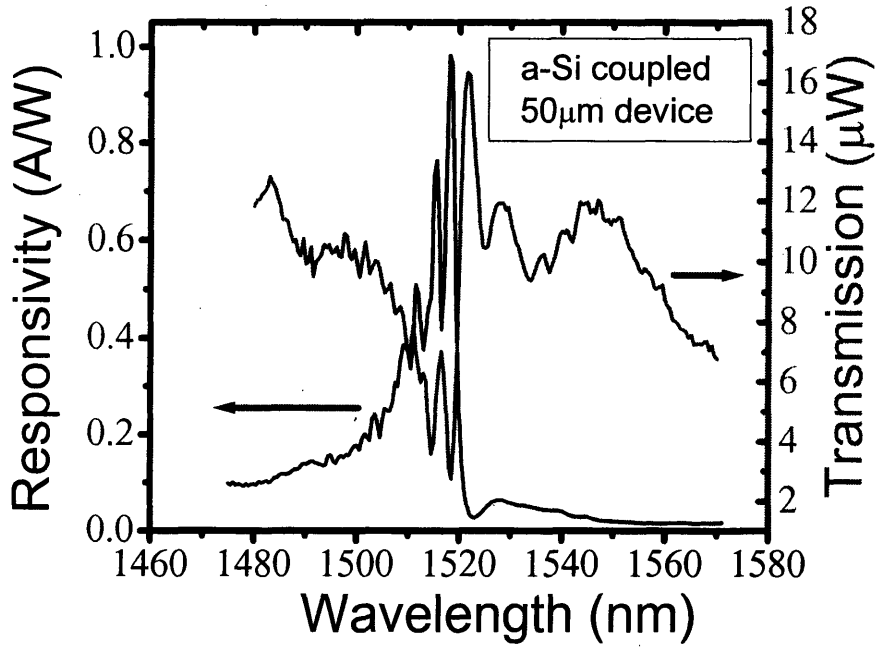

Fig. 5.17 Spectral responsivity and transmitted power of a 50 μm long, waveguide coupled $Ge_{0.992}Si_{0.008}$ photodetector. A 4 V reverse bias was applied for the responsivity measurement.

The spectral responsivity of a 50μm-long $Ge_{1-x}Si_x$ photodetector at 4 V reverse bias is shown in Fig. 5.17. There is a sharp rise in responsivity at 1520 nm, consistent with the designed direct band edge of the $Ge_{0.992}Si_{0.008}$ material. The responsivity at 1518 nm is 1.0 A/W, which corresponds to about 83% external quantum efficiency. An interesting feature of the responsivity curve is that the responsivity decreases fairly sharply for wavelength<1520 nm. From Eqs. 4.27 and 4.28, we can see the responsivity of a waveguide-coupled photodetector is related to its coupling efficiency and the material absorption. The absorption coefficient of $Ge_{0.992}Si_{0.008}$ increases with the decrease of the wavelength in the range of 1300-1600 nm. If we assume the coupling efficiency is similar over the wavelength range of 1500-1520 nm, then the responsivity should either increase with the decrease of wavelength (when the product of the modal

absorption coefficient and the length of the device $\alpha_{mod}L$ ~1 or <1), or decrease linearly with the wavelength (when $\alpha_{mod}L$ >>1). Yet Fig. 5.17 shows a steep decrease in responsivity at shorter wavelength. Therefore, this phenomenon is likely to be related to the wavelength dependence of the coupling efficiency. This explanation is supported by the transmission spectrum of the structure shown on the right hand axis of Fig. 5.17. Corresponding to the maximum responsivity at 1518 nm, the transmitted power shows a sharp valley; while for shorter wavelength the transmission is much higher. If the light has passed through the $Ge_{1-x}Si_x$ material as we designed in the butt-coupling scheme, then the transmitted power should actually decrease with the wavelength since the absorption coefficient is higher at shorter wavelength. The fact that we see an increase in transmission with the decrease of wavelength in 1480-1520 nm range indicates that the light can "by-pass" the $Ge_{1-x}Si_x$ material somehow and finds its way out. Theoretically there should not be such a "by pass" in the butt-coupling scheme when we consider the coupling between the fundamental modes of the Si waveguides and the $Ge_{1-x}Si_x$ modulator, because if light is not coupled into the $Ge_{1-x}Si_x$ material it should be scattered all over the places and cannot reach the output end of the device. Therefore, it must be due to some other factors.

One fabrication error that we have identified through cross-sectional SEM is that the thickness of the GeSi modulator was actually 480 nm instead of 600 nm due to the over-polishing of CMP process. The dimension of the Si waveguide, on the other hand, is 490×188 nm, and the center of the Si waveguide is higher than that of the GeSi modulator by 64 nm. Misalignment of the Si waveguide to the GeSi modulator/detector

surely decreases the coupling efficiency. However, in Fig. 4.22 we have already shown that such small misalignment would not affect the coupling significantly.

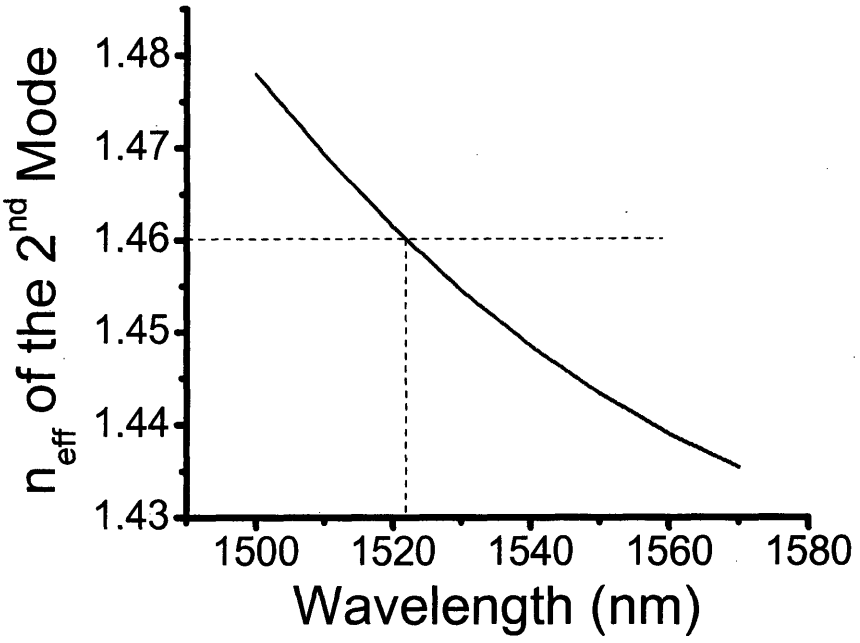

Fig. 5.18. Effective index (n_{eff}) of the second mode in a 490×188 nm Si waveguide as a function of wavelength.

Indeed, simulations by both the mode solving method and the BPM method show that even with the 64 nm vertical misalignment the coupling efficiency from the input Si waveguide to the GeSi detector/modulator should still be ~80% in the wavelength range of 1500-1550 nm if we only consider the coupling between the fundamental modes. The variation in coupling efficiency between the fundamental modes varies within 8% in the wavelength range of 1500-1550 nm, much smaller than the significant change in responsivity in Fig. 5.17. Therefore, to explain the spectral responsivity data we obtained in Fig. 5.17 we have to refer to higher order modes. Fig. 5.18 shows the simulation result of the effective index of the second mode vs. wavelength for a 490 × 188 nm Si

waveguide. When the calculated effective index is smaller than the index of the cladding (SiO_2, refractive index n=1.46), it is not a real guided mode and will dissipate away after some propagation. However, for wavelengths <1520 nm the effective index of the second mode becomes bigger than that of the SiO_2 cladding, indicating a real second mode supported by the waveguide. The shorter the wavelength, the higher the effective index of the second mode, and the more robust the mode. As a result, it is likely that the light could couple into the second order mode for wavelengths <1520 nm due to the perturbation of the sidewall roughness of the poly-Si waveguide or the slight fiber-to-waveguide misalignment in the measurement. As the wavelength decreases, a larger and larger proportion of the power could couple into the second order mode. Since the second order mode is mostly in oxide cladding, it has nearly no overlap with the mode in $Ge_{1-x}Si_x$ detector/modulator and can "by-pass" the device and propagate to the end of the output Si waveguide. Therefore, below 1520 nm the responsivity decreases sharply with the decrease of wavelength in Fig. 5.17.

To avoid measuring the effect of higher order modes, we can design a bend in the Si waveguide before the light reaches the GeSi photodetector. As shown earlier, the effective index of the second order mode is much lower than the first order mode, so the bending loss is much larger. For example, simulation results show that with a bending radius of 50 μm the second order mode is almost completely lost after a 90° bend while the fundamental mode remains intact. This way we can filter out the high order modes and eliminate its effect in the optical measurements.

Fig. 5.19 shows the responsivity at 1518 nm as a function of reverse bias. In contrast to the free space detectors in Chapter 3, the DC responsivity increases

significantly with the reverse bias, and from the trend of the curve it seems at 4 V reverse bias the DC responsivity just starts to reach saturation. We were unable to apply a bias great than 4 V since the leakage current at >4 V exceeds the range of our measurement system. The strong dependence of the DC responsivity on the reverse bias is also related to the problems we described in Section 5.4 on the I-V characteristics of the device. On one hand, the poor material quality and defects induced by CMP process greatly decrease the carrier lifetime in the material. On the other hand, the high leakage current at reverse bias due to the carrier generation in the depletion region induces an electric field (E_{gen}) counteracting the applied electric field E_{appl}. Therefore, the effective electric field in the depletion region is reduced to $E_{appl} - E_{gen}$ and the carrier transit time $\tau_{transit}$ is increased. As a result, the carriers cannot reach the electrodes before they recombine at the defects, and the collection efficiency is low. We can estimate E_{gen} by

$$E_{gen} \sim J_{gen}\tau_{transit} / \varepsilon, \tag{5.3}$$

where J_{gen} is the generation current density, and ε is the dielectric constant of the GeSi material. The transit time is given by

$$\tau_{transit} = H / v_{drift} = H /(\mu E_{eff} /(1 + \mu E_{eff} / v_{sat})), \tag{5.4}$$

where H is the thickness of the GeSi layer, v_{drift} is the carrier drift velocity, $E_{eff} = E_{appl} - E_{gen}$ is the effective electric in the GeSi layer, μ is the carrier mobility in GeSi, and v_{sat} is the saturation velocity in GeSi. Substituting (5.4) into (5.3) and using μ=1000 cm^2/V sec and v_{sat}=6×10^6 cm/sec, we estimate that the effective electric field in GeSi at 4V reverse bias is ~8.2 kV/cm. At this electric field the carriers can be

accelerated close to saturation velocity and nearly full DC responsivity can be achieved. This is consistent with our observation in Fig. 5.19, where the DC responsivity starts to saturate at 4V reverse bias.

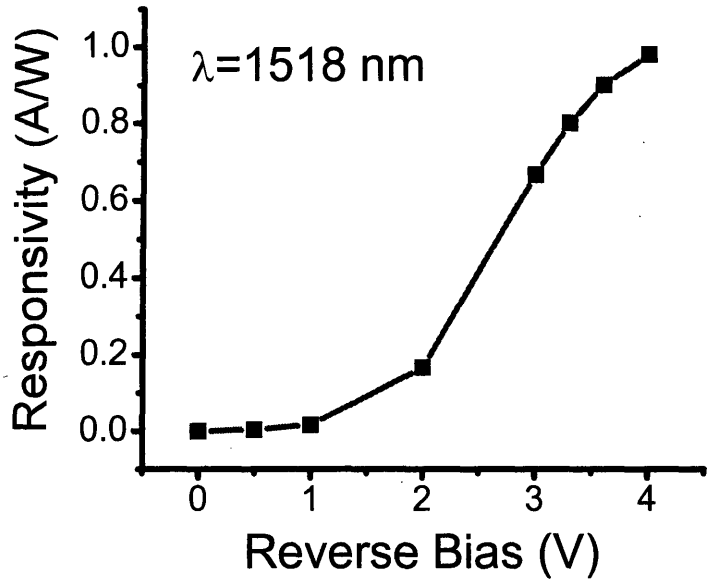

Fig. 5.19 DC responsivity vs. reverse bias of a waveguide coupled $Ge_{0.992}Si_{0.008}$ photodetector.

The experimental setup for the bandwidth measurement of the detector is shown in Fig 5.20. A 1550 nm laser was modulated by an external high speed optical modulator with a bandwidth of 10 GHz, and the modulated optical signal is sent to the $Ge_{1-x}Si_x$ photodetector through the optical fiber and the input Si waveguide.

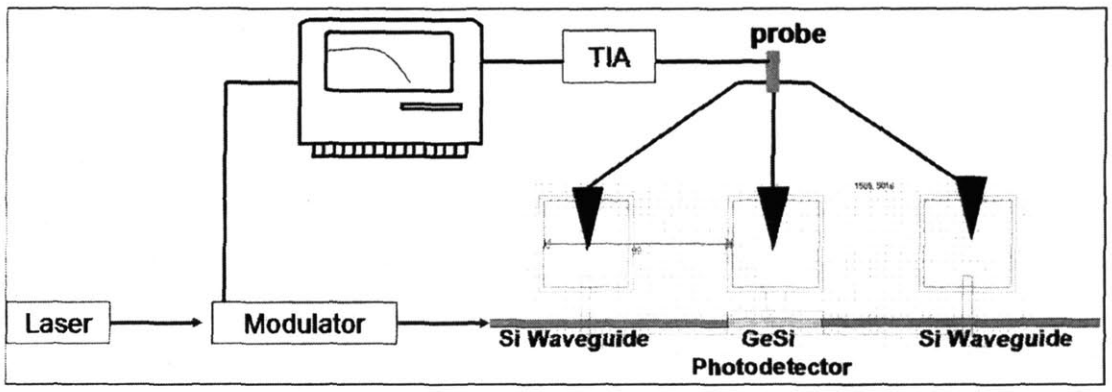

Fig. 5.20 The experimental set up for the bandwidth measurement of the waveguide integrated GeSi photodetector.

The photocurrent signal is amplified by a trans-impedance amplifier (TIA) for higher signal-to-noise ratio in the measurement. A network analyzer is used to scan the frequency of the modulation and read out the photocurrent as a function of modulation frequency via TIA. Fig 5.21 (a) and (b) show some typical results. The oscillation in the frequency scan is due to the RF impedance mismatch in the circuit. Our best device shows a bandwidth of >4.5 GHz (Fig. 5.21(a)). The roll off in this device is actually due to the bandwidth limitation of the TIA circuit instead of the detector itself. More commonly, a bandwidth of ~1.3 GHz was observed, as shown in Fig. 5.21 (b). These devices show a series resistance of <100 Ω and a capacitance of <0.1 pF. Therefore, the RC limited bandwidth should be in the range of ~20 GHz. The reason for the slower speed is most likely due to the slow carrier diffusion process in the defective $Ge_{1-x}Si_x$ material instead of the RC delay. Also, the fact that some devices show higher speed indicates the non-uniformity in the fabrication process, especially the defects formed during CMP, may also play a key role in the variation of the detector speed.

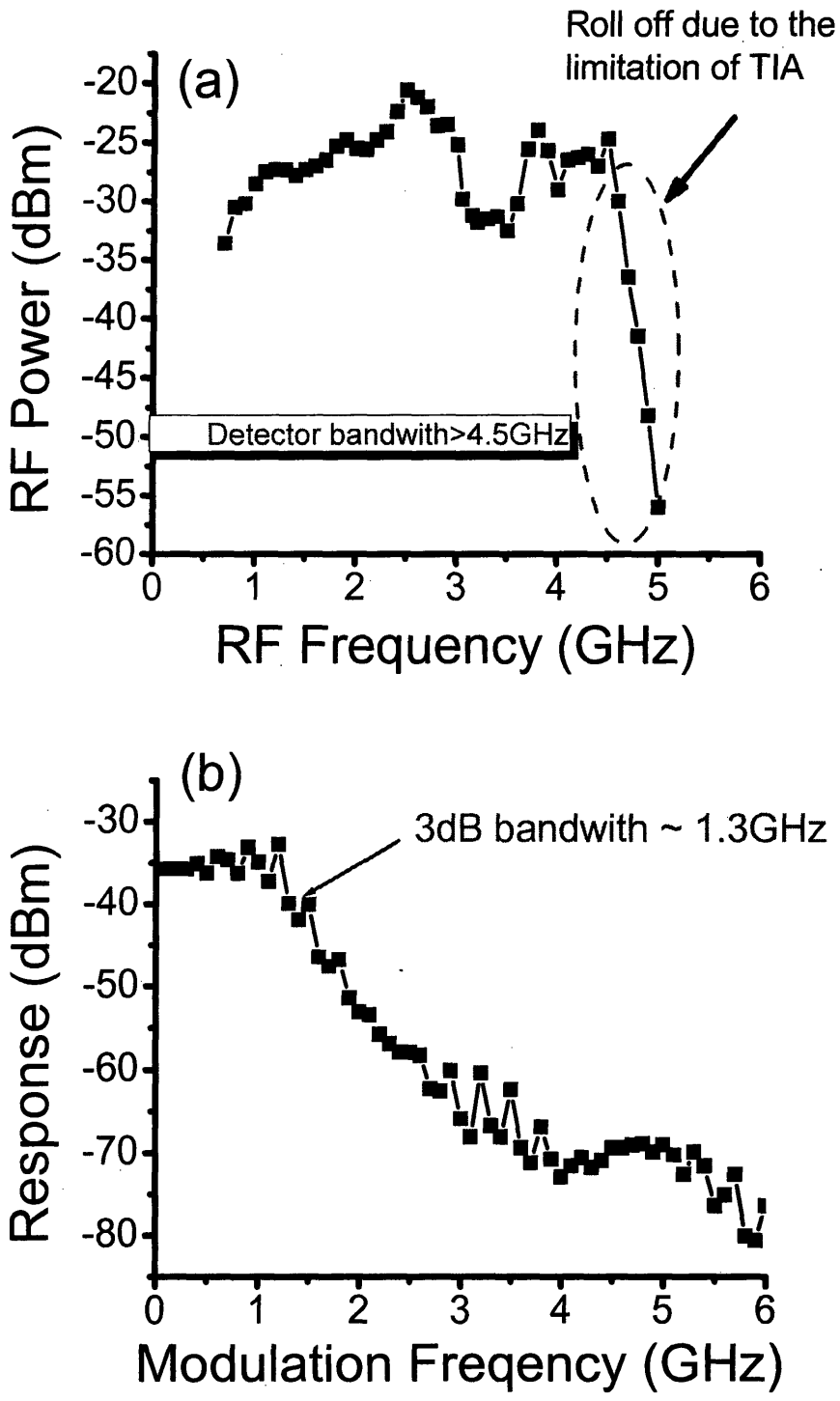

Fig. 5.21. Waveguide-integrated GeSi photodetector response vs. modulation frequency of (a) the best device in this fabrication run, and (b) an average device.

5.6 Preliminary Results on GeSi EA Modulators

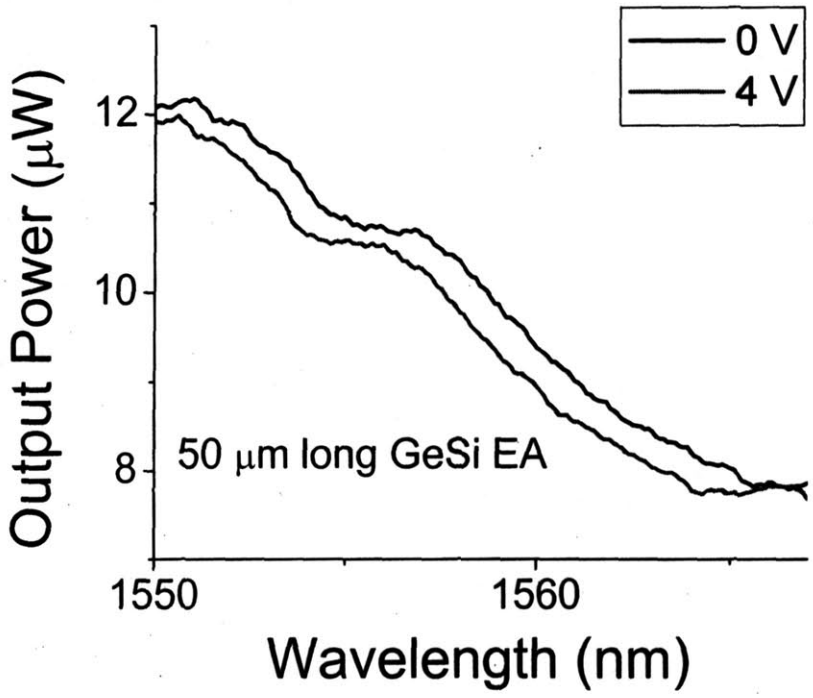

Fig. 5.22. Transmitted power vs. wavelength of the GeSi EA modulator at 0 and 4 V reverse bias.

The same experimental setup in waveguide-integrated detector measurement was also used to measure the performance of the GeSi electro-absorption modulator. In this case, we monitor the change in the output power at different wavelengths as we increase the reverse bias from 0 V to 4 V. Fig. 5.22 shows the experimental result. The maximum extinction ratio is only about 0.3 dB at around 1560 nm. This is because not enough electric field is built into the $Ge_{1-x}Si_x$ layer even though a significant reverse bias is applied due to the growth defects and sidewall defects in the $Ge_{1-x}Si_x$ material. As we mentioned earlier, the effective electric field in the GeSi layer is estimated to be ~8.2 kV/cm at 4V reverse bias. From Fig. 4. 8, we can find that the absorption coefficient of the $Ge_{1-x}Si_x$ material is 124/cm at 0 electric field, and no more than 150/cm at an electric

field <10 kV/cm. The corresponding modal absorption coefficients are 138/cm and 159/cm, respectively. Therefore, with Eqs. 4.23 and 4.25 we can calculate that the extinction ratio should be no more than 0.45 dB. This is consistent with our measurement result that the modulation depth is only ~0.3 dB. The performance should be greatly improved if we can obtain similar material quality as the free-space coupled photodiodes mentioned in Chapter 3, since strong FK effect was demonstrated in those devices and a significantly large electric field can be applied on the GeSi material.

In summary, we have demonstrated a preliminary waveguide-coupled GeSi photodetector with a responsivity of 1.0 A/W at 1518 nm and a bandwidth of >4.5 GHz, as well as a GeSi EA modulator with an extinction ratio of 0.3 dB. The devices suffer significantly from the dark current induced by the growth and fabrication defects in the first fabrication run. Solutions to the growth and fabrications issues are proposed and some of them are already tested. It is promising that we can achieve a device performance predicted in Chapter 4 in a future device fabrication.

Chapter 6. Summary and Future Work

This thesis focuses on the research of waveguide-integrated GeSi photodetectors and EA modulators on a Si platform for electronic-photonic integrated circuits (EPIC). We started with the growth and material characterization of tensile strained epitaxial Ge films on Si in Chapter 2. The direct band gap vs. tensile strain in Ge was measured for the first time, and deformation potential constants were obtained with relatively high accuracy. The tensile strain was engineered by backside silicidation and post-growth annealing. The direct band gap of Ge was decreased to 0.764 eV with 0.25% tensile strain, covering both the C and the L bands in telecommunications. We further investigated the tensile strain in selectively grown Ge mesas and stripes. The major strain relaxation mechanism was identified to be faceting-induced elastic relaxation. This knowledge is very helpful in our design of waveguide-coupled GeSi devices since they are achieved by selective growth in narrow trenches.

In Chapter 3 we demonstrate that the tensile strain in the Ge material transforms to a significant enhancement in the responsivity of the Ge photodetectors. Tensile strained Ge photodetectors were also achieved by selective growth. The broad detection spectrum, high bandwidth and low driving voltage makes it attractive for applications in Si-based EPIC.

Chapter 4 discusses the design of a waveguide-coupled GeSi EA modulator/photodetector. Enhanced Franz-Keldysh effect in tensile strained Ge was reported for the first time, and the experimental results agree with the theoretical model. We moved on to design the material composition and the device structure of GeSi EA modulators with optimal performance at 1550 nm. Our modeling and simulation results

show that an GeSi EA modulator with an extinction ratio of 10 dB and a bandwidth of >50 GHz can be achieved at the cost of ~4.8 dB insertion loss. Such performance is similar to the EA modulators based on III-V materials. The same material and device structure can be also used for waveguide-integrated photodetectors with a responsivity of 1.1 A/W at 1550 nm and a bandwidth >35 GHz. Therefore, an integration of GeSi modulator and photodetector can be achieved relatively easily.

Chapter 5 shows the preliminary results of our first attempt in fabricating waveguide-integrated GeSi photodetectors and EA modulators. A waveguide-integrated GeSi photodetector with a high responsivity of 1.0 A/W at 1518 nm and a bandwidth of >4.5 GHz was achieved. The first GeSi EA modulator we fabricated shows a modulation depth of ~0.3 dB at around 1560 nm. Both devices suffer from the defects related to the material growth and fabrications process, and the performance could be greatly improved with the eliminations of these defects. Solutions to the growth and fabrication issues are discussed and some of them were already tested.

There are several aspects that we should study in more detail in the future work. (1) We need to understand more about the GeSi selective growth in trenches. For example, the effect of trench direction on the growth rate and kinetics should be studied. It has been reported in the case of Si epitaxy that the growth in trenches along [100] direction is free of facets and defects at Si/SiO_2 sidewall interface is much less than the case of [110] trenches [129]. It would be interesting to our application if the same effect exists in the Ge epitaxy on Si, since by avoiding facet growth we could fill up the trench with a flat top and no CMP process is needed to remove the GeSi extruding out of the trench. (2) More analysis on our first lot of waveguide-integrated GeSi EA modulators

and detectors is needed. Although we proposed three possible reasons for the poor diode performance in this run, we are not able to tell which one of them has the most effect by now. Based on our proposed solutions in Chapter 5, we need another fabrication run to have a better understanding about the issues. Failure analysis with extensive TEM images are also needed, especially to see if the ends of the Si waveguides really reach the GeSi material in the butt-coupled structures. If there is an air gap or some other defect it could significantly affect the coupling efficiency. (3) More investigation is needed to evaluate the quality of SiO_2 passivation of GeSi sidewalls. The passivation of the sidewalls of the GeSi stripes is very important, since it may lead to significant peripheral leakage. Research should be done on other dielectric materials like SiON or GeON to compare with the SiO_2 passivation.

Although there are still many problems to solve before we can apply our waveguide-integrated GeSi modulators and detectors to real applications, the physics of these devices is sound and the fabrication problems should be resolved eventually. The GeSi devices have promising future for applications in both Si-based photonics and high speed electronic circuits.

References

[1] M. Paniccia, M. Morse, and M. Salib, Topics in Applied Physics **94**, 52, 2004. Also see http://www.raptureready.com/time/rap31d.html.
[2] Semiconductor Industry Association (SIA) Roadmap, 1997.
[3] International Technology Roadmap for Semiconductors, 2005 edition.
[4] http://news.com.com/Intel+kills+plans+for+4GHz+Pentium/2100-1006_3-5409816.html.
[5] S. V. Kartalopoulos, IEEE. Circuits. Device. **18** , 8 (2002)
[6] L. C. Kimerling, L. Dal. Negro, S. Saini, Y. Yi, D. Ahn, S. Akiyama, D. Cannon, J. Liu, J. G. Sandland, D. Sparacin, J. Michel, K. Wada and M. R. Watts, Topics in Applied Physics, **94**, 89 (2004)
[7] M. L. Lee, E. A. Fitzgerald, M. T. Bulsara, Matthew T. Currie, and Anthony Lochtefeld, J. Appl. Phys. **97**, 011101 (2005)
[8] C. O. Chui, S. Ramanathan, B. B. Triplett, P.C. McIntyre, and K. C. Sarawat, IEEE. Electron. Devic. Lett. **23**, 473 (2002)
[9] M. T. Currie, S. B. Samavedam, T. A. Langdo, C. W. Leitz, and E. A. Fitzgerald, Appl. Phys. Lett. **72**, 1718 (1998)
[10] H.-C. Luan, D. R. Lim, K. K. Lee, K. M. Chen, J. G. Sandland, K. Wada, and L. C. Kimerling, Appl. Phys. Lett. **75**, 2909 (1999).
[11] L. Colace , G. Masini, G. Assanto, H. C. Luan, K. Wada, L. C. Kimerling, Appl. Phys. Lett. **76**, 1231 (2000)
[12] S. Fama, L. Colace, G. Masini, G. Assanto, and H.-C. Luan, Appl. Phys. Lett. **81**, 586 (2002)
[13] S. J. Koester, J. D. Schuab, G. Dehlinger, J. O. Chu, Q. C. Ouyang, and A. Grill, Session V.A-4, 62nd Annual Device Research Conference, Notre Dame University, Notre Dame, Indiana, Jun 22, 2004.
[14] A. Irace, G. Breglio, M. Iodice and A. Cutolo, Topics in Applied Physics. **94**, 361 (2004)
[15] Vilson R. Almeida, Carlos A. Barrios, Roberto R. Panepucci and Michal Lipson, Nature. **431**, 1081 (2004)
[16] Qianfan Xu, Bradley Schmidt, Sameer Pradhan and Michal Lipson, Nature. **435**, 325 (2005)
[17] Ansheng Liu, Richard Jones, Ling Liao, Dean Samara-Rubio, Doron Rubin, Oded Cohen, Remus Nicolaescu and Mario Paniccia, Nature. **427**, 615 (2004)
[18] B. R. Bennett and R. A. Soref, IEEE. J. Quantum. Electron. **QE-23**, 2159 (1987)
[19] D. A. B. Miller, D.S. Chemla, T. C. Damen, A. C. Gossard, W. Wiegmann, T. H. Wood, and C. A. Burus, Phys. Rev. Lett. **53**, 2173 (1984)
[20] T. H. Wood, C. A. Burrus, D. A. B. Miller, D. S. Chemla, T. C. Damen, A. C. Gossard and W. Wiegmann, Appl. Phys. Lett. **44**, 16 (1984)
[21] J. F. Lampin, L. Desplanque, and F. Mollot, Appl. Phys. Lett. **78**, 4103 (2001)
[22] Tatemi Ido, Shigehisa Tanaka, Makoto Suzuki, Mari Koizumi, Hirohisa Sano, and Hiroaki Inoue. J. Lightwave. Technology. **14**, 2026 (1996)
[23] P. J. A. Thijs, L. F. Tiemeijer, P. I. Kuindersma, J. J. M. Binsma, T. Vandongen, IEEE. J. Quantum. Electron. **27**, 1426 (1991).
[24] D. K. Nayak, J. C. S. Woo, J. S. Park , K. L. Wang, K. P. MacWilliams, Appl. Phys. Lett. **62**, 2853 (1993).
[25] J. Welser, J. L. Hoyt, J. F. Gibbons, IEEE. Trans. Electron. Device. Lett. **15**, 100 (1994).
[26] K. K. Rim, J. L. Hoyt, J. F. Gibbons, IEEE. Trans. Electron. Device **47**, 1406 (2000).
[27] *Properties of Group IV Elements and III-V, II-V, and I-VII Compounds*, edited by O. Madelung, Landolt-Börnstein, Numerical Data and Functional Relationships in Science and Technology Vol. 17a, Chapter 1.3 (Springer, Berlin, 1982).
[28] S. L. Chuang, *Physics of Optoelectronic Devices,* Chapter 4, John Wiley & Sons, 1995
[29] C. G. Van de Walle, Phys. Rev. B **39**, 1871 (1989).
[30] I. Balslev, Solid. State. Commun **5**, 315 (1967).
[31] F. H. Pollak and M. Cardona, Phys. Rev. **172**, 816 (1968).
[32] A. R. Goñi, K. Syassen, M. Cardona, Phys. Rev. **B 39**, 12921 (1989).
[33] G. H. Li, A. R. Goñi, K. Syassen, M. Cardona, Phys. Rev. **B 49**, 8017 (1994).
[34] M. Chandrasekhar and F. H. Pollak, Phys. Rev. **B 15**, 2127 (1977).
[35] B. Welber, M. Cardona, Y. F. Tsay, B. Bendow, Phy. Rev. **B 15**, 875 (1977).

[36] I. Balslev, Phys. Rev. **143**, 636 (1966).
[37] J. J. Hall, Phys. Rev. **128**, 68 (1962).
[38] J. C. Hensel and K. Suzuki, Phys. Rev. **B 9**, 4219 (1974).
[39] A. P. Smith III, M. Cardona, F. H. Pollak, Am. Phys. Soc. **12**, 101 (1967).
[40] M. V. Fischetti and S. E. Laux, J. Appl. Phys. 80, 2234 (1996)
[41] J. F. Liu, D. D. Cannon, K. Wada, Y. Ishikawa, D. T. Danielson, S. Jongthammanurak, J. Michel, and L. C. Kimerling, Phys. Rev **B** 70, 155309 (2004)
[42] Y. Ishikawa, K. Wada, J.F. Liu, D. D. Cannon, H. C. Luan, J. Michel, and L. C. Kimerling, J. Appl. Phys 98, 013501 (2005)
[43] E. A. Fitzgerald, Mater. Sci. Rep. **7**, 91 (1991)
[44] H. P. Singh, Acta Crystallogr., Sect. **A**: Cryst. Phys., Diffr., Theor. Gen. Crystallogr. **24**, 469 (1968).
[45] Y. Okada and Y. Tokamaru, J. Appl. Phys. **56**, 314 (1984).
[46] D. D. Cannon, J. F. Liu, Y. Ishikawa, K. Wada, D. T. Danielson, S. Jongthammanurak, J. Michel, and L. C. Kimerling, Appl. Phys. Lett. **84**, 906 (2004).
[47] *Physics of Group IV Elements and III–V Compounds*, edited by O. Madelung, Landolt-Börnstein: Numerical Data and Functional Relationships in Science and Technology, Group III, Vol. 22a (Springer-Verlag, Berlin,1987) ; *Semiconductors. Intrinsic*
[48] Y. Ishikawa, K. Wada, D. D. Cannon, J. F. Liu, H.C. Luan, and L. C. Kimerling, Appl. Phys. Lett. **82**, 2044 (2003).
[49] D. E. Aspnes, Surf. Sci. **37**, 418 (1973).
[50] H. Shen, F. H. Pollak, Phys. Rev. B. **42**, 7097 (1990).
[51] H. Shen, M. Dutta, J. Appl. Phys. **78**, 2151 (1995).
[52] F. H. Pollak, Surf. Interface. Anal. **31**, 938 (2001).
[53] L. Colace , G. Masini, G. Assanto, H. C. Luan, K. Wada, L. C. Kimerling, Appl. Phys. Lett. **76**, 1231 (2000).
[54] G. K. Wertheim and G. L. Pearson, Phys. Rev. **107**, 694 (1957).
[55] H. F. Matare, *Defect Electronics in Semiconductors*, (John Wiley & Sons, New York, 1971)
[56] J. F. Liu, D. D. Cannon, K. Wada, Y. Ishikawa, S. Jongthammanurak, D. T. Danielson, J. Michel and L. C. Kimerling, Appl. Phys. Lett. **84**, 660 (2004).
[57] J. P. Gambino and E. G. Colgen, Mater. Chem. Phys. **52**, 99 (1998)
[58] L. Van den Hove, J. Vanhellemont, R. Wolters, W. Claassen, R. DeKeersmaecker and Declerck, in M. Scott, Y. Akasaka and R. Reif (eds.), *Advanced Materials for ULSI*, Vol 88-19, Electrochemical Soc. Inc., Pennington, NJ, 1988, p 165
[59] T. Ito, H. Azuma, S. Noda, Jpn. J. Appl. Phys. **33**, 5681 (1994)
[60] M. Ohring, *The Materials Science of Thin Films*, (Boston: Academic Press, 1992)
[61] L. Van den Hove, J. Vanhellemont, R. Wolters, W. Claassen, R. DeKeersmaecker and Declerck, in M. Scott, Y. Akasaka and R. Reif (eds.), *Advanced Materials for ULSI*, Vol 88-19, Electrochemical Soc. Inc., Pennington, NJ, 1988, p 165
[62] Properties of advanced semiconductor materials: GaN, AlN, InN, BN, SiC, SiGe , Chapter 6 (Wiley, New York, 2001).
[63] M. Nakamura, Metall. Mater. Trans. **A 25**, 331 (1993)
[64] K. Maex and M. Van Rossum, *Properties of Metal Silicides* 1st ed. (INSPEC, London, 1995)
[65] To take into account the relaxation of Ge film, we choose this $\Delta\alpha_2$ value such that the Ge films in Ge/Si(100)/Ge samples after 5 min RTA at 800°C have an in-plane strain of 0.204% at room temperature, as measured experimentally by XRD.
[66] Taeko Ando, Kazuo Sato, Mitsuhiro Shih&, Tetsuo Yoshioku, Yuji Yoshikuwa, and Tatsuo Kawabata, IEEE. International Symp. Micromechatronics. Human. Sci., p 55 (1997)
[67] T. A. Langdo, Ph.D. thesis, Massachusetts Institute of Technology (2001)
[68] H. C. Luan, Ph.D. thesis, Massachusetts Institute of Technology (2002)
[69] K. Brunner, Rep. Prog. Phys. **65**, 27 (2002)
[70] J. Tersoff and R. M. Tromp, Phys. Rev. Lett. **70**, 2782 (1993)
[71] J. Tersoff and F. K. LeGoues, Phys. Rev. Lett. **72**, 3570 (1994)
[72] J. F. Liu, D. D. Cannon, K. Wada, Y. Ishikawa, S. Jongthammanurak, D. T. Danielson, J. Michel, and L. C. Kimerling, Applied Physics Letters **87**, 011110 (2005)

[73] R. Labusch, J. De. Physique. **III 7**, 1411 (1997)
[74] S. A. Shevchenko, Semiconductors. **34**, 527 (2000)
[75] V. A. Goncharov, Yu. A. Osip'yan, and S. A. Shevchenko, Fiz. Tverd. Tela (Leningrad) **29**, 1928 (1987) [Sov. Phys. Solid State **29**, 1110 (1987)].
[76] Yu. A. Osip'yan and S. A. Shevchenko, Pis'ma Zh. Éksp.Teor. Fiz. **20**, 709 (1974) [JETP Lett. **20**, 328 (1974)].
[77] J. Hess and R. Labusch, Phys. Stat. Sol. **A 138**, 617 (1993).
[78] http://usa.hamamatsu.com/assets/pdf/parts_G/G8198_series.pdf
[79] C. Jacoboni, F. Nava, C. Canali and G. Ottaviani, Phys. Rev. **B 24,** 1014 (1981).
[80] E. J. Ryder, Phys. Rev. **B 90,** 766 (1953).
[81] A. Frova and P. Handler, Phys. Rev. **137**, A 1857 (1965).
[82] J. F. Liu, J. Michel, W. Giziewicz, D. Pan, D. D. Cannon, D. T. Danielson, S. Jongthammanurak, K. Wada, and Lionel C. Kimerling, Appl. Phys. Lett. 87, 103501 (2005)
[83] F. O. Ilday, J. R. Buckley, H. Lim, F. W. Wise, and W. G. Clark, Opt. Lett. **28**, 1365 (2003).
[84] W. Giziewicz, Ph. D. thesis, Massachusetts Institute of Technology. (2006)
[85] S. M. Sze, *Physics of Semiconductor Devices*, 2nd ed. (Wiley, New York, 1981).
[86] M. V. Hobden, J. Chem. Phys. Solid. **23**, 821 (1962)
[87] W. Meer, D. Pommerrenig, Z. Angew. Phys. **23**, 369 (1967)
[88] C. J. Sher DeCusatis and C.-L. J. Jiang, "Chapter 3, Detectors for Fiber Optics," in *Handbook of Fiber Optic Data Communication*, C. DeCusatis, E. Maass, D. P. PClement, and R. C. Lasky, Eds. London: Academic Press, 1998, pp. 87-114.
[89] B. E. A. Saleh and M. C. Teich, *Fundamentals of Photonics*, Chapter 17, pp 673-690, John Wiley & Sons (1990)
[90] A. Yariv, *Optical Electronics in Modern Communications*, Fifth ed. New York: Oxford University Press, 1997.
[91] S. L. Chuang, *Physics of Optoelectronic Devices*, Chapter 13, pp 546-548
[92] A. Frova and P. Handler, Phys. Rev. **137**, A1857 (1965)
[93] A. Frova, P. Handler, F. A. Germano and D. E. Aspnes, Phys. Rev. **145**, 575, (1966)
[94] B. O. Seraphin and R. B. Hess, Phys. Rev. Lett. **14**, 138 (1965)
[95] K. G. Asha and R. L. Anderson, Phys. Rev. **154**, 721 (1967)
[96] T, Hamakawa., F. Germano, and P. Handler, J. Phys. Soc. Japan. **21**, 111 (1966)
[97] C. Pickering, R. T. Carline, D. J. Robbins, W.Y. Leong, S. J. Barnett, A. D. Pitt, and A. G. Cullis, J. Appl. Phys. **73** , 239 (1993)
[98] J. Humlicek, M. Garriga, M. I. Alonso, and M. Cardona, J. Appl. Phys. **65**, 2827 (1989).
[99] J. S. Kline, F. H. Pollak, and M. Cardona, Helv. Phys. Acta **41**, 968 (1968).
[100] R. Braunstein., A. R. Moore, and F. Herman, Phys. Rev. **109,** 695 (1958)
[101] J. Weber and M.I. Alonso, *Phys. Rev. B* **40** , 5683 (1989)
[102] Properties of Advanced Semiconductor Materials: GaN, AlN, InN, BN,SiC, SiGe, Chapter 6, pp 177-178 (Wiley, New York, 2001).
[103] J. M. Hartmann, A. Abbadie, A. M. Papon, P. Holliger, G. Rolland, T. Billon, J. M. Fédéli, M. Rouvière, L. Vivien, and S. Laval, J. Appl. Phys. **95**, 5905 (2004)
[104] J. Humlicek, in *Properties of Strained And Relaxed Silicon Germanium* (edited by K. Kasper), EMIS Datarevews Series. No. 12, INSPEC, London, 1995; Chapters 4.6 and 4.7, pp. 116-131.
[105] *Properties of Group IV Elements and III-V, II-V, and I-VII Compounds*, edited by O. Madelung, Landolt-Börnstein, Numerical Data and Functional Relationships in Science and Technology Vol. 17a, Chapter 1.6, pp 450-451 (Springer, Berlin, 1982).
[106] P. Lawaetz, Phy. Rev. **B** 4, 3460 (1971)
[107] Kevin K. Lee, Desmond R. Lim, Hsin-Chiao Luan, Anuradha Agarwal, James Foresi, and Lionel C. Kimerling, Appl. Phys. Lett. 77, 1617 (2000)
[108] Kevin K. Lee, Desmond R. Lim, Lionel C. Kimerling, Jangho Shin and Franco Cerrina, Optics. Lett. **26**, 1888 (2001)
[109] http://www.apollophoton.com/apollo/page.php?id=10
[110] P. E. Schmidt, Phys. Rev. B. **23**, 5531 (1981)
[111] S. L. Chuang, *Physics of Optoelectronic Devices*, Chapter 5, pp 209-214
[112] R. Zengerle, H. Briickner, H. Olzhausen and A. Kohl, Electron. Lett. **28**, 631 (1992)

[113] Osamu Mitomi, Kazuo Kasaya, and Hiroshi Miyazawa, IEEE. J. Quantum. Electron. **30**, 1787 (1994)
[114] J. Vanroey, J. Vanderdonk, and P. E. Lagasse, J. Optic. Soc. Am. **71**, 803 (1981)
[115] http://web1.rsoftdesign.com/products/component_design/BeamPROP/
[116] W. J. Choi, A. E. Bond, J.W. Kim, J.M. Zhang, R. Jambunathan, H. Foulk, S. O'Brien, J. Van Norman, D. Vandegrift, C. Wanamaker, J. Shakespeare, and H. Cao, J. Lightwave. Technol. **20**, 2052 (2002)
[117] P C Andricacos, C Uzoh, J O Dukovic, J Horkans, and H Deligianni, IBM. J. R&D. **42**, 567 (1998)
[118] S. H. Jones, L. K. Seidel K. M. Lau and M. Harold, J. Cryst. Growth. **108** 73, (1991)
[119] C. I. Drowley, G. A. Reid, and R. Hull, Appl. Phys. Lett. **52**, 546 (1988)
[120] W. K. Burton, N. Cabrera, and C. Frank, Philosophical Transactions of the Royal Society of London. Series A, vol 243, pp 299-358 (1951)
[121] Y. Wakayama, T. Tagami1, S-I. Tanaka, Thin. Solid. Films. **350**, 300, (1999)
[122] http://www.ioffe.ru/SVA/NSM/nk/AluminumCompounds/Gif/al.gif
[123] M. Y. Ghannam, and R. P. Mertens. IEEE. Electron. Device. Lett. **10**, 242 (1989)
[124] S. Y. Han, H. S. Yang, K. H. Baik, S. J. Pearton and F. Rend, Jpn. J. Appl. Phys. **44**, 7234 (2005)
[125] G. S. Oehrlein, Mater. Sci. Engn. **B** 4, 441 (1989)
[126] G. S. Oehrlein and R. Kalish, Appl. Phys. Lett. **54**, 2698 (1989)
[127] T. A. Lango, Ph.D. Thesis, Chapter 4, Massachusetts Inst. Technology, (2001)
[128] *Properties of Group IV Elements and III-V, II-V, and I-VII Compounds*, edited by O. Madelung, Landolt-Börnstein, Numerical Data and Functional Relationships in Science and Technology Vol. 17a, Chapter 1.6, pp 457 (Springer, Berlin, 1982)
[129] A. Ishitani, H. Kitajima, N. Endo, and N. Kasai, Jpn. J. Appl. Phys. **24**, 1267 (1985)

Glossary

AFM: Atomic force microscopy.

BER: bit error rate. The ratio of the number of error bits to the total number of bits.

dB is an abbreviation for decibel. $dB=10\log_{10}(P_2/P_1)$, where P_2 is a quantity compared to P_1.

dBm is an optical power unit used in telecommunications. Let P be the optical power in terms of mW, then in terms of dBm it equals to $10\log_{10}(P)$. Therefore, 0 dBm= 1mW, and 10 dBm=10 mW.

3dB bandwidth (frequency) is the frequency at which the power output of a divice drops to half of the DC case. For photodetectors, it means that the responsivity of the device at this frequency is equal to the DC responsivity divided by $\sqrt{2}$.

Deformation potential constants describe the amount of band gap change under a certain amount of strain in the semiconductor material. The dilational deformation potential, *a*, describes the effect of hydrostatic strain on the band gap of the material, while the devitorial deformation potential, *b*, describes the effect of the devitorial part of the strain tensor on the band gap of the material.

DWDM: Dense wavelength division multiplexing.

EA: Electro-absorption.

Electro-absorption effect refers to the phenomenon that an applied electric field can change the absorption of a material in a range of wavelength.

EPIC: Electronic-photonic integrated circuits.

External quantum efficiency (for detectors): The number of photogenerated electron-hole pairs that are collected by the electrodes divided by the *raw* number of incident photons. It takes into account the propagation and coupling losses of photons as well as the carrier collection efficiency.

Extinction Ratio refers to the contrast in the output optical power between the optical off-state and on-state of a modulator in unit of dB.

FOM: Figure of merit.

FTTX: Fiber to the X

HRTEM: high resolution transmission electron microscopy.

Internal quantum efficiency (for detectors): The number of photogenerated electron-hole pairs that are collected by the electrodes divided by the number of photons that reach the active region of the detector. It does not take into account the propagation and coupling losses of photons.

Insertion loss refers to the loss of optical power at the optical "on" state (transparent state) of a modulator in unit of dB.

PR: Photoreflectance

Responsivity equals to the photocurrent divided by the incident optical power. The unit is usually A/W or mA/W.

RIE: reactive ion etching

SEM: scanning electron microscopy

SIMS: Secondary ion mass spectrometry

SNR: signal-to-noise ratio

TEM: transmission electron microscopy

ULSI: ultra-large scale integrated circuits.

XRD: X-ray diffraction